The squeeze laser and its applications in quantum sensing

Dissertation

zur Erlangung des Doktorgrades

an der Fakultät für Mathematik, Informatik und Naturwissenschaften

Fachbereich Physik

der Universität Hamburg

Doktorarbeit

vorgelegt von

Pascal Gewecke

Hamburg

2024

Abstract

Laser interferometers are able to measure relative optical length changes and to analyze material properties, surface structures, and density fluctuations of fluids and gases. As these setups approach the quantum limit in sensitivity, employing quantum squeezed light becomes a crucial method to enhance the signal-to-noise ratio without increasing the optical power. Squeeze lasers, which produce these squeezed states, have been successfully improved for almost three decades and were implemented in gravitational wave detectors as a first user application. As quantum squeezing finds more practical applications, conventional squeeze lasers, which take up a full optical table, become impractical. The need for compact, robust, and versatile devices rises.

Here, I designed, built, and set up two squeeze lasers on breadboards with footprints of $80\,\text{cm} \times 80\,\text{cm}$ and $60\,\text{cm} \times 40\,\text{cm}$ and with squeezing values at a Fourier-frequency of $5\,\text{MHz}$ of $(10.70 \pm 0.18)\,\text{dB}$ and $(10.06 \pm 0.14)\,\text{dB}$ respectively. One of this setups was used for a laser Doppler vibrometer experiment at the Clausthal University of Technology. My squeeze laser increased the sensitivity of the heterodyne readout of the motion of a oscillating mirror at $1\,\text{MHz}$ by $(2.77 \pm 0.61)\,\text{dB}$. As another practical application of squeeze lasers, I report on the squeezed-light enhanced detection and characterization of ultrasonic sound waves in air between $4.2\,\text{MHz}$–$7.2\,\text{MHz}$ via a Mach-Zehnder interferometer at $1550\,\text{nm}$. Squeezed light allowed to enhance the sensitivity of the setup by more than $10\,\text{dB}$, enabling the detection of sound waves up to $(0.12 \pm 0.02)\,\frac{\text{mPa}}{\sqrt{\text{Hz}}}$.

The work in this thesis demonstrates practical uses of the squeeze laser and opens the path for a new generation of applications for squeezed light.

Kurzfassung

Laser interferometer sind in der Lage, relative, optische Längenänderungen zu messen sowie Materialeigenschaften, Oberflächenstrukturen und Dichtefluktuationen von Flüssigkeiten und Gasen zu analysieren. Wenn diese Geräte das Quantenlimit in ihrer Sensitivität erreichen, kann die Implementierung von gequetschtem Licht eine entscheidende Methode zur Erhöhung des Signal-Rausch-Verhältnisses darstellen, ohne dabei die optische Lichtleistung zu erhöhen. Quetschlaser, die solche gequetschten Zustände erzeugen, wurden in nahezu drei Dekaden erfolgreich verbessert und in Gravitationswellendetektoren als erste Nutzeranwendung implementiert. Während das Quanten-Quetschen mehr praktikable Verwendungen finden, werden konventionelle Quetschlaser, die einen kompletten optischen Tisch einnehmen, impraktikabel. Der Bedarf nach einem kompakten, robusten und vielseitigen Gerät wächst.

In dieser Arbeit habe ich zwei Quetschlaser entworfen und auf zwei Lochrasterplatten mit einer Größe von $80\,\mathrm{cm}\times80\,\mathrm{cm}$ and $60\,\mathrm{cm}\times40\,\mathrm{cm}$ und mit Quetschwerten bei einer Fourierfrequenz von $5\,\mathrm{MHz}$ mit jeweils $(10.70\pm0.18)\,\mathrm{dB}$ und $(10.06\pm0.14)\,\mathrm{dB}$ aufgebaut. Einer dieser Aufbauten wurde für ein Laser Doppler Vibrometer Experiment in der Technische Universität Clausthal genutzt. Mein Quetschlaser erhöhte die Sensitivität der heterodynen Auslesung von der Bewegung eines oszillierenden Spiegels bei $1\,\mathrm{MHz}$ um $(2.77\pm0.61)\,\mathrm{dB}$. In einer anderen praktikablen Anwendung für Quetschlaser berichte ich von der durch Quetschlicht verbesserten Detektion und Charakterisierung von Ultraschallwellen in Luft zwischen $4.2\,\mathrm{MHz}$–$7.2\,\mathrm{MHz}$ in einem Mach-Zehnder Interferometer bei $1550\,\mathrm{nm}$. Gequetschtes Licht ermöglichte die Verbesserung der Sensitivität des Systems um mehr als $10\,\mathrm{dB}$, was die Detektion von Schallwellen bis zu $(0.12\pm0.02)\,\frac{\mathrm{mPa}}{\sqrt{\mathrm{Hz}}}$ erlaubt.

Die Arbeit in dieser Dissertation demonstriert praktische Verwendungen von Quetschlichtlaser und öffnet den Weg für eine neue Generation von Anwendungen für Quetschlicht.

Contents

1 Introduction

Quantum noise is a fundamental principle in quantum mechanics, stemming from the Heisenberg uncertainty relation introduced by Werner Heisenberg in 1925 [1, 2, 3]. The primary assertion of this principle depicts an inherent limit to the precision with which certain pairs of observables can be simultaneously detected. If one considers monochromatic, coherent light, such a pair of observables is given in the form of energy $E = \hbar\omega$ and time t, where $\hbar$ denotes the reduced Planck constant and ω the frequency of the light. This limit in precision is called the uncertainty of the quadrature and results in the quantum photon shot noise, or simply shot noise, which is the dominating contribution of the quantum noise for interferometric measurements with low optical power.

There are two possibilities to enhance the sensitivity of a quantum noise limited measurement: Firstly, by increasing the laser power in the system, and secondly, by injecting squeezed light.

Squeezed states of light describe a unique quantum state where the uncertainty in a certain quadrature, phase or amplitude, is reduced below the vacuum uncertainty at the expense of enhancing the orthogonal quadrature. By exploiting the quantum correlations embedded in squeezed states, otherwise impossible enhancements in the signal-to-noise ratio can be achieved. The first experimental realization of squeezed states were reported in 1986 in [4] and a year later in [5], where both experiments utilized four-wave-mixing. In [6], squeezed light was produced by parametric down-conversion, a process, which is nowadays the state-of-the-art technique. Ever since, the production of high squeezing values for conventionally used wavelengths has been pursued: First, at the wavelength of 1064 nm, 10 dB of squeezing in 2008 [7] and

15.3 dB in 2016 [8] were achieved. Simultaneously, studies at the telecommunication wavelength of 1550 nm were conducted: 12.3 dB in 2011 [9], 13.1 dB in 2018 [10], and more recently 13.5 dB in 2022 [11] were generated. Enhancing the squeezing values even further becomes increasingly more difficult as the acceptable optical loss in the system limits the purity of the squeezed states. For the detection of 16 dB strong squeezed states, for example, only 2.5 % of optical loss in the system is allowed. Although still desired, the focus of research shifts from generating even higher squeezing values to enabling high squeezing values below acoustic frequencies [11] and for a broader range of laser wavelength, such as 2128 nm [12].

The most prominent application of squeezed light occurs in gravitational wave detectors. These Michelson interferometers with kilometer long arm lengths combine the work of hundreds of researchers worldwide. As the circulating light power in gravitational wave detectors already approaches the limits of the coatings and causes thermal deformations of the optical components and instabilities, squeezed light remains an important technique to mitigate quantum noise. The first squeezed light enhanced search for gravitational waves was performed in the gravitational wave detector GEO600, south of Hannover, between 2011 and 2012 [13]. Since 2019, squeezed light is used in both AdvancedLIGO [14] and AdvancedVIRGO [15], representing the most sensitive detectors on the planet for detecting relative length changes. More recently, frequency-dependent squeezed light was introduced and is applied in the current observation run of the AdvancedLIGO detector to reduce both the quantum radiation pressure noise as well as the quantum shot noise simultaneously [16].

Besides gravitational wave detection, other applications for squeezed light are starting to gain interest, especially in quantum communication and quantum sensing. In the former, the entanglement of squeezed states is used to provide a secure communication channel through quantum key distribution (QKD) [17, 18]. In quantum photometry, the influence of optical loss on the purity of squeezed states is utilized and the absorption of samples can be characterized. Additionally, the absolute calibration of photodiodes was shown in [8]. In quantum sensing, the detection of biomedical probes, presented in [19] for yeast cells, shows another application for

squeezed light. Here, the utilization of squeezed light is especially lucrative, as high laser power can damage or destroy the sample. On the other hand, for industrial purposes, squeeze lasers can provide eye-safe measurements and reduce the cost of laser safety regulations. These applications, however, require the squeeze laser to be easily portable, while still allowing a fast implementation in the experiment and without compromising in the generated squeezing value.

As the demand for squeezed light in different fields diversifies, vast improvements of the setups of the squeeze laser in the last decade were developed. Initially covering large optical tables, the size of the squeeze laser in GEO600 was set up on a portable breadboard with a $1.35\,\mathrm{m}\times1.15\,\mathrm{m}$ footprint [20]. In the following years, the size was decreased to $80\,\mathrm{cm}\times80\,\mathrm{cm}$ in [21]. In the first part of my theses, I demonstrate the realization of a squeeze laser on a portable breadboard with a footprint of merely $60\,\mathrm{cm}\times40\,\mathrm{cm}$.

As squeeze lasers become smaller and easier to set up, the implementation in industrial laser-based sensors and detectors is a future aspect of interest. Here, laser Doppler vibrometers (LDVs) provide the ability to characterize surface structures, vibrational motion of samples and density fluctuations of fluids or gases. In the LDV, light is typically back-reflected of a vibrating surface and exhibits information due to the imposed Doppler shift. In the second part of my thesis, I show the transportation of a squeeze laser from the University of Hamburg to the Clausthal University of Technology. There, the system was utilized to enhance sensitivity in a laser Doppler vibrometer, which was set up by Mengwei Yu, with heterodyne readout.

The topology of laser Doppler vibrometers occurs challenges, when the surface of the sample is uneven or when the absorption of the sample is high. Conventional approaches to enhance the signal-to-noise ratio include increasing the optical power or, to enhance the reflectivity of the surface, attaching a highly reflective mirror to the sample. Both of these measures are suboptimal: High laser powers can lead to damage on the sample if the absorption is high, while attaching a mirror to the sample negates the non-contact properties of laser-based detection.

To circumvent the problem of rough and absorbing surfaces, we conducted an experiment in the third part of this thesis for the detection of sound waves emitted by a transducer in a homodyne Mach-Zehnder interferometer. In this topology, only the sound waves of the vibrating sample are detected, which makes the measurement independent from the surface structure. As the sound waves interact with the laser light by changing the refractive index, no additional optical loss is introduced, which allows the usage of high squeezing values.

The thesis is structured as follows:

- Chapter 2 provides a short, fundamental background about quantum optics and, in detail, about squeezed states.

- In Chapter 3, the generation, the detection and the experimental limitations of squeezed states will be discussed. Furthermore, the differences between homodyne and heterodyne readout schemes will be highlighted.

- Chapter 4 shows the experimental setup of the squeeze lasers used in this thesis. Here, I compare different types of designs in terms of performance, size, and usability.

- The transportation and the implementation of a squeeze laser in a heterodyne laser Doppler vibrometer is presented in Chapter 5.

- In Chapter 6, the detection of ultrasonic sound waves in a homodyne Mach-Zehnder interferometer will be enhanced by a squeeze laser.

- Lastly, Chapter 7 summarizes the results of the thesis and gives an outlook for future development of the squeeze laser.

2 Quantum states of light

This chapter provides a simplified overview of the theoretical background concerning the description of the light field in quantum mechanics and the different classical and non-classical states used in this thesis. The important $\hat{X}$ and $\hat{Y}$ operators, known as amplitude and phase quadratures, are introduced and the sideband picture in the "two-photon formalism" is presented. The main references for this chapter are [22, 23, 24, 25].

2.1 Quantization of the electromagnetic field

In this section, I focus on the quantization of light and its description in the "two-photon formalism", which describes the quantized formalism of amplitude and phase modulations. The following calculations are introduced in [23] and [24]:

For a single-mode plane wave field, the electric field can be described as:

$$E(x,t) \equiv E^+(x,t) + E^-(x,t)\,, \tag{2.1}$$

where

$$E^+(x,t) = \int E(\omega)e^{-\mathrm{i}\omega(t-x/c)}\frac{\mathrm{d}\omega}{2\pi}\,, \tag{2.2}$$

$$E^-(x,t) = (E^+(x,t))^*\,. \tag{2.3}$$

$E^+(x,t)$ and $E^-(x,t)$ describe the positive ($\omega > 1$) and negative ($\omega < 1$) frequency parts, respectively, and $E(\omega)$ is the complex amplitude of the plane-wave mode. We further simplify $E(x - ct) = E(t)$. For a better description, the annihilation operator is introduced as

$$\hat{a}_\omega = \sqrt{\frac{c\mathcal{A}}{4\pi\hbar\omega}}E(\omega)\,, \tag{2.4}$$

where $\hbar$ is the reduced Planck constant, $\mathcal{A}$ is the effective cross-sectional area of the laser beam, and c is the speed of light. The operator obeys the commutation relation

$$[\hat{a}_\omega, \hat{a}_{\omega'}] = 0 \tag{2.5}$$

and its eigenstates are the coherent states. The electric field can be rewritten as

$$\hat{E}(t) = \sqrt{\frac{2\pi\hbar}{\mathcal{A}c}}\int_0^\infty \sqrt{\omega}(\hat{a}_\omega e^{-\mathrm{i}\omega t} + \hat{a}_\omega^\dagger e^{\mathrm{i}\omega t})\frac{\mathrm{d}\omega}{2\pi}\,, \tag{2.6}$$

where $\hat{a}_\omega^\dagger$ is the creation operators. $\hat{a}_\omega$ and $\hat{a}_\omega^\dagger$ describe the creation or annihilation of a photon at frequency ω. They are non-Hermitian and therefore non-observable. These operators obey the commutation relation:

$$[\hat{a}_\omega, \hat{a}^\dagger_{\omega'}] = 2\pi\delta(\omega - \omega') \tag{2.7}$$

and their product is the number operator $\hat{n} \equiv \hat{a}^\dagger\hat{a}$. Applying the creation or annihilation operator on the energy eigenstate $\hat{n}_\omega$ results in

$$\hat{a}_\omega |n_\omega\rangle = \sqrt{n_\omega} |n_\omega - 1\rangle \,, \tag{2.8}$$

$$\hat{a}^\dagger_\omega |n_\omega\rangle = \sqrt{n_\omega + 1} |n_\omega + 1\rangle \,. \tag{2.9}$$

2.2 Two-photon formalism

The "two-photon formalism", introduced by Caves and Schumaker in [22], describes processes, in which an upper and a lower sideband field are created or annihilated simultaneously. This sideband picture can describe the phase and amplitude modulations in the following way: A signal at the frequency Ω creates symmetric modulation sidebands at $\omega_0 \pm \Omega$ around the carrier frequency at ω_0. In this notation, the creation and annihilation operators, which now describe the creation or annihilation of a photon at the sideband frequency $\pm\Omega$, change to

$$\hat{a}_\pm = \lambda_\pm \hat{a}_{\omega_0 \pm \Omega}, \; \hat{a}^\dagger_\pm = \lambda_\pm \hat{a}^\dagger_{\omega_0 \pm \Omega} \,, \tag{2.10}$$

where $\lambda_\pm \equiv \sqrt{(\omega_0 \pm \Omega)/\omega_0}$ is used as a scaling of the energies of the photons at different frequencies. The carrier frequency is usually of the order of several THz, whereas Ω, as the measurement frequency, is in this thesis limited to tens of MHz. With this approximation, we can estimate $\omega_0 \gg \Omega$, so that $\lambda \approx 1$.

The two-photon operators are defined as [22]

$$\hat{X}_\Omega = \hat{a}_+ + \hat{a}_-^\dagger \,, \tag{2.11}$$

$$\hat{Y}_\Omega = -\mathrm{i}(\hat{a}_+ + \hat{a}_-^\dagger) \,, \tag{2.12}$$

and they obey the commutation relations

$$[\hat{X}_\Omega, \hat{X}_{\Omega'}] = [\hat{X}_\Omega, \hat{Y}_{\Omega'}] = [\hat{Y}_\Omega, \hat{Y}_{\Omega'}] = 0 \,, \tag{2.13}$$

$$[\hat{X}_\Omega, \hat{X}_{\Omega'}^\dagger] = [\hat{Y}_\Omega, \hat{Y}_{\Omega'}^\dagger] = 2\pi\delta(\Omega - \Omega') \,, \tag{2.14}$$

$$[\hat{X}_\Omega, \hat{Y}_{\Omega'}^\dagger] = [\hat{X}_\Omega^\dagger, \hat{Y}_{\Omega'}] = 2\pi\mathrm{i}\delta(\Omega - \Omega') \,. \tag{2.15}$$

Physically speaking, they create one photon with the frequency Ω while simultaneously annihilating one at $-\Omega$, which becomes evident, when they are applied to the number operator:

$$\hat{X}_\Omega \ket{n_\omega} = \sqrt{n_{\omega_0+\Omega}} \ket{n_{\omega_0+\Omega} - 1} + \sqrt{n_{\omega_0-\Omega} + 1} \ket{n_{\omega_0-\Omega} + 1} \tag{2.16}$$

The electric field from equation 2.6 can be rewritten to

$$\hat{E}^\pm(t) = \frac{1}{2}(\hat{X}_\Omega \pm \mathrm{i}\hat{Y}_\Omega)e^{\mp\mathrm{i}\omega_0 t} \,, \tag{2.17}$$

which leads to the more convenient form

$$\hat{E}(t) = \hat{X}_\Omega \cos(\omega_0 t) + \hat{Y}_\Omega \sin(\omega_0 t) \,, \tag{2.18}$$

with

$$\hat{X}_\Omega(t) = \sqrt{\frac{2\pi\hbar\omega_0}{\mathcal{A}c}} \int_0^\infty (\hat{X}_\Omega e^{-\mathrm{i}\Omega t} + \hat{X}_\Omega^\dagger e^{\mathrm{i}\Omega t}) \frac{\mathrm{d}\Omega}{2\pi}\,, \tag{2.19}$$

$$\hat{Y}_\Omega(t) = \sqrt{\frac{2\pi\hbar\omega_0}{\mathcal{A}c}} \int_0^\infty (\hat{Y}_\Omega e^{-\mathrm{i}\Omega t} + \hat{Y}_\Omega^\dagger e^{\mathrm{i}\Omega t}) \frac{\mathrm{d}\Omega}{2\pi}\,. \tag{2.20}$$

$\hat{X}_\Omega$ and $\hat{Y}_\Omega$ describe the modulation of waves with 'cos(Ωt)' and 'sin(Ωt)', referred to as the quadrature phase operators. By adding a strong classical light field $\hat{E} = \hat{E}_{\mathrm{LO}}\cos(\omega_0 t)$, referred to as the *local oscillator* (LO), a phase reference is created and the electric field becomes:

$$\hat{E}(t) = (\hat{E}_{\mathrm{LO}} + \hat{X}_\Omega)\cos(\omega_0 t) + \hat{Y}_\Omega \sin(\omega_0 t) \tag{2.21}$$

$\hat{X}_\Omega$ is labeled as the amplitude modulation operator and $\hat{Y}_\Omega$ as the phase modulation operator. In classical terms, they describe the depth of the amplitude modulation or the phase modulation of the light, respectively.

In actual experiments, the measurement is not performed instantaneously, and the time resolution $\Delta\tau$ of the detector itself has to be considered. It is defined as $\Delta\tau = 1/\Delta\Omega$, where $\Delta\Omega$, in our case, depicts the resolution bandwidth of the detector. The observable quadratures are modified to

$$\hat{X}_{\Omega,\Delta\Omega}(t) = \frac{\Delta\Omega}{2} \int_{t-(1/\Delta\Omega)}^{t+(1/\Delta\Omega)} \hat{X}_\Omega(\tau)\mathrm{d}\tau,\ \hat{Y}_{\Omega,\Delta\Omega}(t) = \frac{\Delta\Omega}{2} \int_{t-(1/\Delta\Omega)}^{t+(1/\Delta\Omega)} \hat{Y}_\Omega(\tau)\mathrm{d}\tau\,. \tag{2.22}$$

$\hat{X}_{\Omega,\Delta\Omega}$ and $\hat{Y}_{\Omega,\Delta\Omega}$ describe the amplitude or phase modulation depth at the modulation frequency $\Omega \pm \Delta\Omega/2$ [25]. Figure 2.1 shows a vacuum state at $\omega_0 \pm \Omega_1$ and a coherent state in the sideband picture at $\omega_0 \pm \Omega_2$, where for each state two sidebands are shown around the carrier field ω_0. For the vacuum state these sidebands

are empty, but they still contain the vacuum uncertainty, represented by the red circles. The upper and lower sidebands are rotating in different directions around the frequency axis.
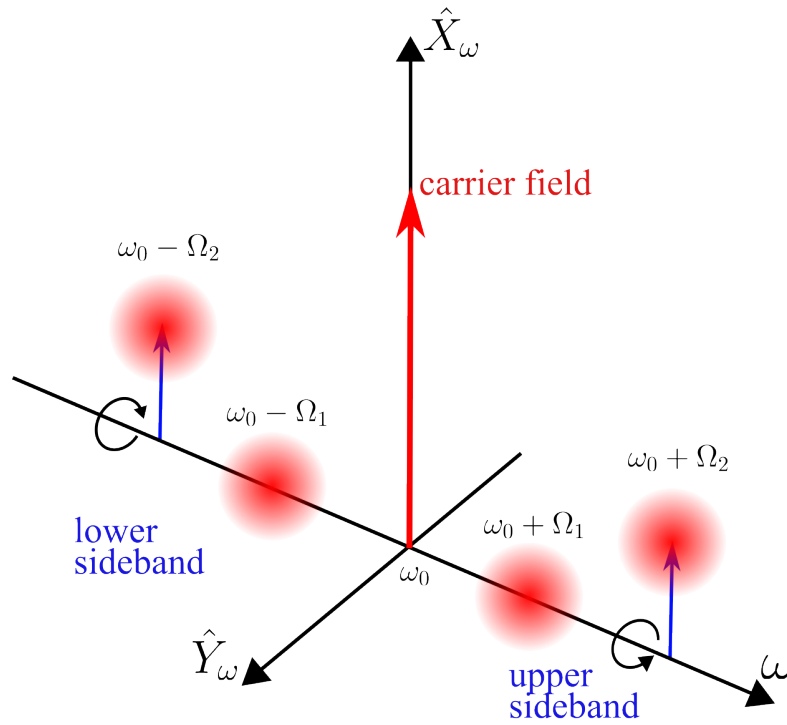
Figure 2.1 – **Representation of sideband modulations in the double sided spectrum.** Illustration from [25] of the phasors of the upper and lower sidebands at $\omega_0 \pm \Omega_{1/2}$ around the carrier field at ω_0. The sidebands are rotating in opposite directions around the frequency axis with the frequency $\pm\Omega_{1/2}$, where the sign determines the rotation direction. The red circles represent a vacuum state (see Section 2.3) at $\omega_0 \pm \Omega_1$ and a coherent state at $\omega_0 \pm \Omega_2$.

2.3 Vacuum state

The vacuum state $|0\rangle$ is the ground state of the quantum harmonic oscillator. The energy of this system is defined by its Hamiltonian

$$H = \hbar\omega \left(\hat{a}_\omega \hat{a}_\omega^\dagger + \frac{1}{2} \right) = \hbar\omega \left(\hat{n}_\omega + \frac{1}{2} \right). \tag{2.23}$$

The vacuum state is characterized by a mean photon number of zero: $\hat{n}_\omega = 0$. Applying the annihilation operator to the vacuum state results in

$$\hat{a}_\omega \left| \hat{n}_\omega \right\rangle = 0. \tag{2.24}$$

The mean value for the annihilation and the creation operator, as well as their counterparts in the two photon formalism (see equation 2.11), equals zero

$$\langle 0|\hat{a}_\omega|0\rangle = \left\langle \hat{a}_\omega \right\rangle = \left\langle \hat{a}_\omega^\dagger \right\rangle = 0, \tag{2.25}$$

$$\langle \hat{X} \rangle = \langle \hat{Y} \rangle = 0. \tag{2.26}$$

In contrast, the energy of the ground state is non-zero. Rewriting the Hamiltonian from equation 2.23 with the amplitude- and phase quadrature operator leads to

$$H = \hbar\omega \left(\hat{X}^2 + \hat{Y}^2 \right) \tag{2.27}$$

and the energy of these quadratures in the ground state is given by

$$\langle 0|\hat{X}_\omega^2|0\rangle = \frac{1}{4} = \langle 0|\hat{Y}_\omega^2|0\rangle \tag{2.28}$$

Following this result, the variance for an arbitrary operator $\hat{O}$ is the square of the standard deviation, referred to as the uncertainty, and described by $\Delta^2\hat{O} = \langle \hat{O}^2 \rangle - \langle \hat{O} \rangle^2$. For the amplitude and phase quadrature in the vacuum state with the results from 2.25 and 2.28, this uncertainty is

$$\Delta^2 \hat{X} = \frac{1}{4} = \Delta^2 \hat{Y} \,. \tag{2.29}$$

The operators obey the commutation relation $[X, Y] = \frac{i}{2}$ and satisfy the Heisenberg uncertainty relation of the form

$$(\Delta^2 \hat{X})(\Delta^2 \hat{Y}) \geq \frac{1}{16} \,. \tag{2.30}$$

2.4 Coherent state

The coherent state is defined as the eigenstate of the annihilation operator

$$\hat{a}_\omega \left| \alpha \right\rangle = \alpha \left| \alpha \right\rangle \tag{2.31}$$

with the complex eigenvalue α. It is valid to describe such a state as a vacuum state, which is displaced in phase space. Following [26], we introduce the displacement operator $D(\alpha)$, which is defined as

$$\hat{D}(\alpha) = \exp\!\big(\alpha \hat{a}^\dagger - \alpha^* \hat{a}\big)\,, \tag{2.32}$$

which leads to the representation of the coherent state as

$$\left| \alpha \right\rangle = \hat{D}(\alpha) \left| 0 \right\rangle = \exp\!\left[\int_{-\infty}^{\infty} (\alpha_\omega \hat{a}_\omega^\dagger - \alpha_\omega^* \hat{a}_\omega) \frac{\mathrm{d}\omega}{2\pi} \right] . \tag{2.33}$$

This equation can be rewritten to get the average occupation number of photons in

the n-th-state

$$|\alpha\rangle = \exp\left(\frac{1}{2}|\alpha|^2\right) \sum_n \frac{\alpha^n}{n!} |n\rangle \ . \tag{2.34}$$

In the two-photon formalism, applying a combination of the displacement operators at the sideband modulation frequencies $\pm\Omega$ results in the coherent excitation:

$$|\alpha_+, \alpha_-\rangle = \hat{D}_+(\alpha_+)\hat{D}_-(\alpha_-)|0\rangle \tag{2.35}$$

From this equation, the displacement α can be connected to the expectation values of the quadrature phase operators:

$$\langle\hat{X}\rangle = \alpha + \alpha^* = 2\,\mathrm{Re}(\alpha) \tag{2.36}$$

$$\langle\hat{Y}\rangle = \mathrm{i}(\alpha + \alpha^*) = 2\,\mathrm{Im}(\alpha) \tag{2.37}$$

The phase space description of the vacuum and the coherent state is presented in Figure 2.3 and can be described by its displacement α and the angle ϕ with $\alpha = |\alpha|\exp\{\mathrm{i}\phi\}$, where the length of this phasor is given by

$$|\alpha| = \sqrt{\langle\hat{X}\rangle^2 + \langle\hat{Y}\rangle^2}\,. \tag{2.38}$$

As stated above, the variance for $\hat{X}$ and $\hat{Y}$ of the coherent states are identical to the vacuum state described in equation 2.29.

2.5 Squeezed state

Squeezed states are non-classical states of light, which differ from both the coherent and the vacuum state. When the sideband modulations from equation 2.5 show
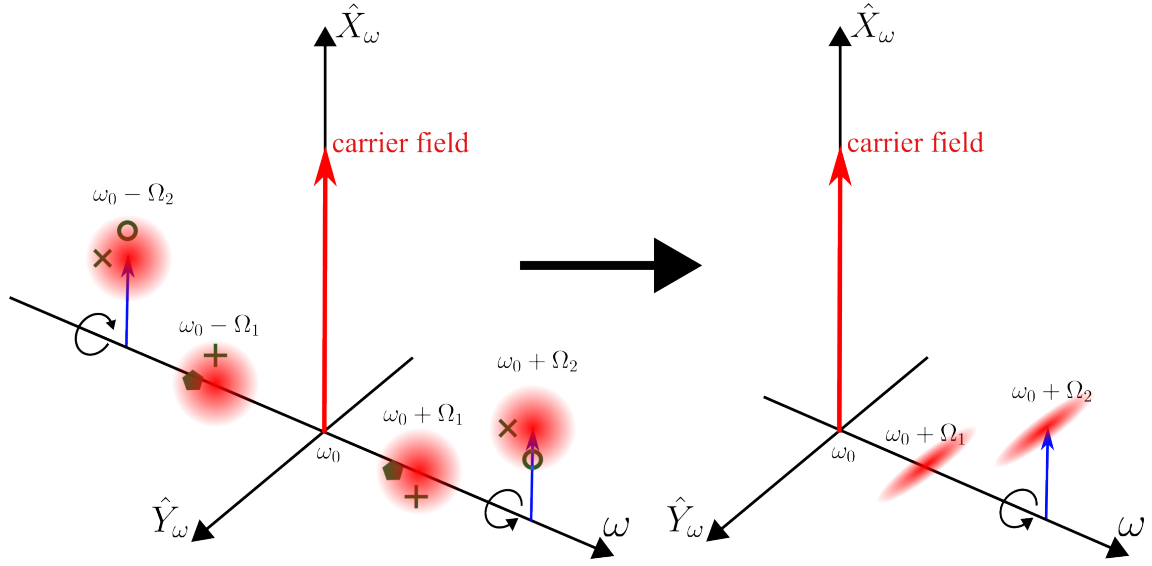
Figure 2.2 – **Generation of an amplitude squeezed state in the sideband picture.** The figure, motivated by [25], shows how an amplitude squeezed states can be visualized in the double sided (left) and single sided (right) sideband picture. In the left picture, a vacuum state at $\omega_0 \pm \Omega_1$ and a coherent state at $\omega_0 \pm \Omega_2$ show quantum correlations of squeezed states, which are depicted as different symbols. In the single sided picture, these correlations lead to the amplitude squeezed vacuum state at $\omega_0 + \Omega_1$ and the displaced amplitude squeezed state at $\omega_0 + \Omega_2$.

non-classical correlations, the uncertainties at these frequencies are entangled. This can be described by the squeeze operator:

$$\hat{S}(\zeta) = \exp\left[\int_{-\infty}^{\infty} (\zeta^* \hat{a}_+ \hat{a}_- - \zeta \hat{a}_+^\dagger \hat{a}_-^\dagger) \frac{\mathrm{d}\Omega}{2\pi}\right] \tag{2.39}$$

Here, $\zeta = r \exp(\mathrm{i}\phi)$ describes the strength of the squeezed state compared to a vacuum state, where r is the so-called *squeeze parameter* and ϕ is the *squeeze angle*, which determines the direction of the squeezed quadrature.

The unique property of the squeezed state lies in the uncertainty of its amplitude and phase quadrature. In contrast to the vacuum state (see equation 2.29) the variance of one of the quadratures is reduced below the comparable one of the vacuum state. To maintain the Heisenberg uncertainty relation (see equation 2.30) the orthogonal

quadrature is enhanced. The relation between the squeezed and the vacuum state is given by the squeeze parameter [25]

$$e^{-2r} = \frac{\Delta^2 \hat{X}_{\text{sqz}}}{\Delta^2 \hat{X}_{\text{vac}}} \,. \tag{2.40}$$
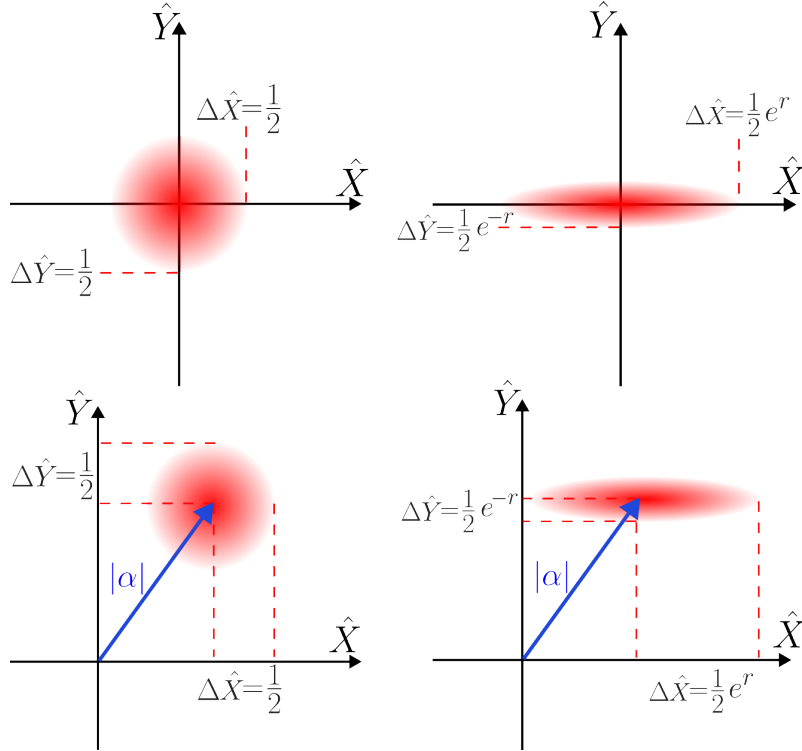
Figure 2.3 – **Phase space representation of a vacuum state, a phase squeezed vacuum state, a coherent state and a displaced phase squeezed vacuum state (from top left to bottom right).** The shown description of the different states are simplified Wigner-functions [25]. The displacement in both the bottom pictures is given by equation 2.38. The uncertainty and therefore the phase space probability is depicted by the brightness of the ellipse.

2.6 Effect of optical loss on the squeezed state

The purity of squeezed states is limited by decoherence mechanisms. Here, the most crucial factor is optical loss. For a better understanding of how optical loss
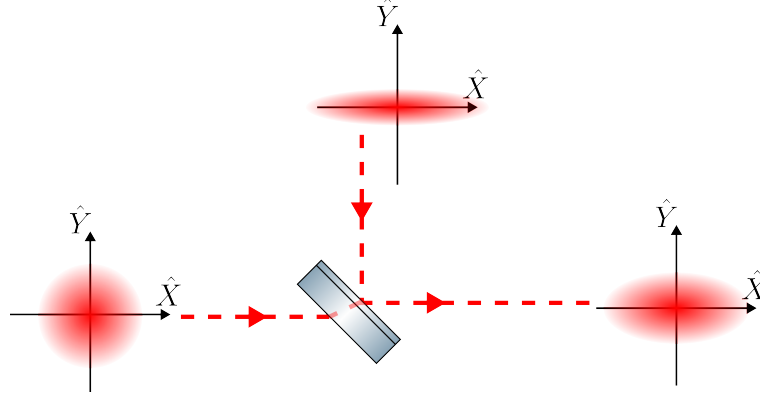
Figure 2.4 – **Influence of optical loss on the purity of a (phase) squeezed vacuum state.** A phase squeezed state shown in phase space exhibits optical loss, represented by the injection of a vacuum state on a virtual beam splitter. The squeezed state retains its non-classical properties, but the purity of the state and its squeeze parameter are diminished.

interacts with the squeezed field, Figure 2.4 depicts a strongly squeezed vacuum state sent to a virtual beam splitter with an arbitrary ratio equal to the introduced loss. As proposed by Caves in [22], one can comprehend this interaction by mixing the incoming squeezed state with a vacuum state at the beam splitter. The ratio of the beam splitter defines the ratio of the mixing of the two states. The uncertainties of the outgoing state maintain their squeezed properties and are described as a superposition of the incoming fields. The squeeze factor of the outgoing squeezed state is, however, reduced compared to the incoming one. Mathematically, the effect of optical loss on the purity of the state is described by

$$\Delta^2 \hat{X} = \eta \Delta^2 \hat{X}_{\text{sqz}} + (1 - \eta)\Delta^2 \hat{X}_{\text{vac}} \,. \tag{2.41}$$

Here, η is describing the sum of all optical losses.

In actual experiments, these losses can be caused by various sources: First is the mode-mismatch, describing the spatial mismatch between the light mode of the squeezed state and any light field mode it interacts with. In balanced homodyne detection, this usually concerns the interference between the local oscillator and the

squeezed light. In laser Doppler vibrometers (see Chapter 5) or Mach-Zehnder interferometers (see Chapter 6), the contrast of the interferometer itself contributes to the loss values as well. An additional source of optical loss are the quantum efficiencies of the photodiodes, which depend strongly on the used wavelength. Likewise, absorption or scattering on mirrors or beam splitters in the beam path of the squeezed light as well as so-called intra-cavity losses, which describes losses, that appear in the generation process of the squeezed light in the cavity, lead to contributions. A more detailed view on the experimental limitations for high squeezing values is presented in Section 3.4.

3 Generation and detection of squeezed light

In this chapter, I elaborate the process of parametric down-conversion (PDC) in cavity-enhanced optical parametric amplification (OPA), which is used to generate squeezed states in this thesis. Additionally, I illustrate two different detection schemes, balanced homodyne and balanced heterodyne detection, and highlight their features and applications. At the end of the chapter, I discuss relevant noise sources and elaborate the main experimental limitations, which occur when working with squeezed light.

3.1 Parametric down-conversion for squeezed light generation

Following equation 2.39, it becomes evident that creating a squeezed vacuum state requires the generation of correlated photon pairs. In our experiments, this is achieved through a process known as parametric down-conversion within cavity-enhanced optical parametric amplifiers. In this process, one photon with energy $E = h\lambda$, where h denotes the Planck constant and λ the wavelength, is annihilated, while simultaneously two new photons are created. Due to energy conservation, the sum of the energies of these two photons equals the energy of the initial one. In the degenerate case, both photons are identical and their wavelength is precisely twice the one of the incoming photon.

For the PDC-process to work, a nonlinear medium is required. The distinctive feature of these nonlinear media is their polarization field $P(\mathcal{E}(t))$, which responds nonlinearly to an external oscillating electric field $\mathcal{E}(t)$ [27]. By using a Taylor-approximation, the dielectric polarization becomes

$$P(\mathcal{E}(t)) = \epsilon_0(\chi^{(1)}\mathcal{E}(t) + \chi^{(2)}\mathcal{E}^2(t) + \chi^{(3)}\mathcal{E}^3(t) + ...), \tag{3.1}$$

where ϵ_0 is the dielectric permittivity of vacuum and $\chi^{(i)}$ the dielectric suscepti-bility of the i-th order. As $\chi^{(1)} \approx 1$ is typically much larger than $\chi^{(i)}$, $i > 1$, the polarization in linear dielectric materials scales linearly with the electric field. How-ever, in nonlinear crystals, $\chi^{(2)}$ can reach values on the order of $10^{-12}\,\frac{\text{m}}{\text{V}}$. For high electric field strengths or correspondingly high intensities, the polarization response becomes quadratic. Higher order linearities are possible as well, with the so-called optical Kerr-effect relying on third order nonlinearity. These effects typically re-quire even higher intensities, often generated by using pulsed lasers [28]. Typically used nonlinear media are lithium niobate (LiNbO$_3$), barium borate (BBO) or, in our experiments, potassium titanyl phosphate (KTP).

Optical parametric amplifiers, which are extensively used in this thesis, take advan-tage of the second-order nonlinearity. An oscillating electric field $\mathcal{E}$ with a frequency ω_0 can be described by $\mathcal{E}(t) = \mathcal{E}_0 \cos(\omega_0 t)$. The polarization in second order can be expanded with:

$$P^{(2)}(\mathcal{E}(t)) = \epsilon_0\chi^{(2)}\mathcal{E}^2(t) = \epsilon_0\chi^{(2)}\frac{\mathcal{E}_0}{2}(1 + \cos(2\omega_0 t)) \tag{3.2}$$

This second order term now oscillates at twice the initial frequency $2\omega_0$. This in-teraction can be described as a three-photon process, involving two photons with frequencies of $\omega_\pm = \omega_0 \pm \Omega$, which are called signal and idler, and one photon at their sum frequency $2\omega_0$. In the degenerate case, where $\Omega = 0$, signal and idler photons are identical.

For a better understanding of the creation of squeezed states in a degenerate type

I OPA, we follow a graphical description first presented in [25] and [29], which is illustrated in Figure 3.1. Here, a small section of a nonlinear medium is pumped with light at the optical frequency of $2\omega_0$. Additionally, a vacuum state at the fundamental frequency ω is superimposed with the pump field, resulting in an incoming electrical field $\mathcal{E}^{\text{in}} = \mathcal{E}^{\text{in}}_\omega + \mathcal{E}^{\text{in}}_{2\omega}$. When this field interacts with the nonlinear crystal, a nonlinear response of the dielectric polarization $P(\mathcal{E})$ is generated, which creates the outgoing electric field $\mathcal{E}^{\text{out}} = \mathcal{E}^{\text{out}}_{\text{sqz}, \omega} + \mathcal{E}^{\text{out}}_{2\omega} + \mathcal{E}^{\text{out}}_{4\omega}$. The term $\mathcal{E}^{\text{out}}_{\text{sqz}, \omega}$ represents the squeezed vacuum state at the fundamental frequency ω, while $\mathcal{E}^{\text{out}}_{2\omega}$ and $\mathcal{E}^{\text{out}}_{4\omega}$ correspond to two classical optical fields leaving the nonlinear medium. These classical fields are created by the response of the polarization to the incoming light field $\mathcal{E}^{\text{out}}_{2\omega}$ in first (P^1) and second (P^2) order.

3.2 Phase matching

It is important to note, that the process illustrated in Figure 3.1 only describes the interaction of the nonlinear medium in a small section of the crystal. To achieve a meaningful conversion, the effect of optical parametric amplification must occur throughout the whole crystal length. This requires the fundamental field at ω_0 and the second harmonic field at $2\omega_0$ to co-propagate in the crystal with the same speed. Due to the dispersion of the nonlinear medium, however, light fields with different wavelengths experience different refractive indices while propagating through a nonlinear medium, resulting in a varying phase relation. The *phase matching*-process is used keep this phase relation constant. For the wavefronts of both fields to travel at the same velocity inside the crystal the phase matching condition is introduced as

$$|\vec{k}_{\omega_+} + \vec{k}_{\omega_-} - \vec{k}_{2\omega}| = 0 \tag{3.3}$$

at which the wave vectors of the photons at the fundamental frequency and the one of the second harmonic cancel each other.
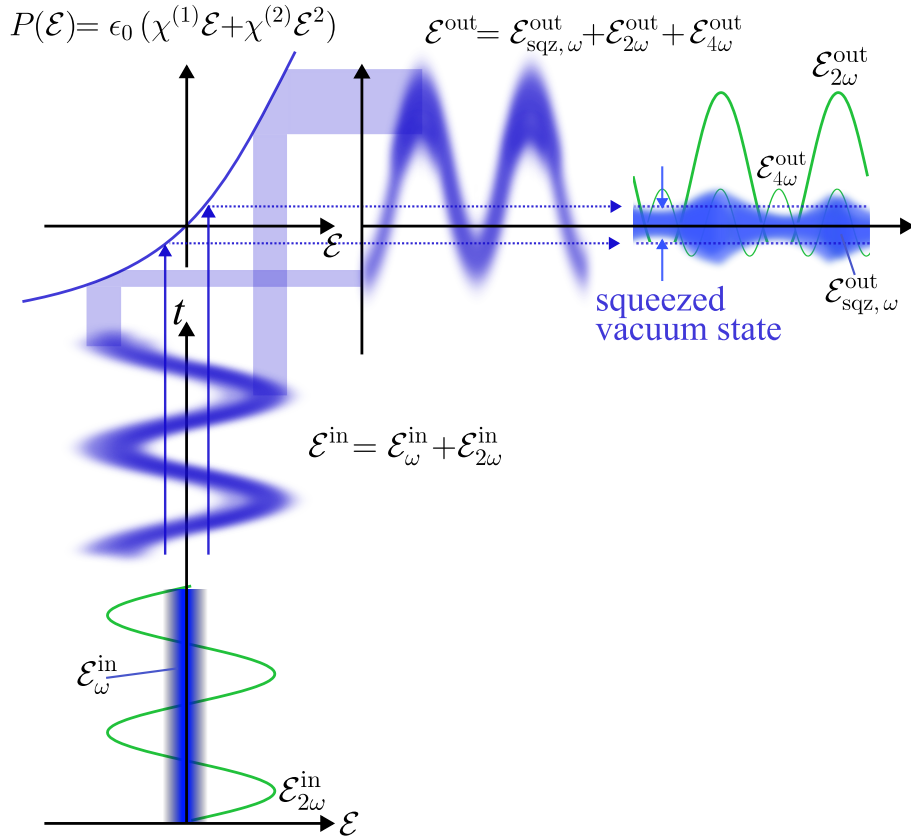
Figure 3.1 – **Optical parametric amplification process for the creation of a squeezed vacuum state.** The picture displays a incoming electrical field $\mathcal{E}^{\text{in}}$, consisting of a classical bright field $\mathcal{E}^{\text{in}}_{2\omega}$ and a vacuum field $\mathcal{E}^{\text{in}}_{\omega}$, which interacts with a nonlinear medium. Its polarization is approximated to its second order $P(\mathcal{E}) = \epsilon_0(\chi^{(1)}\mathcal{E} + \chi^{(2)}\mathcal{E}^2)$ and depicted as the parabolic curve in the top left corner. The outgoing electrical field $\mathcal{E}^{\text{out}}$ is composed of the classical fields $\mathcal{E}^{\text{out}}_{2\omega}$ and $\mathcal{E}^{\text{out}}_{4\omega}$ and a squeezed vacuum field $\mathcal{E}^{\text{out}}_{\text{sqz},\,\omega}$. The figure is adapted from [25, 29].

Achieving true phase matching, conventionally referred to as type I or II phase matching, leverages the birefringence of the nonlinear medium along with different polarization of the fundamental and second harmonic light field. By considering the temperature dependence of the refractive indices, a temperature can be found where the phase matching condition is fulfilled.

In our experiments, we utilize quasi-phase matching (QPM), which is sometimes referred to as type 0 phase matching. Figure 3.2 depicts the difference between true
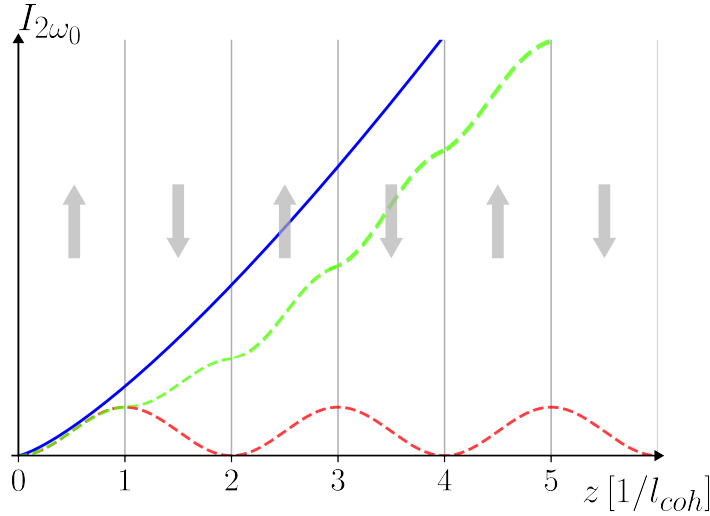
Figure 3.2 – **Impact of phase matching on the conversion efficiency in a nonlinear crystal.** The figure, adapted from [30], shows the difference of optimal phase matching (blue), quasi-phase matching (green) and no phase matching (red) in a nonlinear medium. For optimal phase matching, the intensity of the second harmonic field $I_{2\omega_0}$ is increasing continuously while propagating through the crystal. For no phase matching, the phase drift between the two fields leads to almost no conversion, as the conversion process is inverted after a distance of one coherence length. The gray arrows imply the periodically poling of the crystal for quasi-phase matching. Here, the conversion increases continuously similar to true phase matching but weaker gradient.

phase matching, QPM and no phase matching in a nonlinear crystal. For QPM, equation 3.3 is not entirely fulfilled and the two light fields are allowed to drift in relation to each other over a small range. After the so-called coherence length l_{coh}, the susceptibility in the crystal section is changed, and the phase drift is reversed. For this change, quasi-phase matching requires a periodic poling of the crystal, which is performed by applying a strong, periodically changing electric field in the generation process of the crystal. The length of these domains is usually in the range of tens of µm.

The effective nonlinear coefficient of quasi-phase matching is reduced by a factor of $2/\pi$ compared to true phase matching [31]. QPM can still produce a higher conversion efficiency as all three involved light fields are usually in the same polarization.

23

As the effective nonlinear coefficient, which determines the conversion efficiency, depends on the polarization, in some cases even the reduced factor of QPM can lead to more effective results than type I or II phase matching.

3.3 Detection schemes

There are multiple ways to detect squeezed states of light. The simplest one is the detection with one single photodiode, which is only sensitive to amplitude modulations. For the readout of arbitrary quadratures, balanced detection schemes are used. In this section, I introduce balanced homodyne and heterodyne detection and elaborate their differences in terms of noise contribution and applicability.

3.3.1 The balanced homodyne detector

Balanced homodyne detection (BHD) is a readout scheme used to detect amplitude or phase modulations of oscillating signals by overlapping the signal with a bright field of the same frequency f_0, referred to as the *local oscillator*. It is the state-of-the-art detection method for squeezed states of lights. In BHD the readout quadrature can be varied by changing the phase θ between the signal and the local oscillator. Additionally, classical noise contributions such as amplitude noise, which are elaborated in detail in Section 3.4.1, are suppressed.

Figure 3.3 depicts the setup used for balanced homodyne detection. The local oscillator field is sent onto a 50:50-beam splitter. Here, it is overlapped with the signal beam, which for squeezed light detection is replaced with the squeezed vacuum state. Two photodiodes measure the light in both of the outputs of the beam splitter. Their current is subtracted and analyzed on a spectrum analyzer. With a phaseshifter in one of the arms, the phase θ between the two fields can be varied, which results in the readout of arbitrary quadratures.

We can describe the two incoming light fields $\hat{L}$ and $\hat{S}$ with
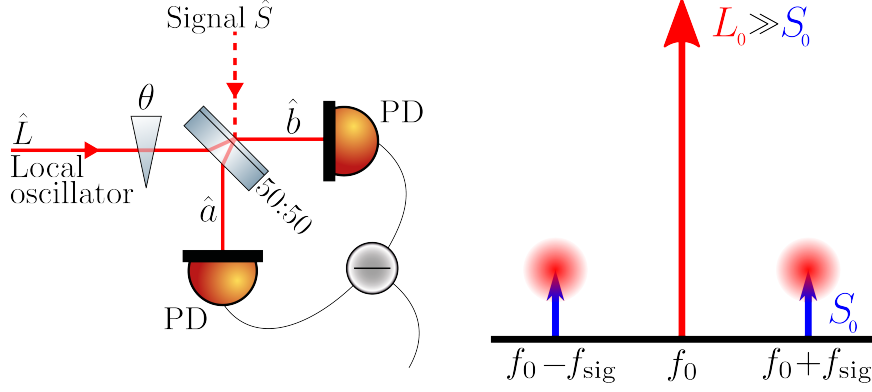
Figure 3.3 – **Simplified scheme of a balanced homodyne detector and its representation in the simplified sideband picture. Left:** Schematic of the signal field $\hat{S}$ overlapped with the local oscillator $\hat{L}$ on a 50:50-beam splitter. The outgoing fields $\hat{a}$ and $\hat{b}$ are detected on two separate photodiodes (PD). Their currents are subtracted and evaluated. By placing a phaseshifter in one of the incoming arms, the phase θ can be changed, resulting in different readout quadratures. **Right:** The local oscillator (red) at f_0 is surrounded by sidebands at $f_0 \pm f_{\text{sig}}$ (blue), which are created by the signal. L_0 and S_0 display the strength of the fields, where $L_0 \gg S_0$. The red circles on top of the phasors represent the quantum noise. The noise contribution of the local oscillator is neglected due to the homodyne approximation.

$$\hat{L} = \left\langle \hat{L} \middle| \hat{L} \right\rangle + \delta \hat{l} = L_0 + \delta \hat{l}\,, \qquad (3.4)$$

$$\hat{S} = \left\langle \hat{S} \middle| \hat{S} \right\rangle + \delta \hat{s} = S_0 + \delta \hat{s}\,, \qquad (3.5)$$

where L_0 and S_0 are the expectation value of the relative operator and $\delta \hat{l}$ and $\delta \hat{s}$ define their fluctuations. Following [24, 32], the outgoing states $\hat{a}$ and $\hat{b}$ after the beam splitter can be described by

$$\begin{pmatrix} \hat{a} \\ \hat{b} \end{pmatrix} = \frac{1}{\sqrt{2}} \begin{pmatrix} 1 & 1 \\ 1 & -1 \end{pmatrix} \begin{pmatrix} \hat{L}e^{i\theta} \\ \hat{S} \end{pmatrix} = \frac{1}{\sqrt{2}} \begin{pmatrix} \hat{L}e^{i\theta} + \hat{S} \\ \hat{L}e^{i\theta} - \hat{S} \end{pmatrix}\,, \qquad (3.6)$$

25

where $e^{i\theta}$ represents the influence of the phase between the two fields. The photo currents $\hat{I}_a$ and $\hat{I}_b$ of both photodiodes are directly proportional to the photon numbers $\hat{n}_a$ and $\hat{n}_b$.

$$\hat{I}_a \propto \hat{n}_a = \hat{a}^\dagger \hat{a} = \frac{1}{2}(\hat{L}^\dagger \hat{L} + \hat{S}^\dagger \hat{S} + \hat{L}^\dagger \hat{S} e^{-i\theta} + \hat{S}^\dagger \hat{L} e^{i\theta})$$
$$\hat{I}_b \propto \hat{n}_b = \hat{b}^\dagger \hat{b} = \frac{1}{2}(\hat{L}^\dagger \hat{L} + \hat{S}^\dagger \hat{S} - \hat{L}^\dagger \hat{S} e^{-i\theta} - \hat{S}^\dagger \hat{L} e^{i\theta})$$

(3.7)

Subtracting the currents leads to

$$\begin{aligned}
\hat{I}_- \propto \hat{n}_- &= \hat{n}_a - \hat{n}_b \\
&= \hat{L}^\dagger \hat{S} e^{-i\theta} + \hat{S}^\dagger \hat{L} e^{i\theta} \\
&= (L_0^* S_0 + L_0^* \delta\hat{s} + \delta\hat{l}^\dagger S_0 + \delta\hat{l}^\dagger \delta\hat{s})e^{-i\theta} \\
&\quad + (S_0^* L_0 + S_0^* \delta\hat{l} + \delta\hat{s}^\dagger L_0 + \delta\hat{s}^\dagger \delta\hat{l})e^{i\theta}.
\end{aligned}$$

(3.8)

With $L_0^* = L_0$, $S_0^* = S_0$ and the definition $\delta\hat{l}e^{-i\theta} + \delta\hat{l}^\dagger e^{i\theta} \equiv \hat{X}_\theta = \hat{X}\cos\theta + \hat{Y}\sin\theta$, it follows that

$$\hat{n}_- = 2\cos\theta L_0 S_0 + L_0 \hat{X}_\theta^S + S_0 \hat{X}_\theta^L + \delta\hat{l}^\dagger \delta\hat{s} e^{-i\theta} + \delta\hat{s}^\dagger \delta\hat{l} e^{i\theta}.$$

(3.9)

Here, $\hat{X}$ and $\hat{Y}$ describe the amplitude- and the phase quadrature respectively. With the assumption, that the fluctuation of the signal $\delta\hat{s}$ and the local oscillator $\delta\hat{l}$ are much smaller than their amplitudes, so that $|L_0 \hat{X}_\theta^S| \gg |\delta\hat{l}^\dagger \delta\hat{s}|$ and $|L_0 \hat{X}_\theta^S| \gg |\delta\hat{s}^\dagger \delta\hat{l}|$, as well as that the amplitude of the local oscillator is much larger than the signal $L_0 \gg S_0$, we can simplify the equation above. Due to $|L_0 \hat{X}_\theta^S| \gg |S_0 \hat{X}_\theta^L|$, fluctuations of the local oscillator can be neglected, which is referred to as the homodyne approximation. Following [25] the difference of the photo currents at the sideband frequency $\Omega \pm \Delta\Omega/2$ with the bandwidth $\Delta\Omega$ leads to

$$\hat{I}_{\Omega,\Delta\Omega}^-(t) \propto \hat{n}_{\Omega,\Delta\Omega}^-(t) \approx L_0 \hat{X}_{\theta,\Omega,\Delta\Omega}^S(t).$$

(3.10)

Equation 3.10 directly shows, that the signal quadrature is amplified by the local oscillator.

3.3.2 Comparison of heterodyne and homodyne detection schemes
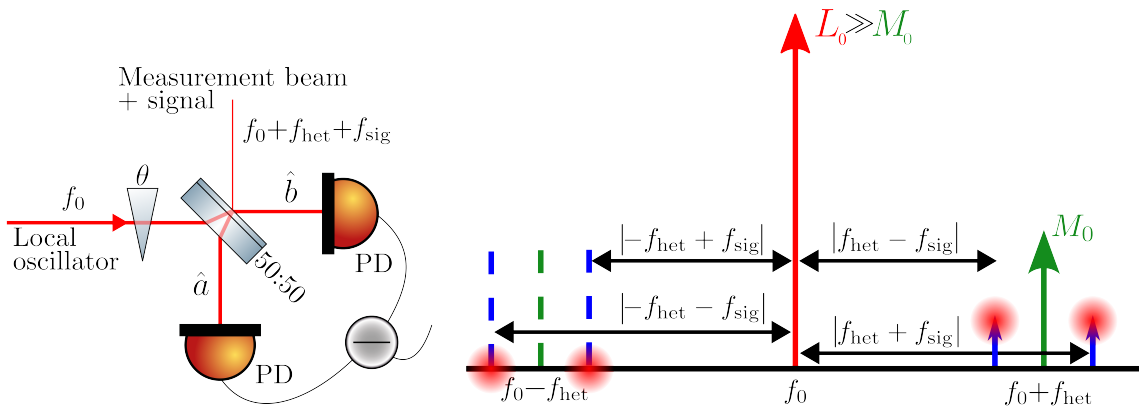
Figure 3.4 – **Balanced heterodyne detection and its sideband contributions**
Left: Schematic of the signal field $\hat{S}$ at the frequency f_{sig}, which is shifted together with the measurement beam at f_{het}, overlapped with the local oscillator $\hat{L}$ on a 50:50-beam splitter at f_0. The outgoing fields $\hat{a}$ and $\hat{b}$ are detected on two separate photodiodes (PD). Their currents are subtracted and evaluated. By placing a phaseshifter in one of the incoming arms the phase θ can be changed, resulting in different readout quadratures. **Right:** The signal (blue) appears as sidebands around the measurement beam, which is beating with the local oscillator (red). L_0 and M_0 display the strength of the LO and the measurement beam, with $L_0 \gg M_0$. The red circles on top of the signal represent the quantum shot noise. Due to energy conservation the empty sideband at $f_0 - f_{\text{het}}$ also contains noise at $f_0 - f_{\text{het}} \pm f_{\text{sig}}$. The noise contribution is twice as high compared to the homodyne detection readout.

Balanced heterodyne detection is the second readout scheme used in this thesis. Here, either the signal beam or the local oscillator is frequency shifted with respect to the other field before it is overlapped at the beam splitter. The frequency shift is usually performed with an acousto-optic modulator and numbers at tens to hundreds

of MHz. The readout contains a measurement beam, which amplitude M_0 is much smaller than the local oscillator L_0. In the left picture of Figure 3.4, the measurement beam acquires the signal sidebands and interferes on a balanced beam splitter with the LO. The readout of the outputs of this beam splitter is identical to the balanced homodyne detection scheme.

There are some notable differences between homodyne and heterodyne detection: First, heterodyne detection allows the detection of signals with high amplitudes. Here, homodyne detection is restricted as one can only detect signals which are smaller than one interference fringe. Next, not only the detection frequency of the signal is shifted to $f_0 + f_{\mathrm{het}} + f_{\mathrm{sig}}$, but the relevant electronic noise of the detector as well, which we refer to as the *dark noise* (see Section 3.4.1). A detector with low dark noise is essential for interferometric measurements, but becomes more and more challenging when moving towards smaller frequencies below 100 Hz. Heterodyne detection allows the shift of the measurement frequency to a frequency, where the dark noise becomes neglectable. Last, the readout of the measurement requires no phase stabilization between the measurement beam and the local oscillator. The readout of arbitrary quadratures is performed by demodulating the output signal with different functions. In contrast, homodyne readout is typically performed either at the dark fringe of the interferometer, which is used in gravitational wave detector, or at the mid fringe, which is done in the Mach-Zehnder interferometer used in Chapter 6.

On the other hand the shot noise in a heterodyne detection scheme is fundamentally twice as high as its homodyne counterpart [33, 34]. This is illustrated in the right picture of Figure 3.4. The measurement beam is shifted in reference to the local oscillator while the signal sidebands at $f_0 + f_{\mathrm{het}} \pm f_{\mathrm{sig}}$ are located around the carrier frequency $f_0 + f_{\mathrm{het}}$. Simultaneously due to energy conservation sidebands at $f_0 - f_{\mathrm{het}} \pm f_{\mathrm{sig}}$ are created. They do not preserve any amplitude, but they still contribute to the overall quantum noise. This additional noise term leads to the enhanced shot noise level in heterodyne detection schemes.

Most experiments performed throughout this thesis use the balanced homodyne readout. In the squeezed light enhanced laser Doppler vibrometer in Chapter 5

both homodyne and heterodyne detection schemes are used.

3.3.3 Squeezed light enhancement in heterodyne detection
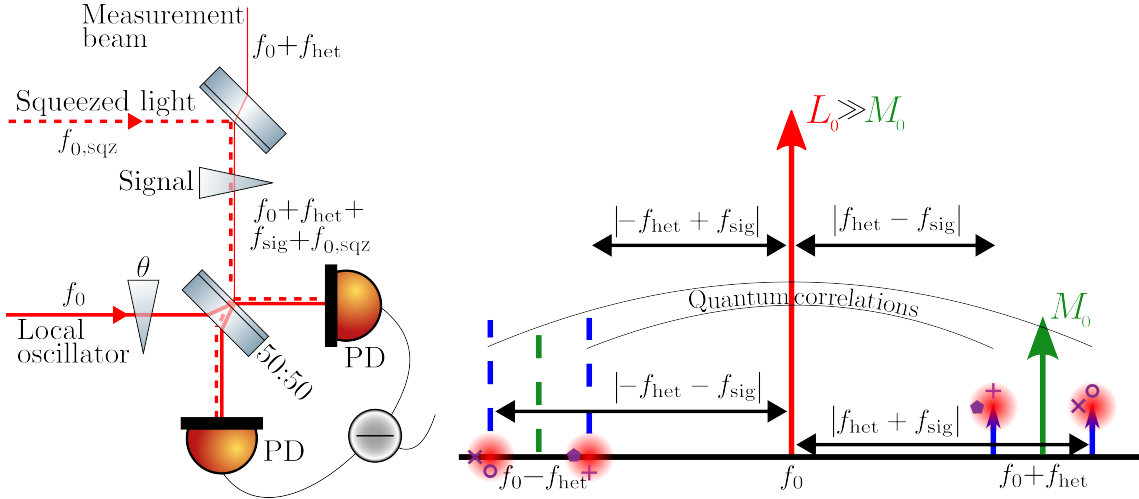
Figure 3.5 – **Influence of squeezed light in a balanced heterodyne detection scheme. Left:** Squeezed light, produced at the frequency f_0, is overlapped on a beam splitter with the measurement beam. Both fields acquire the signal at $f_{het} \pm f_{sig}$ and interfere with the local oscillator on a second beam splitter with a 50:50 ratio. **Right:** The implementation of squeezed light generates quantum correlations, shown in the left picture. The squeezed states create entanglement between the sidebands and can therefore reduce the quantum shot noise. This correlations are depicted as the purple symbols on top of the shot noise.

Similar to homodyne readout schemes, squeezed light can also be implemented in interferometric setups which utilize heterodyne detection. Figure 3.5 displays how a squeezed field at frequency f_0 creates correlations between the different sidebands. The squeezed state is overlapped on a beam splitter with the measurement beam which then acquires the signal sidebands. Next, the measurement beam and the squeezed light are superimposed with the local oscillator.

The correlations created by the squeezed light are represented by the black curves in the right picture of Figure 3.5. Here, the signal at $f_0 + f_{het} - f_{sig}$ is correlated with the corresponding one at $f_0 - f_{het} + f_{sig}$. In this spectrum, the distance between local

oscillator and the signal sideband is identical and equals $|f_{\text{het}} - f_{\text{sig}}|$. Consequently, the two sidebands at $f_0 - f_{\text{het}} - f_{\text{sig}}$ and $f_0 + f_{\text{het}} + f_{\text{sig}}$ are entangled as well. The correlations are depicted by the circles and crosses inside the quantum noise. This illustration was introduced in Section 2.5. In the measurement process, this spectrum is folded around the local oscillator frequency, resulting in a squeezed state replacing the original vacuum state.

3.4 Experimental limitations for squeezed light detection

Theoretically, squeezed states with infinite squeezing can be produced. Due to different noise contributions and decoherence effects, introduced in Section 2.6, however, the detectable squeezing values are limited.

3.4.1 Noise sources

Squeezed states of light are only able to reduce the quantum noise in the experiment, but there are multiple other classical noise sources, which have to be minimized to see a sensitivity enhancement. In this work, the strongest noise contributions are:

Shot noise: The fundamental quantum shot noise forms, together with the quantum radiation pressure noise, the quantum noise. For low laser powers, the shot noise is the dominating term of these two and whenever I use the term quantum noise, I refer to the quantum shot noise. Quantum noise derives directly from the Heisenberg uncertainty relation. It can be visualized in the following way: When laser light is detected on a photodiode, all of the photons of the laser beam are uncorrelated in time. This means that their arrival on the detector is random and results in uncertainty, which we refer to as shot noise.

The shot noise itself is frequency independent and proportional to $\sqrt{P_{\text{in}}}$, where P_{in}

describes the optical power in the interferometer. There are two ways to increase the sensitivity in a shot noise limited interferometer: The first one is increasing the optical input power. Due to the signal in the interferometer scaling with P_{in}, the signal-to-noise ratio (SNR), which describes the sensitivity of the system, is given by

$$\text{SNR} = \frac{S_{\text{sig}}}{S_{\text{sn}}} \propto \frac{P_{\text{in}}}{\sqrt{P_{\text{in}}}} = \sqrt{P_{\text{in}}} \,. \tag{3.11}$$

The second way is injecting a squeezed vacuum state. Here, the shot noise is directly decreased and this decrease is proportional to the squeeze factor β, which is connected to the squeeze parameter from Section 2.5 by $r = \ln(\beta/2)$. In this case, the signal-to-noise ratio is

$$\text{SNR} = \frac{S_{\text{sig}}}{\beta S_{\text{sn}}} \,. \tag{3.12}$$

Dark noise of the detector: The electrical dark noise of the photo detector is caused by the generated noise of the transimpedance amplifier, which is required to stabilize and enhance the detected signals. The choice of this transimpedance amplifier is crucial and depends on the needs of the experiments [35]. Here, the gain-bandwidth product prevents the detector from having both low dark noise values and a high detection frequency range simultaneously. In contrast to the shot noise, the dark noise is independent from the light power. Therefore, enhancing the light power directly reduces the influence of the dark noise on the measurement.

Technical laser noise: This noise is caused by fluctuations of the seed laser in frequency and amplitude.

Frequency noise for interferometric measurements describes small changes in the wavelength of the laser light and can be mitigated by matching the arm lengths of the interferometer arms.

Amplitude noise characterizes power fluctuations in the output power of the laser. It is characterized by the relative intensity noise (RIN) of the laser, which describes

the quotient of the measured noise to the average mean power. Amplitude noise scales linearly with the optical power and depends on the properties of seed laser of the experiment. Balanced detection schemes are used to suppress the effect of amplitude noise. Here, the splitting ratio at the beam splitter determines how strong the amplitude noise couples into the measurement. As the noise is correlated in both arms, a ideal 50:50-beam splitter together with photodiodes with identical quantum efficiency lead to the complete subtraction of amplitude noise. For the measurements conducted in this thesis, the technical laser noise was minimized and did not interfere with the measurements.

Phase noise: Phase noise describes noise that occurs due to the difference between the squeezing angle of the ellipse and the readout angle of the measurement [36, 37] and can be illustrated by a periodic jitter of the squeezing ellipse. The detected squeezing value is in this case the projection of the squeezing ellipse on the desired quadrature. Especially for high anti-squeezing values this jitter can reduce the squeezing value drastically, while the effect on the anti-squeezing value is neglectable. To distinguish phase noise from other noise sources, one can steadily increase the pump power of the system and trace the anti-squeezing and squeezing value. As mentioned before the anti-squeezing values will increase with rising pump power, while the squeezing values reach a maximum and drop afterwords [38]. Main causes for phase noise are acoustic oscillations, for example due to vibrating mirrors, or unstable control locking systems of the length of the cavities.

3.4.2 Optical loss and cavity bandwidth

Following [39], the squeezed and anti-squeezed spectrum produced by optical parametric amplification below threshold are given by

$$S_{\text{sqz,asqz}}(f) = 1 \mp \eta \frac{4\sqrt{\frac{P}{P_{\text{thr}}}}}{\left(1 \pm \frac{P}{P_{\text{thr}}}\right)^2 + 4\left(\frac{2\pi f}{\gamma}\right)^2} \,. \tag{3.13}$$

Here, f is the measurement frequency, η the efficiency of the system, P the pump power of the cavity, P_{thr} the threshold power and γ the bandwidth of the cavity. The optical loss is given by $\epsilon = 1 - \eta$. The spectra are normalized to the shot noise, which is frequency-independent, for $P = 0$, where $S = 1$.

In the squeeze lasers described in this thesis the two limiting factors for achieving high squeezing values are the optical loss and the cavity bandwidth.

Optical loss

Optical loss, introduced in Chapter 2, describes the overall loss in the system, which main contributions are absorption or scattering of optics, the quantum efficiency of the photodiodes, the spatial mismatch between the local oscillator and the squeezed field and internal losses in the cavity itself. Based on equation 3.13, Figure 3.6 depicts how optical loss, denoted by the values next to the respective trace, influences the detectable squeezing (blue) and anti-squeezing (red) spectra with $\gamma/2\pi = 100\,\mathrm{MHz}$ and $\frac{P}{P_{\mathrm{thr}}} = 0.8$. Both quadratures are normalized to the white shot noise at $0\,\mathrm{dB}$.

If there is no optical loss present in the setup, both spectra are identical. For $5\,\%$, $10\,\%$ and $15\,\%$ the squeezed level is decreasing rapidly while the anti-squeezed one is only influenced slightly. At low frequencies, 10% of optical loss prevents the detection of more than $10\,\mathrm{dB}$ of squeezing, even for arbitrary high values of anti-squeezing.

By detecting the squeezed and anti-squeezed values for identical pump powers, the efficiency and therefore the optical loss can be calculated. Following [21], the efficiency η of the system is given by

$$\eta = 1 - \frac{1 - S_{\eta,\mathrm{sqz}}(f)S_{\eta,\mathrm{asqz}}(f)}{2 - S_{\eta,\mathrm{sqz}}(f) - S_{\eta,\mathrm{asqz}}(f)} \,. \tag{3.14}$$

For all measurements in this thesis, the optical loss is derived from the efficiency, which is calculated with this formula.
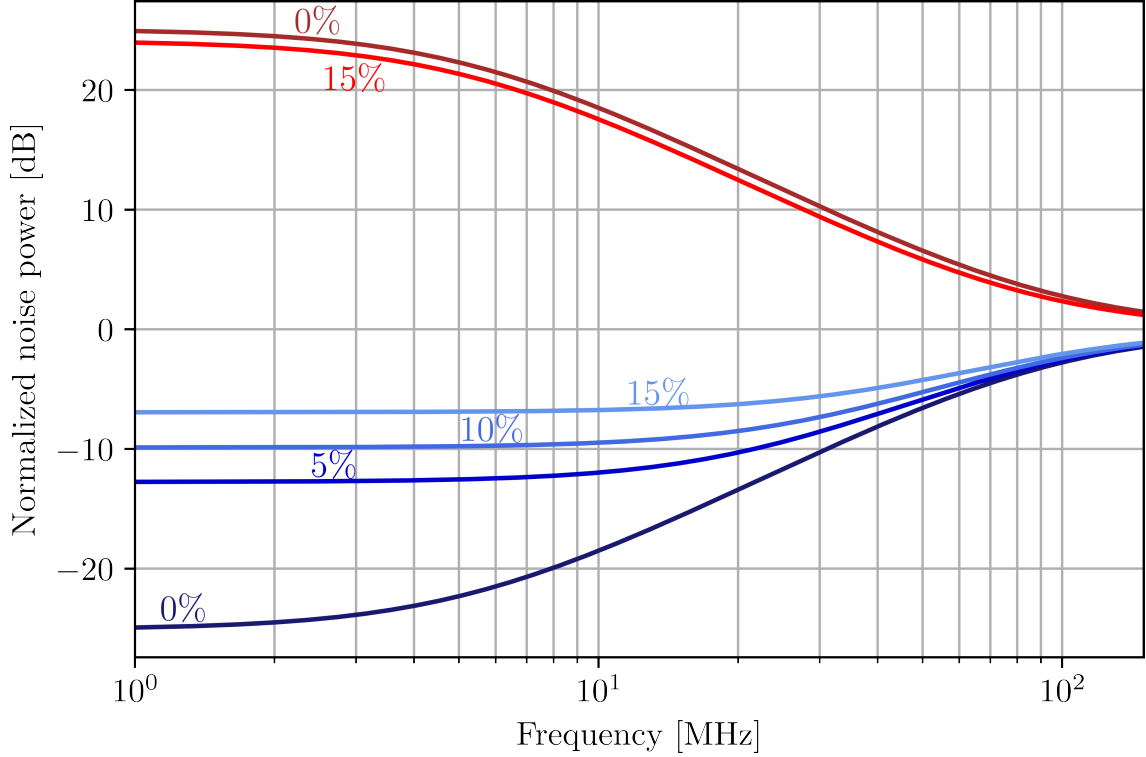
Figure 3.6 – **Influence of different optical loss values on the squeezed (blue) and anti-squeezed (red) spectra.** The traces are normalized to the shot noise at $0\,\mathrm{dB}$ with the anti-squeezed spectra above and the squeezed ones below. The decrease of the spectra for $0\,\%$, $5\,\%$, $10\,\%$ and $15\,\%$ of optical loss was calculated according to equation 3.13 with $\gamma/2\pi = 100\,\mathrm{MHz}$ and $\frac{P}{P_{\mathrm{thr}}} = 0.8$. Clearly visible, the squeezed values are much more vulnerable to optical loss compared to the anti-squeezed values, where optical loss can typically be neglected.

Cavity-bandwidth

The optical bandwidth of the parametric down-conversion cavity is the another limiting factor in our measurements. It is defined as the quotient between the free spectral range (FSR) and the finesse F of the cavity. For linear cavities, the bandwidth is

$$\gamma = \frac{\mathrm{FSR}}{F}\,, \tag{3.15}$$

with

$$\text{FSR} = \frac{c}{2L}, \ F = \frac{2\pi}{1 - r_1 r_2} \,. \tag{3.16}$$

Here, c is the speed of light, L the cavity length and r_1 and r_2 are the amplitude reflectivities of the mirror forming of the cavity. Figure 3.7 shows how squeezing and anti-squeezing spectra change for different bandwidths when there is no optical loss ($\eta = 1$) present. The pump power remained at $\frac{P}{P_{\text{thr}}} = 0.8$. For lower frequencies the detectable squeezed values are almost identical. Moving to higher frequencies, a cavity with the a bandwidth of $\gamma/2\pi = 100\,\text{MHz}$ is only able to detect $10\,\text{dB}$ of squeezing until $f = 30\,\text{MHz}$.
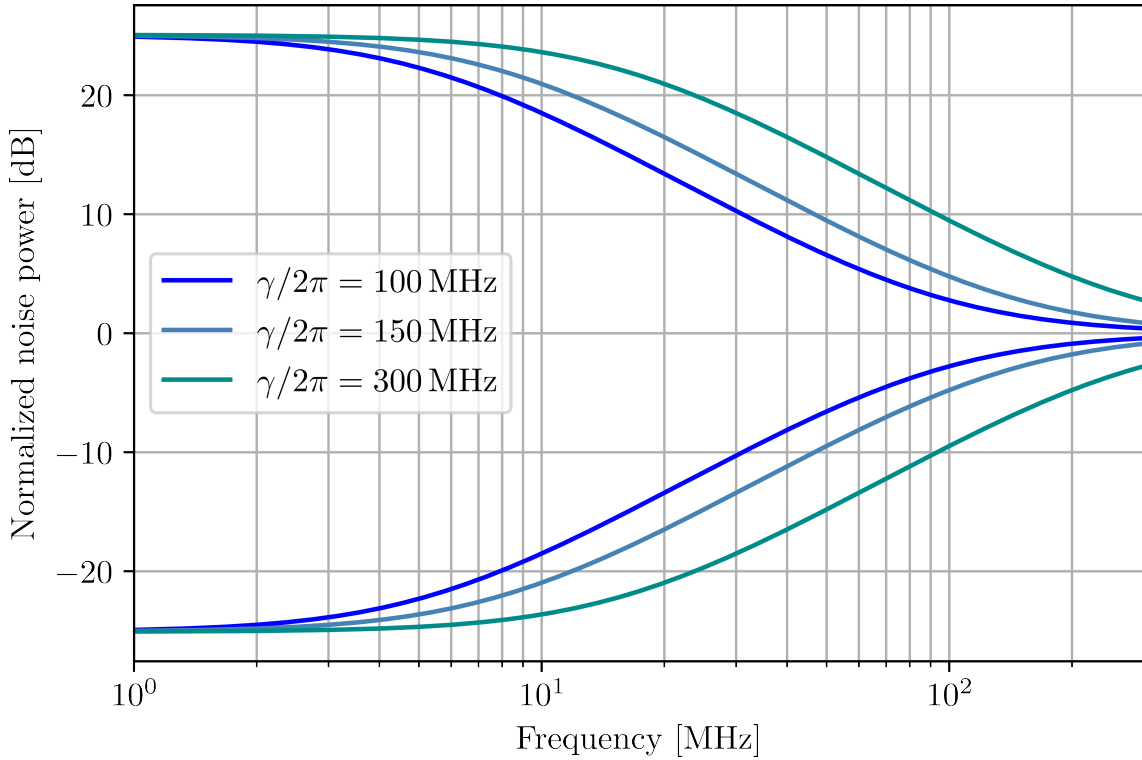
Figure 3.7 – **Influence of the bandwidth on the spectrum of the squeezed and anti-squeezed noise.** The traces show the squeezed (negative values) and anti-squeezed (positive values) spectra normalized to the shot noise at $0\,\text{dB}$ according to equation 3.13 with $\eta = 1$ and $\frac{P}{P_{\text{thr}}} = 0.8$. For high frequencies the bandwidth becomes a major factor in limiting the detectable squeezing.

4 The experimental realization of a squeeze laser

Squeezed light can improve the sensitivity of any shot noise limited laser-based detection scheme. Previously, the setups, which produces these squeezed states, were labeled as a squeezed light source. In [40], the denotation of a *squeeze laser* was introduced, which will be used in this thesis to describe devices, that are able to produce amplitude - or phase squeezed states of light. In recent history, the size of these squeeze lasers was constantly reduced: In 2010, the size of the setup for the generation of squeezed states in the gravitational wave detector GEO600 in Hannover numbered $1.35\,\text{m} \times 1.15\,\text{m}$. More recently in 2018 and 2019, the size was reduced to fit on $80\,\text{cm} \times 80\,\text{cm}$ and $80\,\text{cm} \times 100\,\text{cm}$-breadboards, respectively [21, 41]. This size and weight reduction allows faster transportation and easier implementation in other interferometric setups. In this chapter, I first discuss the general design and setup by using the example of a squeeze laser I set up on a $80\,\text{cm} \times 80\,\text{cm}$-breadboard. I highlight the features of this setup and compare different cavity designs in terms of performance, stability and their implementation in external experiments. Next, I present a more compact version of the squeeze laser, set up on a $60\,\text{cm} \times 40\,\text{cm}$-breadboard. In the end, I will make a comparison between the here presented squeeze lasers with similar experiments shown in [21], [29] and in the PhD thesis of Malte Hagemann.

4.1 Setup of the squeeze laser

To produce strongly squeezed and stable vacuum states, the squeeze laser requires multiple cavities, control schemes, optical components and electronic support. The setup, inspired by [21], is shown in Figure 4.1. Here, the main difference is the cavity design of the parametric down-conversion cavity, which is elaborated in Section 4.2. The entire optical setup is placed on a $80 \, \text{cm} \times 80 \, \text{cm}$ breadboard, which allows the transportation to other facilities in the future.

Laser preparation: A commercially available seed and amplifier fiber laser system from *NKT Photonics* produces up to $2 \, \text{W}$ of quasi-monochromatic $1550 \, \text{nm}$ light. It was possible to tune the wavelength of the light between $1550 \, \text{nm} \pm 200 \, \text{pm}$, which we refer to as the wavelength offset. The light was split with a fiber splitter from *Thorlabs* with a 50:50 ratio into two parts. Roughly $80 \, \text{mW}$ exits a fiber output coupler (top left in the figure), passes a $\lambda/4$- and a $\lambda/2$-waveplate and is transmitted through a Faraday isolator to prevent back reflections, which would otherwise cause instabilities in the seed laser. Next, an electro-optic modulator (EOM) imprints a phase modulation of $61 \, \text{MHz}$ on the light. This modulation is used to lock the length of different cavities via a Pound-Drever-Hall scheme, which is explained in detail in Section 4.2.5. A combination of a $\lambda/2$-waveplate and a polarizing beam splitter (PBS) regulates the power, which is either sent to the local oscillator path on the right or used for the generation of $775 \, \text{nm}$ light.

Second harmonic generation: In the latter case a second harmonic generation (SHG) cavity is set up to provide the pump field for the squeeze laser at $775 \, \text{nm}$, with two photodiodes placed in transmission of the cavity. PD_{1550} is used to monitor the $1550 \, \text{nm}$ light transmitted through the cavity, while PD_{SHG} is detecting the converted light at $775 \, \text{nm}$. Additionally, PD_{SHG} is providing a feedback signal for the length stabilization of the cavity.

Squeezed light generation: The produced pump field from the SHG is sent to the squeezed light generating cavity by using the process of parametric down-conversion (PDC). In the depicted setup in Figure 4.1, the cavity is set up in a *monolithic*
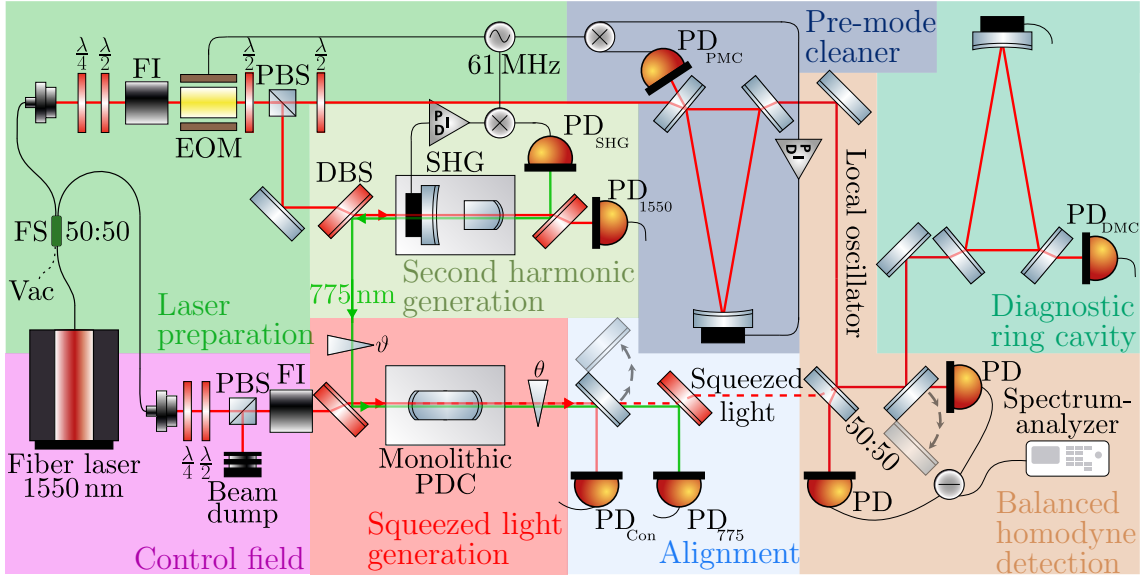
Figure 4.1 – **Schematic setup of a squeeze laser with a monolithic cavity design on a 80 cm×80 cm breadboard.** This setup for creating and detecting the squeezed states consists of multiple parts, highlighted in different colors. A 1550 nm fiber laser is connected to two fiber output coupler via a fiber splitter. In the top left section, the light passes different polarization optics and an electro-optic modulator (EOM). Most of the light is sent to the second harmonic generation (SHG) cavity, which creates the pump field at 775 nm for the parametric down-conversion process in the monolithic cavity design, simply referred to as PDC. Additionally, an auxiliary control field enters the PDC from the same side and is used for adjustment. Light, which is not sent to the SHG, is filtered in a triangular ring cavity, called the pre-mode cleaner (PMC), which provides the local oscillator (LO) field for the balanced homodyne detection. Here, the LO is overlapped with the squeezed light, detected on two photodiodes (PD) and evaluated on a spectrum analyzer. The phase between the LO and the squeezed states can be controlled with the phaseshifter ϑ and θ. In the top right a diagnostic ring cavity can be used to optimize the interference of the two fields. FI=Faraday isolator, DBS=dichroic beam splitter, PBS=polarizing beam splitter.

design. In Section 4.3.4 it will be changed to a *hemilithic* one. The differences between these two schemes are described in Section 4.2.1. Two phaseshifter are implemented to vary the phases of the pump field ϑ or the squeezed field θ in respect to the local oscillator, which allows the readout of arbitrary quadrature.

Control field and alignment: As the squeezed light has almost no amplitude, a bright auxiliary control field was sent onto the crystal from the highly reflective side, which requires high light power of the auxiliary field. The spatial mode of the control field in the PDC cavity is monitored by PD_{Con} in transmission. In our setup the control field fulfills two tasks: Firstly, it is used to find a temperature of the cavity where both the fundamental field in 1550 nm, monitored by PD_{Con}, and the pump field in 775 nm, detected on PD_{775}, are resonant (see Section 4.3.1). Secondly, the control field allows us to measure and optimize the spatial overlap of the squeezed field and the local oscillator at the 50:50-beam splitter with the help of the diagnostic ring cavity.

Balanced homodyne detection: The produced squeezed states are measured on a balanced homodyne detector, described in Section 3.3.1, where they are overlapped with the local oscillator (LO). The local oscillator path consists of a triangular cavity, the so called a pre-mode cleaner cavity (PMC), elaborated in Section 4.2.3. This cavity is used to optimize the spatial shape of the mode, which can be distorted by passing through either the EOM or any other polarization optic. Any impurities in the mode shape result in a reduced visibility and increase the optical loss, which directly limits the detectable squeezing values. The visibility, or the contrast, for equal input powers at the homodyne detector is given by

$$V = \frac{I_{\max} - I_{\min}}{I_{\max} + I_{\min}}, \tag{4.1}$$

where $I_{\max}$ and $I_{\min}$ describe the currents measured on one of the photodiodes while the phase between the two input fields is scanned. After exiting the PMC, the local oscillator is almost entirely in the TEM_{00}-mode and it is sent onto the 50:50-beam splitter.

Diagnostic ring cavity: To achieve high interference between the local oscillator and the squeezed states at the beam splitter, we use an auxiliary diagnostic ring cavity, which is further described in Section 4.2.4. By using this technique visibilities as high as $(99.0 \pm 0.3)\,\%$ were measured.

4.2 Cavities

The squeeze laser utilizes different cavities, each one with a different purpose: Generating squeezed states of light by parametric down-conversion, producing light for the pump field at 775 nm by second harmonic generation, optimizing the beam shape of the local oscillator with a pre-mode cleaner and enhancing the spatial overlap of multiple light fields on a diagnostic ring cavity.

4.2.1 Parametric down-conversion

The generation of squeezed states is performed by parametric down-conversion within cavity-enhanced optical parametric amplification. Here, the pump field at 775 nm is converted into to a squeezed vacuum field at 1550 nm, which is theoretically described in Section 3.1.

The squeeze lasers built throughout this thesis use two different designs for the PDC cavity: A monolithic design, used in Section 4.1, and a hemilitic one, depicted in Section 4.3.4 and 4.4. Figure 4.2 shows a simplified sketch of both cavities emphasising their differences. For a simplified overview, Table 4.1 summarizes the different specifications of the cavities.

The **hemilithic cavity** design (top) consists of a partially reflective incoupling mirror and a nonlinear crystal of 9.3 mm length made of periodically-poled KTP. The incoupling mirror is curved with a radius of curvature (ROC) of 25 mm and includes reflective coatings of 85 % for 1550 nm and 97.5 % for 775 nm. The front side of the crystal was anti-reflective (AR) coated for 1550 nm and 775 nm, the back side was curved with a ROC of 12 mm and highly reflective for both wavelengths. The air gap between the mirror and the crystal was 24 mm wide. The incoupling mirror is attached to a piezo-electric actuator, which is used to vary the length of the cavity. For the aligning process of the spatial mode of the incoming field to the cavity, a frequency generator applies a triangular voltage to this piezo-electric element. This scan of the cavity over a full free-spectral range (FSR) allows the monitoring of
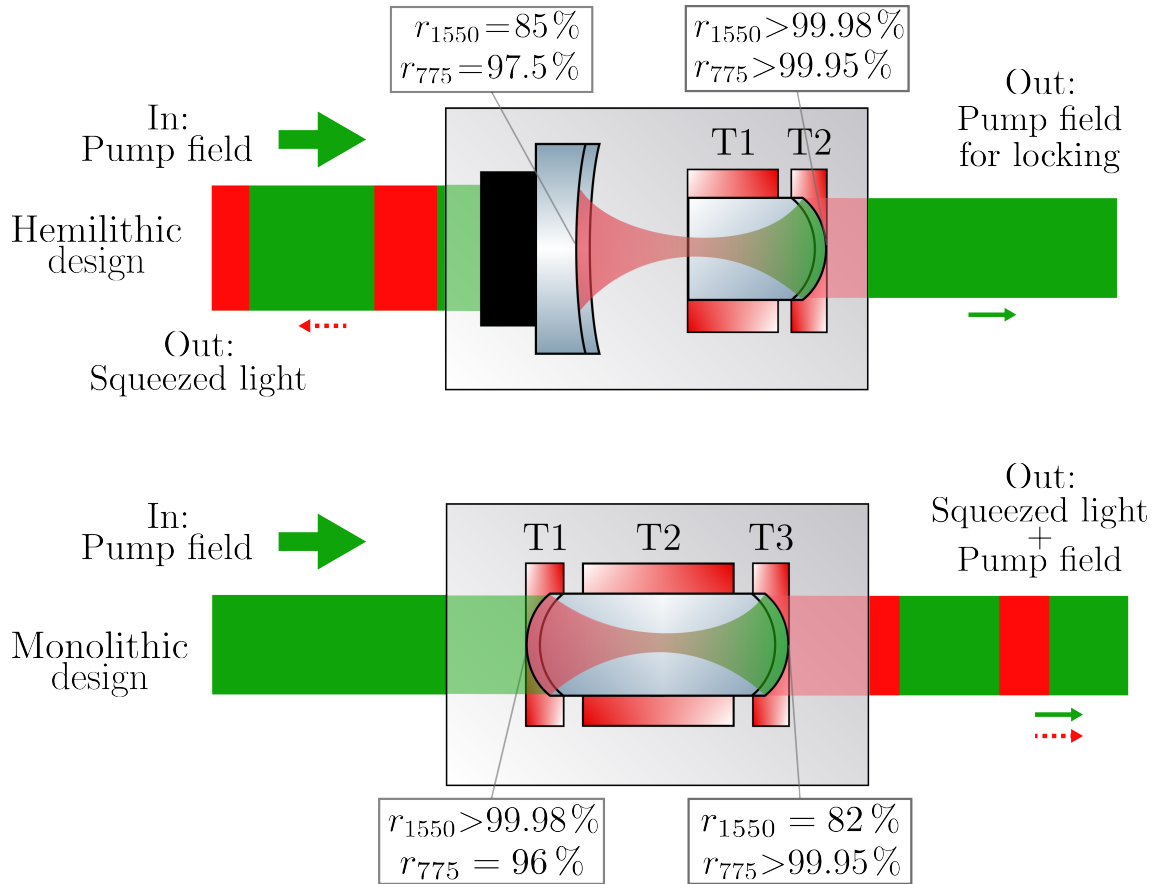
Figure 4.2 – **Comparison of the hemilithic and the monolithic cavity design.** In both designs, a bright pump field enters the cavity from the left, which is converted into a squeezed light field together with some small fraction of the pump field. The arrows reference the amplitude and the direction of the fields. **Top:** The hemilithic cavity design is made of a partially reflective incoupling mirror, a crystal and an air gap between them. The mirror is connected to a piezo-electric element (black), which is utilized to vary the length of the cavity. To fulfill the phase matching condition, the temperature can be adjusted with two separate peltier elements T1 and T2. This design was used for the second-harmonic generation process as well. **Bottom:** The monolithic design consists of one single crystal. The effective length of the cavity is varied with the temperature, which can be adjusted by three distinct peltier elements, or the wavelength offset. To fulfill the phase matching condition, the main temperature T2 is used. By changing the wavelength offset, a cavity length can be found were both the pump field and the fundamental field are resonant.

Parameter	Hemilithic design		Monolithic design	
Cavity length L	9.3 mm + 24 mm airgap		11.3 mm	
FSR	3.7 GHz		7.7 GHz	
	1550 nm	775 nm	1550 nm	775 nm
r_1	85 %	97.5 %	99.98 %	96 %
r_2	99.98 %	99.95 %	82 %	99.95 %
Finesse F	41	246	34	155
Bandwidth γ	89.6 MHz	15.2 MHz	225.9 MHz	49.6 MHz

Table 4.1 – **Comparison of hemilithic and the monolithic design.** The table summarizes the different specifications of the hemilithic and the monolithic design. r_1 and r_2 denote the power reflectivities of the front and back side of the cavities. For the optical cavity length, different refractive indices for KTP and air were considered. The FSR, the finesse and the bandwidth were calculated with the formula presented in Section 3.4.2.

the mode distribution. Additionally, with a Pound-Drever-Hall locking scheme, the length of the cavity is stabilized to its resonance condition throughout the measurements.

The two temperatures allow the fulfillment of the phase matching condition, which was introduced in Section 3.2. Here T1 and T2 characterize two thermo-electric modules (TEC), which are glued to a printed circuit board inspired by [21]. Next to these modules, two negative temperature coefficient (NTC) thermistor, which are elements, that posses a temperature dependent resistance, are used to measure the temperature. The areas heated up by T1 and T2 differ in size as shown in Figure 4.2. T1 is referred to as the phase matching temperature. Its effective size is larger and it dominates the temperature in the whole crystal. The heated area of T2 is smaller and used to improve the conversion process even further: The domain length of the periodically poled section in the crystal is well defined in the center. At the edges however, it is possible that the length of the outermost domain is smaller than the coherence length. Although small, this can cause a decrease in the conversion efficiency. Ideally, the only purpose of T2 is to change the optical length of the last domain to match the coherence length.

The **monolithic design** consists of only one single PPKTP crystal with a length of 11.6 mm one but with reflective coatings on both sides. In this scheme, the temperature is used to satisfy the phase matching condition. Similar to the hemilithic design, the main temperature contribution comes from the center temperature (here T2). T1 and T3 are used to balance out any inhomogeneity at the edges of the crystal. For the resonance condition the wavelength offset of the seed-laser was used, which is further analyzed in Section 4.3.1. In contrast to the hemilithic cavity, the length of the monolithic one was not stabilized in a feedback locking scheme. Adjusting the wavelength to a value, where the resonance condition was fulfilled, provided enough stability for our measurements. It is possible to implement a Pound-Drever-Hall lock for the length by using the temperature and for experiments, that require measurement times in the time frame of hours or days, a length stabilization scheme is recommended.

In this thesis, I set up different squeeze laser with both the monolithic and the hemilithic cavity design. The experimental realization and the individual features of both schemes will be discussed in Section 4.3.

4.2.2 Second harmonic generation

The second harmonic generation cavity is used to produce light at half the wavelength of the its pump field. In the squeeze lasers presented in this thesis, SHGs are used to convert light from 1550 nm to 775 nm. The hemilithic cavity design as well as the properties of the nonlinear crystal and the incoupling mirror are identical to the one in Figure 4.2. Two temperatures are used to create conversion and optimize its efficiency. Shown in Figure 4.1 the two photodiodes PD_{1550} and PD_{SHG} detect light at 1550 nm and at 775 nm in transmission of this cavity. The former one was used to calibrate and adjust the cavity to the incoming pump field, while the latter one provides an error signal for the cavity to stabilize the length via a Pound-Drever-Hall locking scheme (see Section 4.2.5).

4.2.3 Pre-mode cleaner

In this topology, two highly reflective mirrors with $r_{1550} = 99.8\,\%$ and one curved mirror with $r_{1550} \approx 1$ with a radius of curvature (ROC) of $500\,\text{mm}$ form a triangular ring cavity, which is $8.5\,\text{cm}$ long and $2.3\,\text{cm}$ wide. Attached to the endmirror is a piezo-electric actuator, which can change the effective length of the cavity similar to the length change in the hemilithic cavity design. The length of the cavity is operated in a way that only the fundamental TEM_{00} mode is transmitted. Throughout this thesis, pre-mode cleaner cavities are solely used to optimize the spatial shape of a light field and to produce the local oscillator.

The length of the cavity is stabilized via a Pound-Drever-Hall locking scheme (see Section 4.2.5), where the error signal is detected in reflection of the cavity. This means that the sideband modulation frequency of the EOM, in this case at $61\,\text{MHz}$, needs to be above the bandwidth of this cavity, which was $3.5\,\text{MHz}$.

4.2.4 Diagnostic mode cleaner

A diagnostic mode cleaner (DMC) is an auxiliary cavity used to minimize the spatial mismatch of two or more optical fields [42, 43]. In this thesis, it is solely used to maximize the spatial overlap of multiple light fields at the beam splitter of the balanced homodyne detector. It consists of a triangular cavity, which is built identically to the PMC in Section 4.2.3.

The concept of the DMC is the following: Light is sent onto a cavity, where the length is periodically scanned. In transmission, a photodiode is detecting the power of different spatial modes at different cavity lengths, which I refer to as *mode picture*. The transmitted light of the cavity depends on the position, angle and size of the incoming beam. For all of our cavities, we align the incoming beam in a way that only the TEM_{00} mode is transmitted. This process is called mode-matching and it is used for the alignment of every cavity presented in this section.

Mode-matching can additionally be used to improve the visibility at the beam split-

ter of the homodyne detector. Here, the cavity serves as a reference. When the interfering light fields are sent onto this cavity and their mode picture in transmission (or reflection) of the cavity is identical, the spatial properties of the incoming fields are identical as well.

As the squeezed states itself contain almost no optical power, a bright control field was sent into the crystal from the backside representing the squeezed light field. Both the control field and the local oscillator were matched on the DMC. With this the contrast of at the beam splitter was measured to be above $(99.0 \pm 0.3)\,\%$.

4.2.5 Pound-Drever-Hall locking scheme

The Pound-Drever-Hall (PDH) locking scheme, introduced in [44], is a technique to either stabilize the frequency of a laser to a reference cavity or, as it is used in this thesis, to stabilize the length of a cavity to the laser frequency. This length stabilization is required to keep the cavity on its resonance. The PDH locking scheme is utilized for all hemilithic cavities used in this thesis as well as for the pre-mode cleaner.

For the PDH-locking scheme used in this thesis, light, which is then sent onto a cavity, is phase modulated by passing through an electro-optic modulator at $61\,\mathrm{MHz}$. Depending on the relation between the bandwidth of the cavity and the modulation frequency, either the reflected or the transmitted light is detected on a photodiode, which transfer function is resonant at the modulation frequency. This signal is mixed with an electrical local oscillator at the same frequency. The mixed signal contains the sum and the difference of both electrical signals. It is low-pass filtered and provides the error signal for the locking scheme. The error signal is fed into a proportional–integral–derivative (PID) control system, which regulates and stabilizes the length of the cavity.

The original PDH-locking system used to detect the modulation in reflection of the cavity. In most of our cavities, we detect it in transmission as it reduces the amount of necessary optics. This requires the sideband frequency to be smaller than the

bandwidth of the cavity.

A low-noise error signal is vital for the strength of the locking scheme. For this purpose Hennig Vahlbruch and Sebastian Steinlechner, previous members of the group at the Albert-Einstein-Institut, designed a resonant photodiode circuit design, where the detection of the light and the creation of the error signal is performed on a single printed-circuit board. Additionally, they built a servo circuit, which is required to control the locking scheme. This servo design was optimized by Jan Südbeck, Oke Huhs and myself. This optimization, described in [45], contains an automatic length stabilization system, which allows the near continuous operation of the cavities even after external disturbances disrupt the locking scheme.

4.3 Squeezed light generation with a monolithic cavity design

In [29], the performance of a hemilithic cavity design was compared to a monolithic one at the laser wavelength of 1064 nm. In terms of intra-cavity losses, the monolithic cavity is superior. This is due to the amount of passings of anti-reflective (AR) coatings per round trip in the cavity itself. In the hemilithic case light passes through AR coatings two times, while there are no AR coatings in the monolithic design.

On the other hand there are multiple downsides in terms of experimental work with monolithic cavity designs: Controlling the cavity length is difficult and usually done by tuning the temperature. Due to the absorption of the pump field in the crystal, thermal disturbances can cause instabilities while operating the cavity. At 1064 nm these instabilities are enhanced due to the strong heating effects of the pump field at 532 nm. For 1550 nm with the pump field wavelength of 775 nm, the absorption and the created heating of the cavity are reduced. Therefore one goal of this thesis was the comparison of the two cavity designs at 1550 nm. I first built the setup presented in Figure 4.1 and characterized it in terms of detectable squeezing and

anti-squeezing values as well as overall approachability.

4.3.1 Double resonance and phase matching in the monolithic cavity

As mentioned in Section 4.2.1, for achieving high conversion with optical parametric amplification, the cavity has to fulfill two conditions: First, the optical length of the cavity has to stabilized on resonance of the fundamental wavelength to produce continuous squeezed light fields. For all measurements our cavities are operated on double resonance, which describes a specific optical cavity length where both the pump field and the squeezed light field at the fundamental wavelength are resonant. Although not necessary, double resonance of the cavity leads to smaller external pump powers and is implemented in all cavities used in this thesis. Second, the phase matching condition has to be fulfilled to achieve high conversion throughout the whole crystal (see Section 3.2). In hemilithic cavities the length of the cavity is controlled by a piezo-electric element, which is connected to the incoupling mirror. The temperature of the crystal is then used to achieve the phase matching condition.

In monolithic cavities this is different as the length of the crystal can not be adjusted with a piezo-electric element. To fulfill the phase matching the temperature is used, which changes the refractive index of the cavity leading to a change in the optical path length. To achieve double resonance, the wavelength offset of the seed-laser was tuned. The effects of different wavelength offsets on the double resonance in the cavity is shown in Figure 4.3, where I vary the wavelength of the seed laser from $-173\,\mathrm{pm}$ to $-192\,\mathrm{pm}$, which results in the effective wavelength tuning between $1549.808\,\mathrm{nm}$ and $1549.827\,\mathrm{nm}$. Here, the fundamental light, represented by the control field, in red and the pump light in green are shown while periodically changing the temperature T3 of the cavity with a frequency generator at $200\,\mathrm{mHz}$. The control field was detected on $\mathrm{PD_{Con}}$ and the pump field on $\mathrm{PD_{775}}$. When changing the wavelength offset one can tune the resonances relative to each other. For this measurement the squeezed light mode was replaced by the control field, which coupled into the cavity from the front side. The phase between the two fields was not
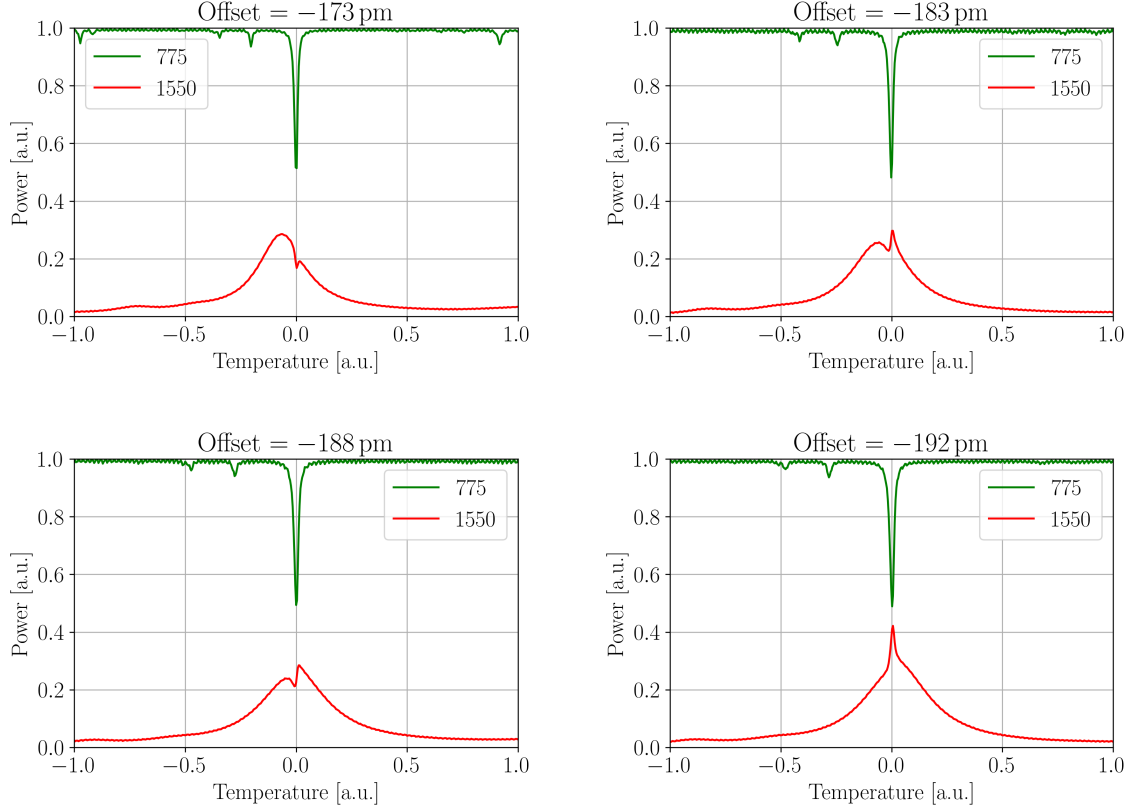
Figure 4.3 – **Resonances of the fundamental field and the pump field in the monolithic PDC design for different wavelength offsets of the seed laser.** The four pictures show the normalized power of the pump field (green), detected on PD_{775}, and of the control field (red), measured on PD_{Con}, for different wavelength offsets of the seed laser while periodically changing the temperature T3. The offset is specified relative to the center wavelength at $1550\,\mathrm{nm}$ and it is used to tune the overlap of the two resonances so that the cavity is resonant for both wavelengths at one specific temperature. The dips or peaks in the red traces arise due to parametric amplification or deamplification. Because the phase between the two fields is not controlled, these effects result in arbitrary shapes of the fundamental light. The best overlap was achieved for $-188\,\mathrm{pm}$, which leads to an effective wavelength of $1549.812\,\mathrm{nm}$. All future measurements with the monolithic design were performed at this wavelength.

controlled, which leads to random parametric amplification (second and fourth picture of Figure 4.3) or deamplification (first and third picture). The greatest overlap was achieved at the wavelength of 1549.812 nm in the third picture. All following measurements of the monolithic cavity design were performed at this wavelength.

Figure 4.3 depicts the resonance of both wavelengths in range of 19 pm. The resonance condition can additionally be fulfilled when the offset is shifted over a wider range. In Figure 4.3 this would be illustrated in an overlapping of the peak at the fundamental wavelength with a different peak of the pump field, which is not shown in the figure. To that end the offset had to be tuned for 80 pm. As the seed laser was only able to shift the wavelength offset between 1549.8 nm to 1550.2 nm there were in total 5 wavelength offsets, at which the squeeze laser could be operated. For these 5 points I measured the gain of the cavity, which describes the increase of the fundamental light when it is amplified by the pump field. The highest gain was found for the wavelength of 1549.812 nm.

4.3.2 Experimental detection of squeezed states with balanced homodyne readout

To evaluate the performance of the squeeze laser in the monolithic cavity design, a zero span measurement with a resolution bandwidth of 300 kHz and a video bandwidth of 300 Hz was performed with a spectrum analyzer, shown in Figure 4.4, with the measurement specifications listed in Table 4.2.

Table 4.2 – Measurement specifications for the zero span measurement performed in Figure 4.4

Parameter	Value
Detection frequency	3.3 MHz
Local oscillator power	(10.0 ± 0.5) mW
Pump light power	(65.00 ± 3.25) mW
Anti-squeezing	(18.97 ± 0.15) dB
Squeezing	(10.70 ± 0.18) dB
Optical loss	(6.96 ± 0.28) %

To detect the shot noise the input of the squeezed light was blocked and only the

local oscillator was sent on the beam splitter. The dark noise, which was detected when both the LO and the squeezed path were blocked, measured at the detection frequency was 23 dB below the shot noise and was not subtracted from the other traces. After detecting both the shot noise and the dark noise, the squeezed states were lead into onto the beam splitter.
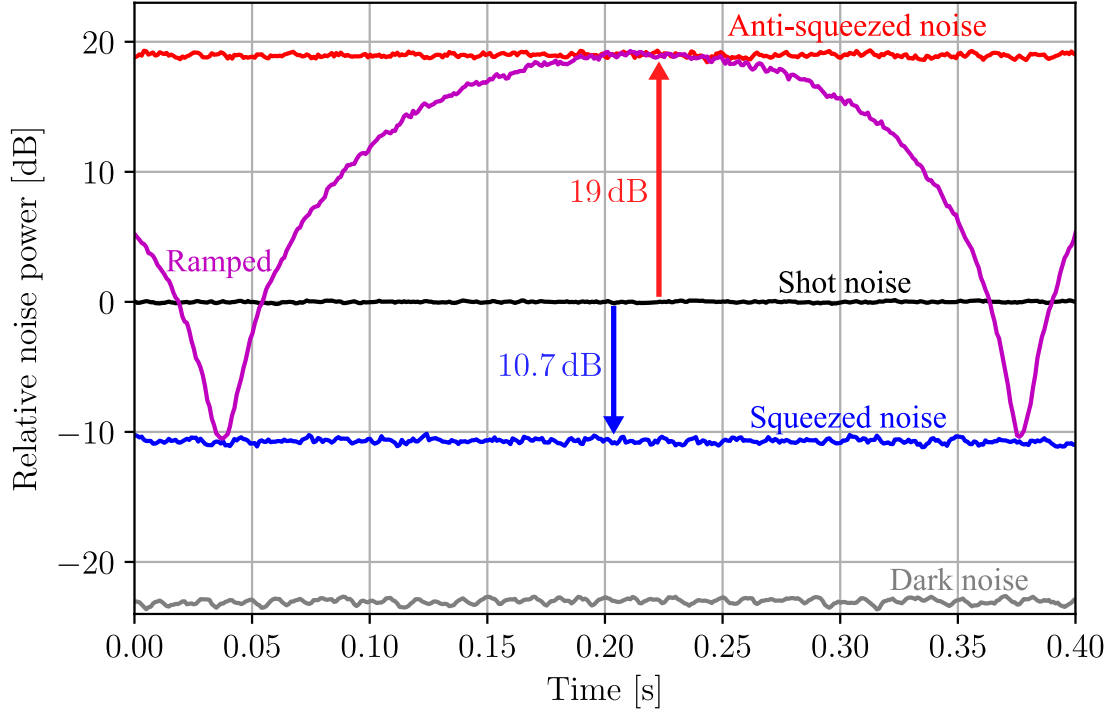
Figure 4.4 – **Zero span measurement at 3.3 MHz of the squeezed and anti-squeezed noise normalized to the shot noise of the monolithic cavity design.** The measurement shows 10.7 dB of squeezing (blue) for 19 dB of anti-squeezing (red), which is normalized to the shot noise (black). In purple the phase θ was periodically changed. The optical loss results in 7 %. Other measurement specifications are shown in Table 4.2. The dark noise in this measurement was below 23 dB below the shot noise and was not subtracted from the data. The resolution bandwidth was 300 kHz and the video bandwidth 300 Hz.

The setup produced a shot noise reduction of 10.7 dB with 19 dB of anti-squeezing, which resulted in 7 % of loss in the setup. The phase between the local oscillator and the squeezed light, which determines the detected quadrature on the balanced homodyne detector, was not stabilized by any feedback loop. These feedback loops

are required when the phase has to be stabilized for longer periods of time. For high RBWs the measurement times remain small and does not require an active stabilization. Instead varying the input voltage of the phaseshifter when taking the measurement determines the phase between the local oscillator and the squeezed states and allows the switch between detection the squeezed or anti-squeezed trace. The purple trace shows a periodically changing readout of the signal by applying a sinusoidal voltage to this phaseshifter.

The main contributions of the optical loss are the spatial overlap between the modes of the local oscillator and the squeezed field. We noticed that the output mode of the squeeze cavity is distorted slightly when the pump field is near the threshold of the cavity. This distortion reduces the visibility and therefore the reachable squeezing levels. The reason for this deformation is not clear. Due to the high intensity, it might be caused by thermal lensing or other thermal effects inside the cavity. Additionally, the quantum efficiency of the photodiodes and intra-cavity losses contribute to the overall loss.

4.3.3 Performance of the squeeze laser over 21 days

In future experiments, the squeeze lasers constructed in this thesis are planed to be implemented in various experiments, which are assumed to run for multiple months or even years. To make sure that high squeezing values can be ensured over longer periods, we characterized the changes in squeezing and anti-squeezing level occurring during 21 days in which the squeezer was operated. Over night between the measurement days, the squeeze laser was shut down. Once per day the squeezing and anti-squeezing values were measured by performing a zero span measurement at 3.3 MHz similar to the one presented in Figure 4.4.

During the 21 days, I tried to minimize adjustments performed on the squeeze laser. These adjustments included corrections of the spatial overlap of the squeezed and the local oscillator field due to temperature drifts of mechanical components as well as adaptations of the optimal conversion temperature of the PDC cavity.
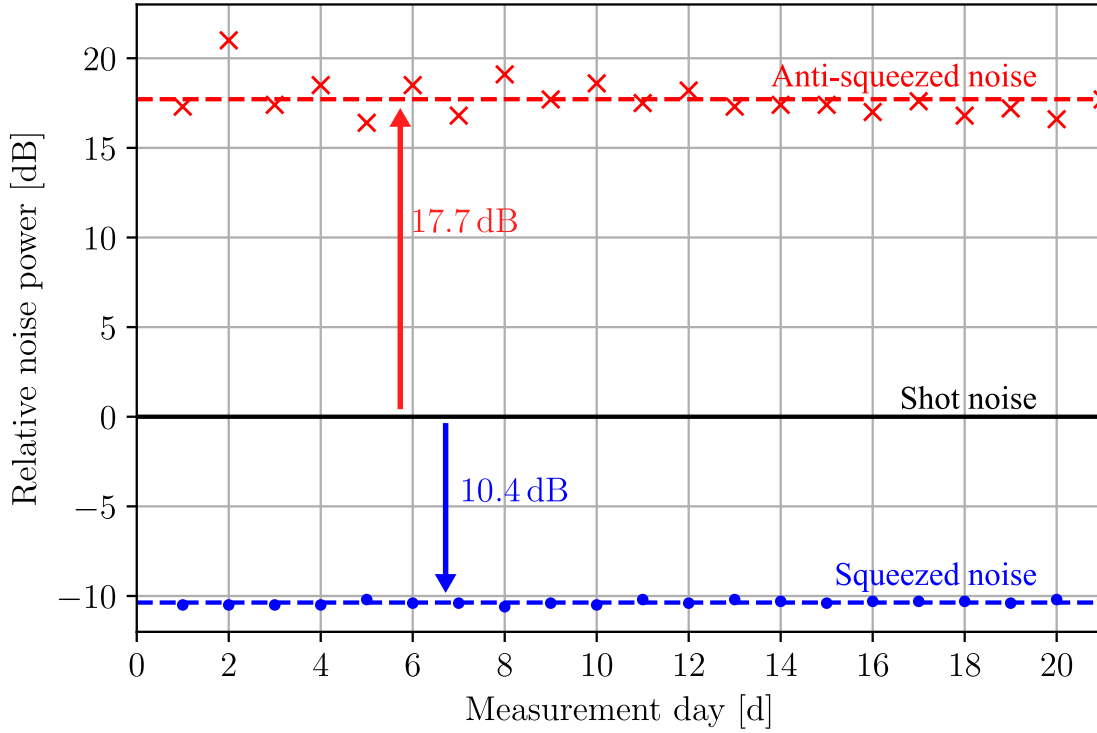
Figure 4.5 – **Performance of the squeeze laser over a period 21 days.** Each dot and each cross represents the squeezing and anti-squeezing values of a zero span measurement with similar properties to the one in Figure 4.4. The data is normalized to the shot noise and the dark noise was subtracted from the traces. The dashed lines depict the mean values with (10.37 ± 0.28) dB and (17.73 ± 1.02) dB of the squeezed and anti-squeezed measurements. Between these measurements the only adjustments performed in the setup were improving the visibility at the beam splitter and optimizing the temperature of the cavity.

In Figure 4.5 the measured squeezing and anti-squeezing values for each day normalized to the shot noise are shown. The mean values are depicted as dashed lines. The measurement resulted in (10.37 ± 0.28) dB of squeezing and (17.73 ± 1.02) dB of anti-squeezing, where the errors are the mean squared deviations of the data. The resulting loss varies between 7 % and 8 %. I show that constant high squeezing values are producible repetitively with small effort. The performed alignments each day were completed is less than 30 min.

The pump power of the squeezer and the power of the local oscillator were 65 mW

and 10 mW respectively and remained unchanged between the measurements. From day 8 until the end of the series, problems in the air cooling system of the institute and in the air damping of the optical table were reported, which lead to increased time spent on the correction of any occurring misalignment.

4.3.4 Squeezing performance of the hemilithic cavity design

To classify the performance of the monolithic design, the monolithic cavity from Section 4.3 was changed to a hemilithic one, which was introduced in Section 4.2.1. The locking scheme of the PDC cavity is identical to the one used in the SHG cavity, where the length stabilization is performed with a piezo-electric crystal connected to the incoupling mirror. The length stabilization is done with a Pound-Drever-Hall lock with the error signal produced by PD_{775}. Instead of placing a second EOM in the 775 nm pump field to create the necessary sidebands, we set the frequency of the phase modulation of the first EOM to a frequency inside the bandwith of the SHG cavity. The sidebands are up-converted and preserved in the pump field and can be used to stabilize the PDC cavity. There were no major changes made to the rest of the setup other that replacing optical components to fulfill the needs of the newly calculated mode-matchings.

Table 4.3 – Measurement specifications for the zero span measurement performed in Figure 4.6

Parameter	Value
Detection frequency	5 MHz
Local oscillator power	(10.0 ± 0.5) mW
Pump light power	(25.00 ± 1.25) mW
Anti-squeezing	(17.87 ± 0.22) dB
Squeezing	(10.53 ± 0.31) dB
Optical loss	(7.17 ± 0.52) %

A zero span measurement is shown in Figure 4.6 with the specifications of the measurement listed in Table 4.3.

The optical loss of 7.2 % is comparable to the loss of the monolithic cavity of 7 % presented in Figure 4.4. The squeezing value can still be improved by increasing

the pump power, enhancing the visibility at the beam splitter and optimizing the temperatures of the PDC. In the future, this squeeze laser will be used to enhance the sensitivity of the Hamburg prototype of the HF Einstein Telescope, which is currently set up by Justin Hohmann in his PhD thesis. It was transported between two laboratories and reinstalled next to the experiment. As the prototype encountered various different challenges, the implementation of squeezed light in this experiment will be delayed, which means that there was no use to improve the detectable squeezing values at the moment.
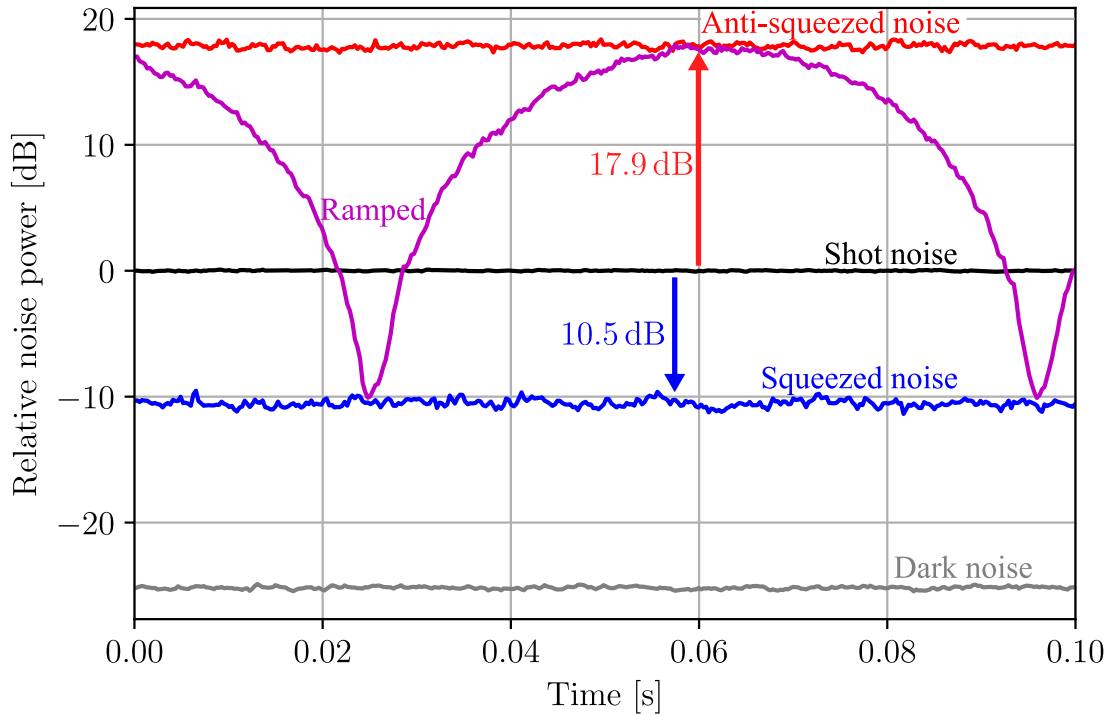
Figure 4.6 – **Zero span measurement at 5 MHz after exchanging the monolithic PDC design with a hemilithic one.** Squeezing and anti-squeezing values are compared to the shot noise. The measurement shows 10.5 dB of squeezing for 17.9 dB of anti-squeezing, which corresponds to 7.2 % of optical loss. The RBW was 300 Hz and the VBW was 300 Hz. Other measurement specifications are presented in Table 4.3. The values are in good agreement with the results of the monolithic cavity design, which was shown in Figure 4.4.

Although the optical loss in the hemilithic setup has slightly increased compared to the monolithic design, it offers several advantages, which will be discussed in Section

4.3.5.

4.3.5 Limitations of the monolithic design and comparison

In [29], the switch from a hemilithic to a monolithic PDC at a wavelength of 1064 nm proved to be successful as it was able to produce 12.7 dB of squeezing with 4.5 % of optical loss. The limitation to achieve even higher values of squeezing for this wavelength were thermal effects of the pump field at 532 nm. These thermal effects were proposed to be lower at the wavelength of 775 nm. However, in this thesis there was no visible improvement of a monolithic setup compared to the hemilithic one described in [21].

The highest squeezing value achieved in the monolithic design was 10.7 dB with a corresponding optical loss of 7 %. The main loss contribution is the spatial overlap of the interfering modes, which was restricted by the slight distortion of the output mode of the squeezer when the cavity was driven close to its threshold. We are not entirely sure where this problem comes from, but suspect thermal effects due to absorption in the crystal. Getting rid of this problem is challenging as one need the high pump power to get sufficient anti-squeezing values. We tried first pumping the squeezer slightly below threshold and directly adjusting the spatial overlap of the fields by optimizing the squeezing value on the spectrum analyzer, with which we achieved a small increase in the squeezing values of about 0.4 dB.

Additionally the monolithic design showed multiple flaws compared to a hemlitihic PDC:

Alignment: The alignment of the pump field to the PDC cavity requires a scan of the optical length of the crystal. In hemilithic cavities this is done by oscillating the mirror, that is connected to the piezo-electric crystal. This oscillation is performed at a frequency between 10 Hz–100 Hz, leading to a fast response of the mode picture. In the monolithic case the change of the optical length is performed by varying the temperature, which is limited to mHz-frequencies due to the slow response of the TEC. This means that aligning the monolithic cavity is slower and leads to worse

results compared to the hemilithic design. Scanning the wavelength for aligning the pump field was not possible as the SHG cavity was not able to stay on resonance during the scan.

Stability: The stability of the monolithic design highly depends on the used optical pump power. For high pump powers we noticed instabilities, which we attributed to an increase of the temperature inside the crystal due to absorption. As the temperature was the main parameter to adjust the length of the cavity to its resonance, it was challenging to stabilize the cavity for increasing pump powers.

Requirements on the seed-laser: Due to the design of the monolithic cavity, the wavelength offset of the seed laser can not be set to any arbitrary wavelength but rather defines a specific wavelength at which the setup can be operated. When the squeeze laser is implemented in another experiment in the future, there is therefore a strong confinement on the wavelength. Next, the pump power of 65 mW was higher for the monolithic case compared to the hemilithic one, which was observed at 1064 nm as well. One reason here are the lower reflectivities of the crystal. Additionally, the alignment of the pump field to the cavity was worse, which directly decreases the effective light power in the cavity.

After considering both cavity designs, we concluded that the hemilithic system is more stable, easier to set up and to operate. Particularly the alignment of the pump field on the PDC is much faster in the hemilithic design. In this work, the primary focus lies on the usage of squeezers in different experiments, their compatibility, implementation and performance when used in combination with other interferometric setups. Considering that, the monolithic design provides only marginal advantages in terms of squeezing performance and no substantial benefits in overall usefulness compared to the hemilithic design. Therefore we have decided to use hemilithic cavities exclusively moving forward.

4.4 The squeeze laser on a 60 cm×40 cm breadboard

After working with the squeeze laser presented in the previous sections, it was apparent that the size of the whole setup can be reduced even further without compromising strongly in terms of squeezing values. This section describes the characterization of a squeeze laser, that was set up on a 60 cm×40 cm breadboard. The setup was transported to the Clausthal University of Technology in Chapter 5.

4.4.1 Setup

The squeeze laser was designed to be smaller and lighter than the one in Section 4.3 to facilitate the transportation process for future experiments. In Figure 4.7, the setup shows the outline of the breadboard as the black line while everything outside of the breadboard is dyed in grey. Almost all sections from Figure 4.1 underwent some changes to decrease the size and reduce the weight to make shipping easier. The fiber laser, the fiber splitter and a newly implemented broadband fiber EOM by *Jenoptik*, which replaced the previously used free space crystal, were placed outside of the breadboard and can be transported separately from the squeeze laser. The PMC in the local oscillator path was removed, because the spatial shape of the laser beam was close to the TEM_{00} mode already. Additionally, it is now possible to use some light power of the local oscillator for experiments outside of the squeeze laser. This bright light field in the top right was, for example, used in Chapter 5 to provide the local oscillator field for the external homodyne detection. The squeezed states were produced in a hemilithic cavity due to the problems of the monolithic design described in Section 4.3.5. This cavity was identical to the one used in Section 4.3.4. For the length stabilization of the cavity and the generation of the error signal for the PHD lock, the converted sidebands of the second harmonic cavity were used. With a flipping mirror, it was possible to either measure the squeezed light on the on-board homodyne detector or guide them out of the breadboard. To save space, the diagnostic mode cavity was placed outside of the breadboard as it is only required for the initial alignment of the control field (acting as the squeezed field) and the
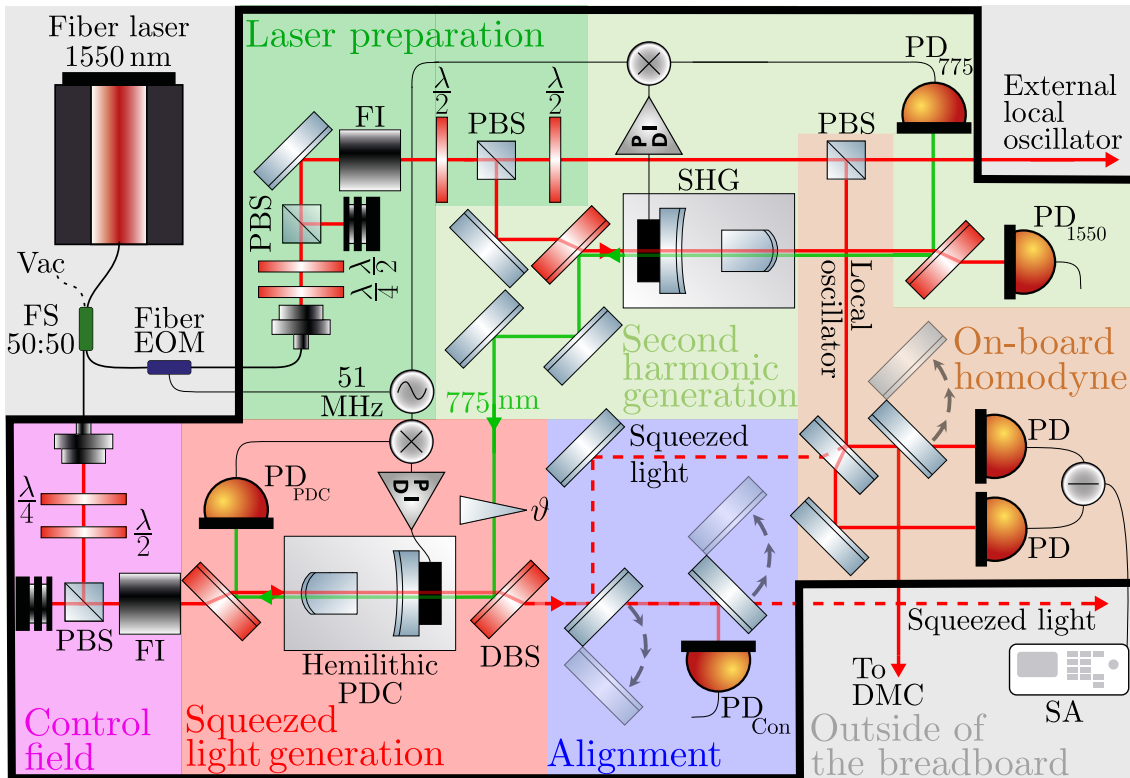
Figure 4.7 – **Schematic setup of the hemilithic squeeze laser on a 60 cm×40 cm breadboard.** The black outline represents the boundaries of the breadboard. The squeeze laser consists of different sections, highlighted in different colours. The main differences to the squeeze laser in Figure 4.1 are the decrease in size, the change to a hemilithic PDC design, the usage of a fiber EOM and the relocation of the DMC outside of the breadboard. The squeezed light is outcoupled at the bottom right corner and guided to future experiments. FI=Faraday isolator, PBS=polarizing beam splitter, DBS=dichroic beam splitter, FS=faser splitter, SA=spectrum analyzer, PD=photodiode, SHG=second harmonic generation, PDC=parametric down-conversion, DMC=diagnostic mode cleaner.

local oscillator. Once the size of the two beams is identical, small misalignment in position and angle between the two fields can be adjusted by directly optimizing the squeezed values or by monitoring the visibility.

4.4.2 Squeezed light detection at 5 MHz and 40 MHz

Two zero span measurements at 5 MHz and at 40 MHz were conducted to determine the squeezing performance before the transportation to the Clausthal University of Technology. The results of the former is presented in Table 4.4 and in Figure 4.8.

Parameter	Value	
Detection frequency	5 MHz	40 MHz
Local oscillator power	$(20 \pm 1)\,\text{mW}$	$(20 \pm 1)\,\text{mW}$
Pump light power	$(25.00 \pm 1.25)\,\text{mW}$	$(25.00 \pm 1.25)\,\text{mW}$
Anti-squeezing	$(20.47 \pm 0.13)\,\text{dB}$	$(8.25 \pm 0.12)\,\text{dB}$
Squeezing	$(10.06 \pm 0.14)\,\text{dB}$	$(6.08 \pm 0.13)\,\text{dB}$
Optical loss	$(7.87 \pm 0.26)\,\%$	$(10.00 \pm 0.39)\,\%$

Table 4.4 – Measurement specifications for the zero span measurement performed in Figure 4.8 at 5 MHz and in Figure 4.9 at 40 MHz.

The measurement show smaller squeezing values and higher optical loss than the measurements performed with the squeeze laser in Section 4.3 and 4.3.4. This is to be expected and is lead back to a decrease in the visibility at the beam splitter. This decrease is caused by reduction in size of the setup, which made the alignment of the squeezed and the local oscillator field more difficult. Additionally, a new design for the homodyne detector was introduced. This design was smaller than the previous one used in Section 4.3 and had a higher bandwidth, but therefore resulted in a higher dark noise at lower frequencies (see Section 3.4.1).

The second measurement at 40 MHz, presented in Table 4.4 and Figure 4.9, illustrates the limiting effect of the frequency bandwidth of the PDC cavity (see Section 3.4.2). 40 MHz is the frequency at which the heterodyne readout is performed at in Chapter 5. As expected both squeezing and anti-squeezing values are reduced compared to the measurement at 5 MHz. Additionally, the optical loss is increased, which is surprising as most noise sources have either equal contributions at 5 MHz, such as the frequency-independent shot noise, or in case of phase noise, are even reduced. Contributions to the optical loss, such as mode-mismatch, absorption or detection efficiency remained the same as well.

Figure 4.8 – **Zero span measurement at 5 MHz.** Squeezing and anti-squeezing values are compared to the shot noise. The measurement shows 10.1 dB of squeezing for 20.5 dB of antisqueezing, which corresponds to 7.9 % of optical loss. The specifications are presented in Table 4.4. The values are not dark noise corrected. The RBW for the measurement was 300 kHz and the VBW was 100 Hz.

We try to explain this the following way: As mentioned above, the sidebands, which are imprinted on the pump light field at 51 MHz, are inside the linewidth of the PDC cavity at 89.6 MHz. This means that they are affected by the conversion process and propagate together with the squeezed field. We investigated this effect by changing the electrical power sent to the fiber EOM, while monitoring the related squeezed values. For high electrical signals, the respective squeezing value was reduced. On the other hand, reducing the electrical power on the EOM decreases the error signal of the cavities, which was needed for the Pound-Drever-Hall locking scheme. Small error signals lead to instabilities in the length lock of the system and are one of the main causes for phase noise (see Section 3.4.1). Therefore, for the electrical power on the EOM, one needs to consider both of these effects.
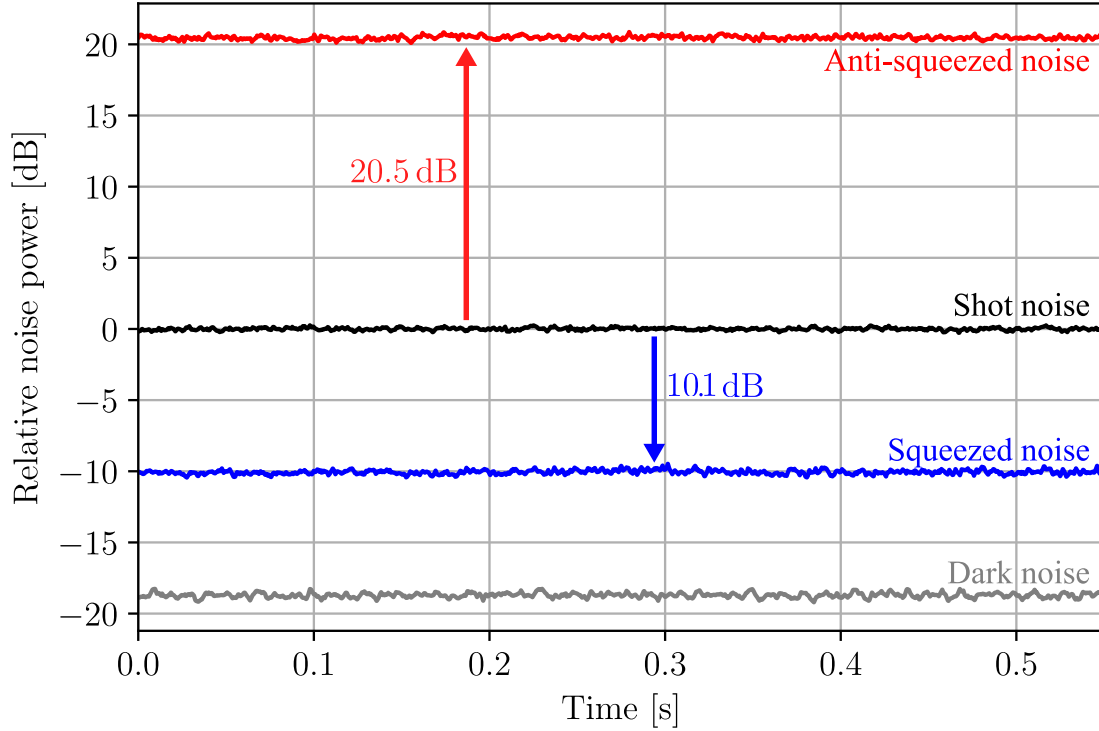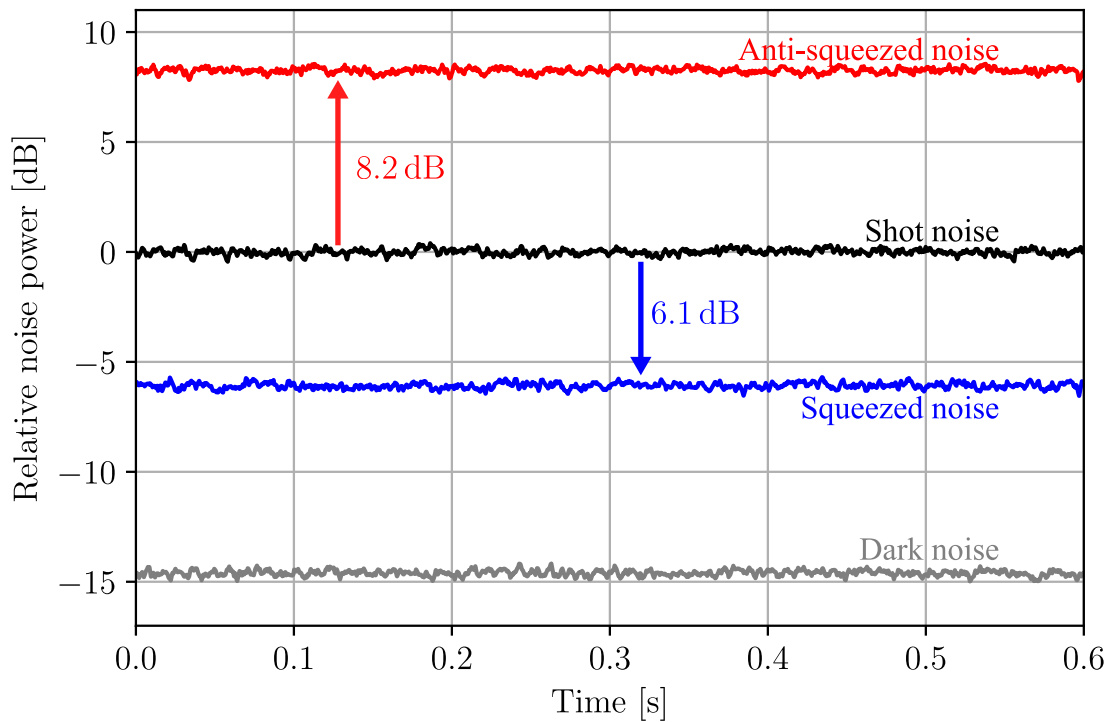
Figure 4.9 – **Zero span measurement at 40 MHz.** Squeezing and anti-squeezing values are compared to the shot noise. The measurement shows 6.1 dB of squeezing for 8.2 dB of antisqueezing, which corresponds to 10.1 % of optical loss. The specifications are presented in Table 4.4. The RBW for the measurement was 300 kHz and the VBW was 100 Hz. The frequency at which this measurement was performed was determined by the beat frequency of the heterodyne detection scheme in Chapter 5.

One way to get rid of this problem would be to imprint these sidebands on the local oscillators as well. When the optical path lengths and the amplitude of the sidebands are equal, the rotating phase modulations would cancel out. In our setup, this is not possible as it would require a second EOM which would be placed behind the PMC. This, however, leads to distortion of the spatial mode of the light.

A better solution requires a change in the frequency of the sidebands. By choosing a sideband frequency larger than the cavity bandwidth, the error signal for the length stabilization would be generated with the light reflected from the cavity and the sidebands would enter the cavity.

	Ge. 1	Ge. 2	Ge. 3	Ha.	Sc.	Ba.
Wavelength [nm]	1550	1550	1550	1550	1550	1064
Size [cm]	80×80	80×80	60×40	80×80	80×80	Not portable
SHG [type]	Hemi	Hemi	Hemi	Mono	Hemi	Hemi
PDC [type]	Mono	Hemi	Hemi	Mono	Hemi	Mono
Squeezing [dB]	10.7	10.5	10.1	10.4	13.1	12.7
Loss [%]	7	7.2	7.9	7	4.5	4.5

Table 4.5 – **Comparison of the size, schematic and performance of different squeeze lasers.** To quantify the effectiveness of the performed changes in this thesis, I compare the squeeze lasers, which I built (first three columns), with the ones from M. Hagemann, A. Schönbeck [21] and S. Steinlechner and J. Bauchrowitz [29]. All setups can provide more than 10 dB of squeezing in each case with rather small optical loss values. I was, however, not able to replicate the high squeezing values reported in [21] or [29].

4.5 Comparison of the performance of the squeeze lasers

One of the main goals of this thesis was the construction of portable squeeze lasers without compromising in their achievable squeezing level. Therefore, I compare the setups from this section with previous experiments in terms of size, produced squeezing and optical loss in Table 4.5. The first three squeeze lasers are characterized in this thesis, 'Hagemann' was setup by Malte Hagemann in his PhD-thesis, 'Schönbeck' was characterized in [21] by Axel Schönbeck, 'Bauchrowitz' in [29] by Sebastian Steinlechner and Jöran Bauchrowitz. The squeezer differ in size, operational wavelength and cavity design of the SHG and the PDC.

Although all squeeze lasers are able to produce more than 10 dB of squeezing, I was not able to reach the high values of [21] or [29]. Still, the optical loss in the setups is below 8 % and allows the implementation of the setups in different experiments. The squeeze lasers in this thesis were optimized for transportation and implementation in external experiments. A lot of work was funneled into enhancing the stability of the different locking schemes and into preparing the transport of the system rather than decreasing the optical loss further.

4.6 Outlook

4.6.1 Improvements of the current design

Size

The setup depicted in Figure 4.7 showcased the squeeze laser on a breadboard with a footprint of $60\,\mathrm{cm} \times 40\,\mathrm{cm}$. However, further reducing the size is possible by relocating non-essential components. First, the balanced homodyne detector, primarily used for initial squeezing verification, can be positioned outside on a separately portable breadboard. Another space-saving measure involves the usage of fiber optics. In Section 4.4, the previously homebuilt electro-optic modulator was replaced by a fiber EOM. For future squeeze lasers, the Faraday isolators can be exchanged by a fiber replacement as well. In contrast to free space components, the implementation of fiber optics is very straight forward and does not involve any adjustment of the laser beam. The size of the squeeze laser is mainly limited by the optical components. Fiber optics can be stored separately, for example by connecting them to the inside of the housing and therefore lead to smaller footprints of the optical setup.

In another future prospect, the hemilithic second harmonic generation cavity can be replaced by a single-pass design. In this configuration, the pump field propagates through the crystal only once, yielding faster adjustment, reduced costs without the need for an additional mirror compared to the hemilithic case, and eliminating the necessity for the length stabilization. On the other hand, the single-pass SHG achieves a much smaller conversion efficiency compared to the cavity design. As the squeeze laser built in this thesis were operated at pump powers of $25\,\mathrm{mW}$ and $65\,\mathrm{mW}$, the SHG therefore needs to be pumped at high optical powers. Here, increasing the reflectivities of the PDC cavity for the pump light at $775\,\mathrm{nm}$ can decrease the pump threshold.

Locking schemes

The use of locking schemes for the readout quadrature is another aspect for future squeeze lasers. In the measurements conducted in this chapter as well as in Chapter 5, the squeezed and anti-squeezed quadratures were not stabilized by a feedback loop. A coherent control locking scheme, introduced in [46], can be integrated into existing squeeze lasers. This design involves additional components such as a frequency-shifted light field (generated by an acousto-optical modulator), a beam splitter, and new integrated circuits in the photodetectors and in the homodyne detector.

4.6.2 Squeezed light generation via waveguides

The squeeze lasers in this thesis operate by utilizing parametric down-conversion in cavity-enhanced optical parametric amplification, which is to this day the method, that generates the highest squeezing values. Waveguides offer a different approach to the generation of squeezed light.

Optical waveguides are used to guide electromagnetic waves in a spatially confined channels. They find numerous applications such as the generation of phase or amplitude modulations in electro-optic modulators in fiber. Due to the light being confined in a small section, high nonlinear effects can be produced. In [47], a broadband, single-pass waveguide with optical parametric amplification achieved 8.3 dB of squeezing at a Fourier frequency of 11 MHz. The waveguide consisted of a 45 mm long ZnO-doped periodically poled lithium niobate (PPLN) crystal. Waveguides have the benefit of being very flexible and allow a fast and easy implementation. However, due to the setup of the waveguide, the output mode of the squeezed light is distorted when it exits the setup. Additionally, a degrading of the squeezing value for high pump powers was observed.

5 Squeezed light enhancement of a heterodyne laser Doppler vibrometer

Laser Doppler vibrometers (LDVs) are used to measure vibrations of surfaces or to analyze turbulences in liquids or gases. They provide precise results with stable readout and find numerous applications not only in research related fields but also for industrial purposes [48]. Typically, LDVs use a heterodyne readout scheme, which allows the detection of signals with large amplitudes compared to the used wavelength (see Section 3.3.2). These measurements are required in aerospace [49], automotive [50] and civil engineering [51]. Other uses include material or biomedical research [52]. Generally, the readout in these fields require high optical powers in the LDV to provide a sufficiently high signal-to-noise ratio. The usage of high power, however, is not always desired. Not only can it cause damage to the sample, but in most situations, it is additionally accompanied by higher expenses. These include, for example, the fulfillment of laser safety regulations or the general costs of high power performing lasers. Here, a squeeze laser is very lucrative as it increases the signal-to-noise ratio without enhancing the light power.

In this chapter, we demonstrate the implementation of a squeeze laser in a laser Doppler vibrometer setup. The LDV was set up at the Clausthal University of Technology (TUC) in the group of Professor Christian Rembe by Mengwei Yu. In a cooperation project between the University of Hamburg (UHH) and the TUC, I prepared the squeeze laser, which was characterized in Chapter 4, for transportation. After the implementation of the squeeze laser into the LDV, we examined the

vibrational motion of a piezo-electric actuator at $1\,\mathrm{MHz}$, which was connected to a highly reflective mirror. In this configuration, the sensitivity of the heterodyne LDV was improved by more than $2.7\,\mathrm{dB}$. The results of this experiment were published in [53].

5.1 Setup of the squeezed light enhanced heterodyne LDV

Laser Doppler vibrometers are able to characterize surface vibration or density fluctuations by detecting the frequency shift caused by the Doppler effect. They have a long history, starting in 1968 in [54] after first measurements with a laser Doppler anemometer were performed four years ago in [55].

The enhancement of a heterodyne interferometer with squeezed light was shown in numerous experiments [56, 57, 58]. Here, the squeezed states are overlapped with the signal on a highly reflective beamsplitter to reduce optical loss, which consequently leads to a strong reduction of the signal power. A different approach was chosen in [59], where two squeezed light fields at different frequencies are used.

Figure 5.1 shows the combined experiment. The LDV (brown) was built by Mengwei Yu at the TUC while I set up the squeeze laser (blue), which was characterized in Section 4.4. A fiber laser from NKT produces quasi-monochromatic laser light at $1550\,\mathrm{nm}$, which is split in a 50:50-fiber splitter to operate both experiments. In the LDV, the light is split into two beams at a polarizing beam splitter (PBS), where the splitting ratio is defined by a $\lambda/2$-waveplate. The beam transmitted at the PBS is called the measurement beam, while the reflected light serves as the local oscillator. The measurement beam passes an acousto-optic modulator (AOM), which can shift the frequency of the beam by $40\,\mathrm{MHz}$. In contrast to previous experiments, that explored squeezed light in heterodyne schemes, the measurement beam is overlapped with the squeezed light on a 93:7-beamsplitter before interacting with the probe. The phase θ between the two fields, which determines the readout quadrature, can
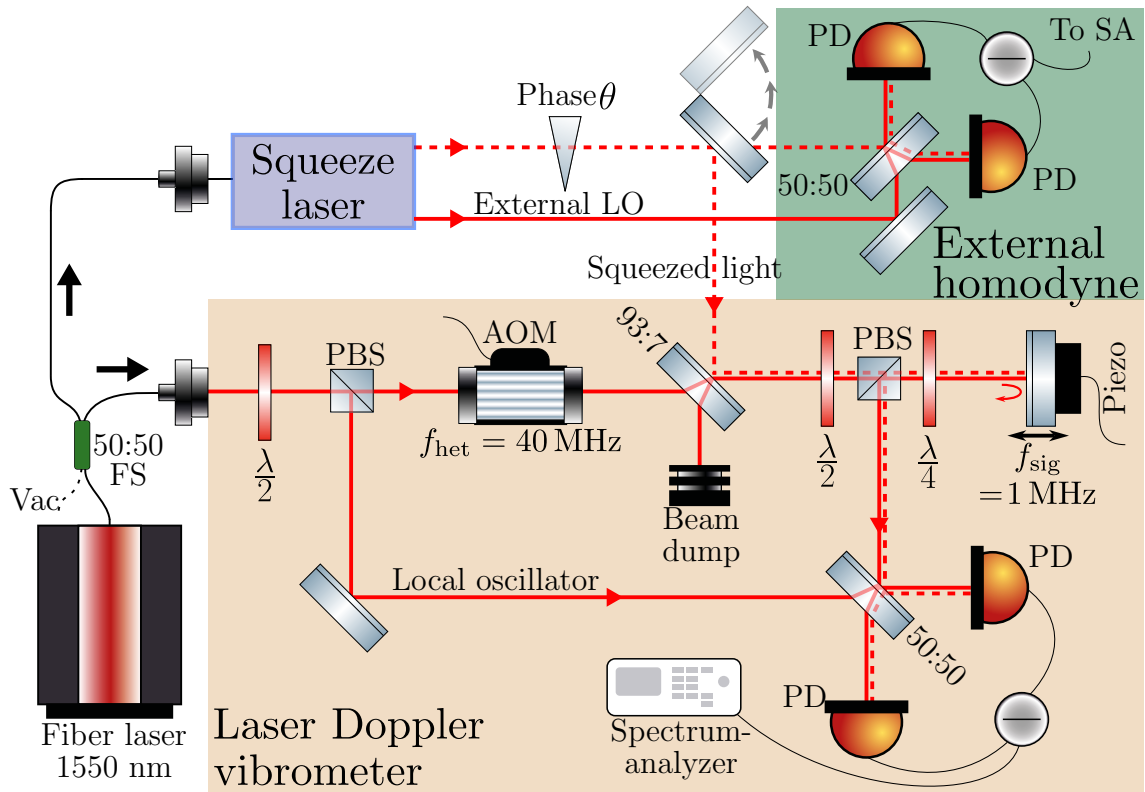
Figure 5.1 – **Schematic of the heterodyne laser Doppler vibrometer with squeezed light enhancement.** The figure displays the schematic of the laser Doppler vibrometer (brown) and the implementation of the squeeze laser (blue). A fiber laser provides the light for both experiments. In the LDV the light is split into a local oscillator (LO) and a measurement beam, which is shifted by an acousto-optic modulator (AOM) by $f_{het} = 40\,\mathrm{MHz}$ and then overlapped with the squeezed light (dashed line) on a 93:7-beam splitter. The combined fields are phase modulated when they are reflected off of the vibrating surface of the oscillating mirror at $f_{sig} = 1\,\mathrm{MHz}$. This signal is analyzed in a heterodyne detection scheme, where it is overlapped with the local oscillator and evaluated on a spectrum analyzer. The squeeze laser was characterized in Section 4.4 and transported from the University of Hamburg to the Clausthal University of Technology. To observe the squeezed states outside of the LDV, a external homodyne detector (green) was set up, which was accessible with a flipping mirror. PD=photodiode, FS=faser splitter, PBS=polarizing beam splitter. SA=spectrum analyzer

be adjusted with a phaseshifter in the beam path of the squeezed light itself. The combined fields are transmitted at a second PBS and a $\lambda/4$-waveplate before they

are reflected off of the sample. In our experiment, this sample consists of a highly reflective mirror connected to a piezo-electric crystal, which is oscillating at a signal frequency of $f_{\mathrm{sig}} = 1\,\mathrm{MHz}$. This oscillation results in a phase modulation on the measurement beam, which was depicted in Figure 3.4 in Chapter 3.3.2. The reflected light passes the $\lambda/4$-waveplate a second time, which results in a rotation of the polarization of 90° compared to the incident beam. The measurement beam is reflected at the PBS and overlapped with the local oscillator at a 50:50-beam splitter. Two photodiodes detect the light power in both arms and their current is subtracted, amplified and evaluated on a spectrum analyzer.

Additionally, an external homodyne detector was set up (green) to characterize the squeeze laser outside of the LDV. In Section 5.5, this homodyne detector was used to characterize the degrading of the system over a time frame of fifteen months.

5.2 Transportation of the squeeze laser

The housing of the $60\,\mathrm{cm} \times 40\,\mathrm{cm}$-sized squeeze laser together with a rack-mounted system for the electrical components is shown in Figure 5.2. This aluminum housing was designed to avoid dust entering the setup and to minimize the damage in the transportation process. Drilling a hole in one of the sides allowed the squeezed states to be guided out of the housing.

The squeeze laser was transported by car to the TUC, which took roughly three hours of driving time. It was then set up on an optical table next to the LDV. To confirm that no damages occurred during the transportation process, a zero span measurement at $5\,\mathrm{MHz}$ was performed on the on-board homodyne detector. This measurement provided $6\,\mathrm{dB}$ of squeezing with $15\,\mathrm{dB}$ of anti-squeezing. The anti-squeezing value affirmed that the squeeze laser was intact while the low squeezing value was explained by the spatial mode mismatch between the squeezed field and the local oscillator, which was not optimized for the measurement.
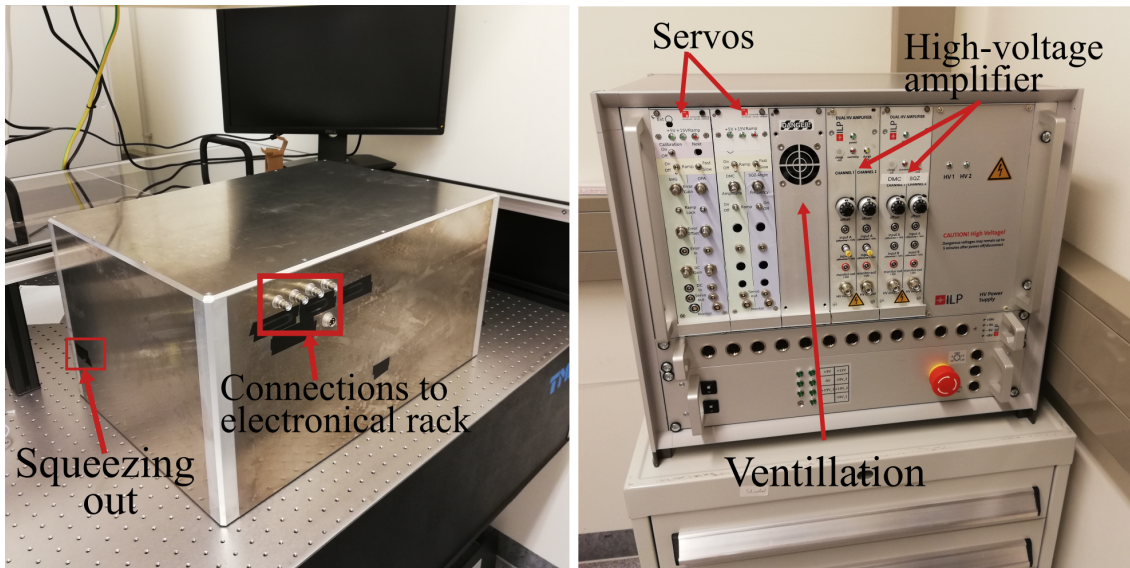
Figure 5.2 – **Aluminum housing (left) and rack-mounted system (right) for the transportation of the squeeze laser and the electrical components. Left:** To avoid damages and to maintain the cleanliness of the optical components, an aluminum housing was placed around the optical setup of the squeeze laser. The top of the housing was removable so that adjustments inside were still possible. A small hole on one side of the housing (covered by tape in the left picture) was used to lead the squeezed light outside of the housing. **Right:** The rack-mounted system contained two servos (two left slots), which provide the length stabilization for the cavities and the generation of ramp signals for the alignment process. To avoid overheating, a fan was implemented inside the rack. Two high-voltage amplifiers were required to enhance the signals from the servos to the piezo-electric elements in the cavities and the phaseshifters.

5.3 Homodyne and heteodyne detection in the squeezed light enhanced LDV

5.3.1 Homodyne measurement

To evaluate the performance of the squeezed light enhanced heterodyne LDV, we first performed two measurements in a homodyne readout scheme similar to the ones shown in Section 4.4. Here, the measurement beam was blocked and only the

squeezed states were overlapped with the local oscillator.

Parameter	Value	
Detection frequency	5 MHz	40 MHz
Local oscillator power	$(20 \pm 1)\,\mathrm{mW}$	$(20 \pm 1)\,\mathrm{mW}$
Pump light power	$(17.00 \pm 0.85)\,\mathrm{mW}$	$(17.00 \pm 0.85)\,\mathrm{mW}$
Anti-squeezing	$(13.77 \pm 0.14)\,\mathrm{dB}$	$(6.15 \pm 0.13)\,\mathrm{dB}$
Squeezing	$(6.32 \pm 0.11)\,\mathrm{dB}$	$(3.74 \pm 0.13)\,\mathrm{dB}$
Optical loss	$(19.52 \pm 0.51)\,\%$	$(23.29 \pm 1.05)\,\%$

Table 5.1 – Measurement specifications for the zero span measurement performed in Figure 5.3 at 5 MHz and 40 MHz.
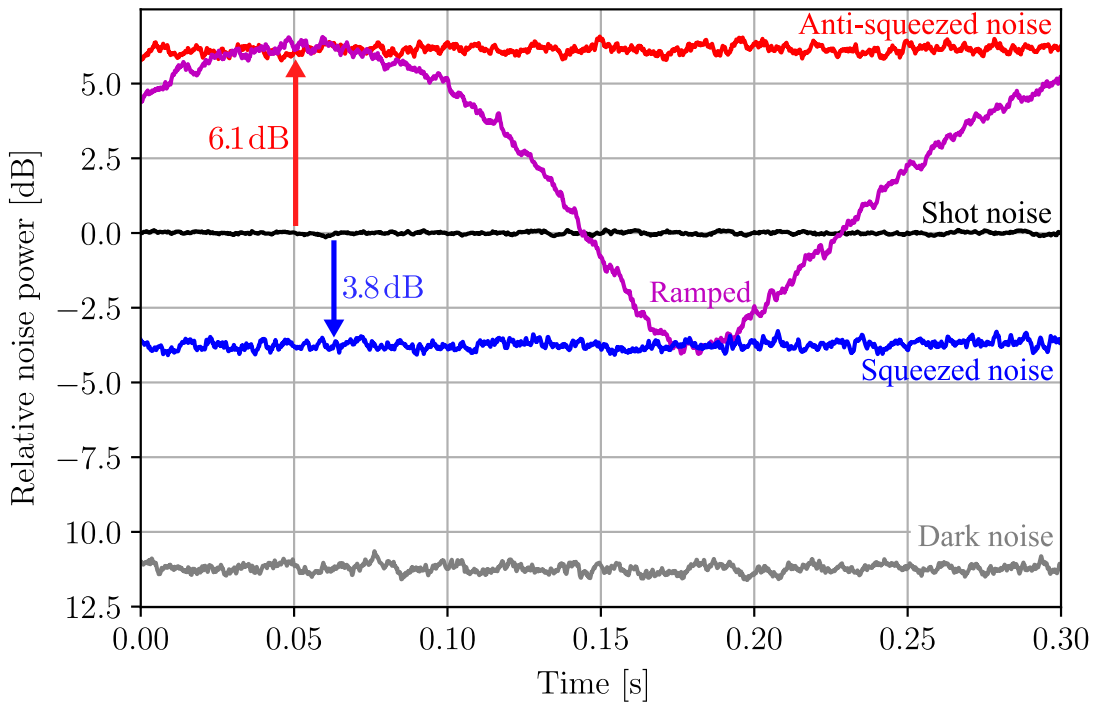
Figure 5.3 – **Zero span measurement at 40 MHz in the homodyne LDV normalized to the shot noise.** This measurement, with the specifications presented in Table 5.1, shows similar squeezing values compared to the one performed in the University of Hamburg (see Figure 4.9) with respect to the included 93:7-beam splitter in the LDV. The RBW for the measurement was 300 kHz and the VBW 100 Hz. The dark noise was not subtracted from the data.

We performed two zero span measurements, one at $5\,\mathrm{MHz}$ and one at $40\,\mathrm{MHz}$, for which the results and specifications are displayed in Table 5.1. The second measurement is shown in Figure 5.3. The dark noise was $11\,\mathrm{dB}$ below the shot noise and was not subtracted from the data.

Compared to the measurement in Hamburg, shown in Figure 4.9, where the optical loss numbered $7.87\,\%$, the loss in this measurement is enhanced due to multiple reasons. First, the squeezed light is passing more optics compared to the measurement in Hamburg: Here, the biggest loss contribution with $7\,\%$ is caused by the beam splitter at which the squeezed field is overlapped with the measurement beam. In addition, the polarizing beam splitter and the $\lambda/4$-waveplate enhance the loss even further due to the absorption of the coatings as well as the spatial deformation of the beam. Furthermore, due to the long path length between the squeeze laser and the LDV, fluctuations in the readout of the squeezed or anti-squeezed quadrature are introduced. These fluctuations are most likely caused by air turbulence and made it difficult to stabilize the squeezing angle (see Section 5.6). Last, the laboratory in the TUC was not a clean room, which results in dust depositing on the optics. After the implementation of the squeeze laser, measures to optimize the purity of the laboratory were established. These measures included working with gloves and using shoe covers and sticky mats.

5.3.2 Heterodyne measurement

For the heterodyne readout, a frequency shifted measurement beam with a light power of $\mathrm{P_{mes}}$ was sent onto the sample, which was not oscillating in this measurement. In Figure 5.4, a spectrum from $38\,\mathrm{MHz}$ to $42\,\mathrm{MHz}$ is presented, which is located around the frequency shift f_{het} of the measurement beam at $40\,\mathrm{MHz}$. The specifications of the measurements are shown in Table 5.2. The bright, frequency shifted light beam at f_{het} is visible as the peak in the spectrum. For $5\,\mathrm{MHz}$, the measurement is cohesive with the one presented in the previous section: The loss values and both the squeezing and anti-squeezing values lead to similar results shown in Table 5.1.

Parameter	Value	
Detection frequency	5 MHz	39 MHz
Local oscillator power	$(20 \pm 1)\,\text{mW}$	$(20 \pm 1)\,\text{mW}$
Measurement beam power	$(20 \pm 1)\,\text{µW}$	$(20 \pm 1)\,\text{µW}$
Pump light power	$(17.00 \pm 0.85)\,\text{mW}$	$(17.00 \pm 0.85)\,\text{mW}$
Anti-squeezing	$(13.28 \pm 0.66)\,\text{dB}$	$(6.35 \pm 0.49)\,\text{dB}$
Squeezing	$(5.45 \pm 0.46)\,\text{dB}$	$(2.44 \pm 0.44)\,\text{dB}$
Optical loss	$(21.80 \pm 2.52)\,\%$	$(39.30 \pm 5.25)\,\%$

Table 5.2 – Measurement specifications and comparison of the zero span measurement performed at 5 MHz and the spectrum around 40 MHz presented in Figure 5.3. In the second measurement, 39 MHz denotes the frequency at which the squeezed values were calculated from. The high loss in the second measurement is dominated by the fluctuating readout quadrature due to the long path length of the squeezed light.

The squeezed and anti-squeezed values are measured at 39 MHz and show surprisingly high loss values of more than 39.3 %. The explanation here is the strongly fluctuating phase due to the long propagation path of the squeezed light, which was mentioned in Section 5.3.1. This effect is enhanced in the second measurement, as the quadrature had to be stabilized for multiple seconds due to the temporal length of the spectrum and the comparable small RBW. Enhancing the RBW was not possible, as the oscillation of the mirror, which will be shown in the next Section 5.4, required a sufficiently small RBW to resolve the signal. Due to time constraints, the measurement could not be improved further. In grey, the dark noise of the measurement depicts a peak at $f_{\text{het}} = 40\,\text{MHz}$, which is caused by the amplification of the AOM. As it is several dB below the peak that is generated by the measurement beam, it did not disturb the measurement.
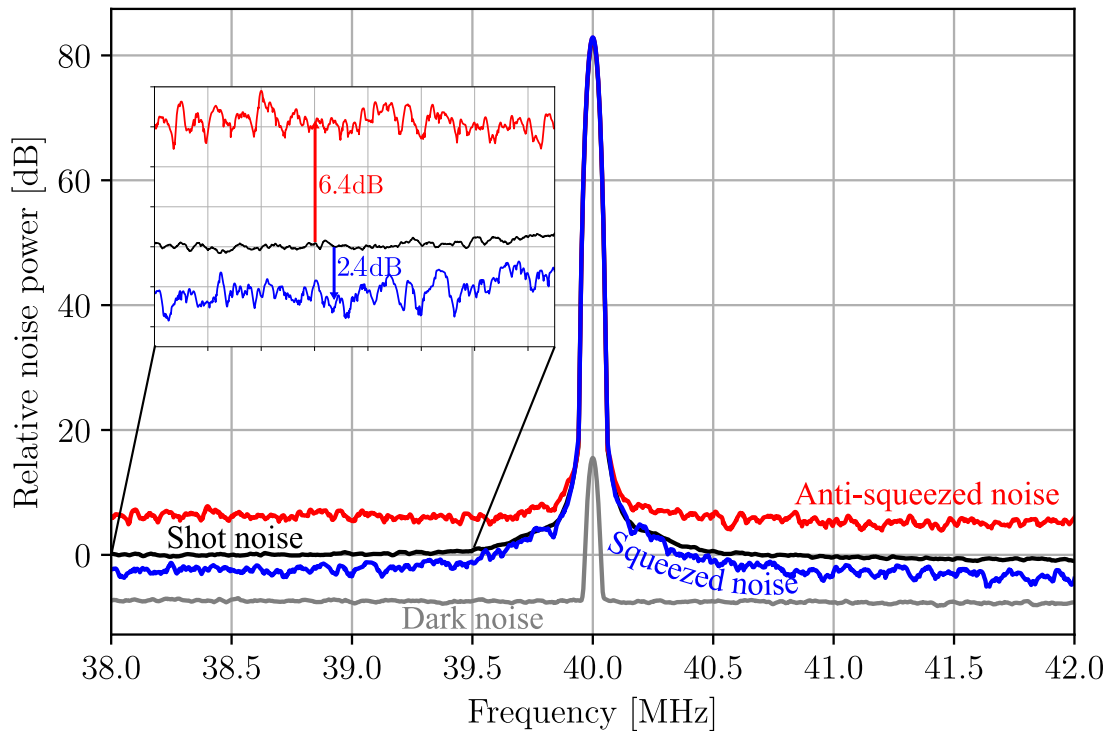
Figure 5.4 – **Spectrum of the squeezed light enhanced heterodyne LDV from 38 MHz to 42 MHz.** The figure shows the dark noise (gray), the shot noise (black) and the squeezed (blue) and anti-squeezed (red) noise on the heterodyne detector. The peak at 40 MHz arises from the frequency shifted measurement beam. At 39 MHz the squeezed noise was 2.44 dB below the shot noise. The RBW was 30 kHz and the VBW 100 Hz.

5.4 Signal detection in the squeezed light enhanced heterodyne LDV

In the following measurement, a sinusoidal voltage was applied to the piezo-electric actuator at a frequency of $f_{sig} = 1$ MHz, which caused the end-mirror of the LDV to oscillate. This oscillation was detected in the heterodyne LDV as two sidebands at $f_{het} \pm f_{sig}$. Figure 5.5 shows a spectrum from 38 MHz to 42 MHz, where the measurement from Section 5.3.2 is repeated but with the vibrating end-mirror. The black trace depicts the shot noise of the measurement together with both the frequency of

| Parameter	Value
Detection frequency	$39\,\mathrm{MHz}$
Local oscillator power	$(20 \pm 1)\,\mathrm{mW}$
Measurement beam power	$(20 \pm 1)\,\mathrm{\mu W}$
Pump light power	$(17.00 \pm 0.85)\,\mathrm{mW}$
Anti-squeezing	$(6.02 \pm 0.51)\,\mathrm{dB}$
Squeezing	$(2.77 \pm 0.61)\,\mathrm{dB}$
Optical loss	$(30.55 \pm 5.96)\,\%$

Table 5.3 – Measurement specifications of the spectrum shown in Figure 5.5.
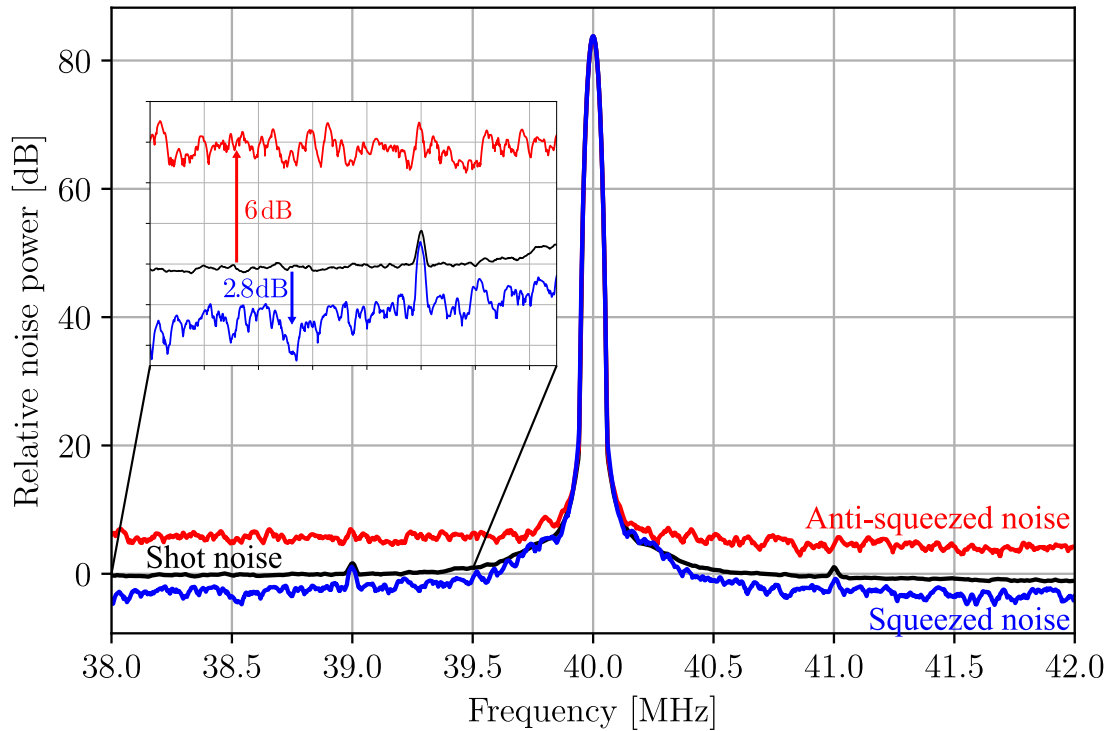
Figure 5.5 – **Spectrum of the squeezed light enhanced heterodyne LDV from 38 MHz to 42 MHz.** The figure shows the shot noise (black) and the squeezed (blue) and anti-squeezed (red) noise on the heterodyne detector. The peak at $40\,\mathrm{MHz}$ arises from the frequency shifted measurement beam. At $38.5\,\mathrm{MHz}$ the squeezed noise was $3.4\,\mathrm{dB}$ below the shot noise, while the anti-squeezed noise was $7\,\mathrm{dB}$ above. The RBW was $30\,\mathrm{kHz}$ and the VBW $100\,\mathrm{Hz}$.

the AOM on the measurement beam at 40 MHz and the signal sidebands at 39 MHz and 41 MHz. The blue and red traces show the implementation of the squeezed states and the resulting squeezed and anti-squeezed noises.

A sensitivity enhancement of 2.77 dB was achieved with a corresponding optical loss of 30.55 %. This high loss value is, similar to the previous section, caused by the readout fluctuation due to the long path length.

5.5 Degrading of the system over time

Squeeze lasers are usually stored in clean rooms, with numerous precautions taken to minimize the amount of dust entering the setup. As this is not standard in most laboratories, the degradation of the system without constant care is inevitable. To quantify this degradation, I visited the TUC fifteen months after the transportation. During this year, the squeezer was both in and out of operation for multiple months.

5.5.1 Squeezed light production and optical loss

At the TUC, the actions taken to reduce the amount of dust were restricted to an air filter, sticky mats, and shoe covers. This means that over time the purity of the squeezed light will suffer as dust will settle on the optics. This degrading was examined with an external homodyne detector, shown in Figure 5.1 in the top right. Upon arrival, this separate homodyne detector was set up outside of the housing of the squeeze laser to provide information on the squeezing performance without opening the housing of the squeeze laser to prevent dust from entering the system. On this (external) homodyne detector, two zero span measurements were performed: One directly after the squeezer was transported to Clausthal-Zellerfeld and the other one fifteen months later. In Table 5.4, they are compared with the measurements from Hamburg presented in Section 4.3.

For all three measurements, I used the same detector (with the same photodiodes)

	Before transportation [UHH]	Upon arrival [TUC]	After fifteen months [TUC]
Squeezing [dB]	10.1	9.5	5.8
Anti-squeezing [dB]	20.1	18	14
Loss [%]	7.9	8.9	23.9

Table 5.4 – **Degrading of the squeeze laser over time.** The three measurements compare the performance of the squeeze laser for different times. In all measurements, a zero span measurement at 5 MHz was performed. The first measurement was taken at the UHH before the transportation, where a clean room was established. Here, the on-board homodyne detector was used. The second one was directly performed after the squeezer was transported to the TUC. Lastly, the third measurement was executed after fifteen months. The measurements in the TUC were performed on the external homodyne detector.

and identical local oscillator powers. Before each measurement, the mode matchings were improved to achieve high visibility over 98 %. The pump power of the squeeze laser varied slightly due to temperature drifts of the ambient air in the laboratory. To a certain degree, these drifts can be compensated with the temperatures of the TECs inside the cavities. Still, this caused the conversion efficiency to change throughout the day and resulted in varying anti-squeezing values in the measurement.

The degrading from the first to the second measurement is likely explained due to spatial mismatch and a decrease in the visibility at the beam splitter: Less time was spent on optimizing the overlap of the local oscillator and the squeezed light field.

The decrease from the second to the third measurement is surprisingly high. Here, I suspect dust on top of the mirrors or directly on the photodiodes of the external homodyne detector, as such a high degrade in purity cannot be explained otherwise. As the results of the laser Doppler vibrometer with homodyne readout (see Figure 5.3) displayed a similar loss values, although it included the 93:7-beam splitter, the increasing loss value has to appear in the external homodyne setup.

5.5.2 Electrical components

The electrical support of the squeeze laser consists of the 19-inch rack with its servos, high-voltage amplifiers, and the power supply (depicted in Figure 5.2), together with the photo detectors in the optical setup and the temperature controller required for the cavities. All of these components were built by myself, Jan Südbeck, and Dieter Haupt.

After fifteen months, the electronic components showed no signs of degrading. The length stabilization of the cavities worked extremely well, and due to the auto-locking schemes (see Section 4.2.5), the squeeze laser can be operated nearly continuously even when external disturbances impede the system. Such disturbances especially occur when mechanical work on the optical table was performed, for example, when optical components were mounted or shifted for alignment purposes.

The temperature control systems for the SHG and the PDC cavity both performed as well as they did in Hamburg. As the laboratory in the TUC has no air conditioning, the ambient temperature was slowly drifting throughout the day. Although the temperature of the TECs in the cavity heated the actuator to temperatures between $40\,°C$ and $50\,°C$, these temperature drifts affected the temperature inside the cavity and caused a slow decrease in the conversion efficiency throughout the day. It was, therefore, necessary to adjust the temperature of the TECs hourly.

5.6 Loss contribution, limitations and outlook

In this chapter, we demonstrated the proof-of-principle experiment of a squeezed light enhanced heterodyne laser Doppler vibrometer with a sensitivity enhancement of more than $(2.77 \pm 0.61)\,dB$. In contrast to previous experiment, that combined squeezed light and heterodyne readout, here, the full squeeze factor can be utilized to increase the signal-to-noise ratio without discarding parts of the signal. The main loss contributions come from the 93:7-beam splitter, which is required for overlapping the squeezed light with the measurement beam. Additional loss sources

are the spatial overlap of the squeezed field with both the measurement light field and the local oscillator, as well as dust in the setup and the quantum efficiency of the photodiodes. Another limitation, that reduces the measured squeezed values, was caused by fluctuations in the readout quadrature. These fluctuations are caused by air turbulence in the laboratory. Due to the long path length between the squeeze laser and the LDV, stabilizing the squeezing angle was difficult, especially for longer measurement times. For future measurements, a housing can prevent this problem. Lastly, both the squeezing and the anti-squeezing value were limited by the optical bandwidth of the cavity at higher frequencies and the bandwidth of the detector.

Furthermore, we demonstrated that the squeeze laser can be transported, implemented, and utilized even by groups that are not accustomed to working with squeezed light. The degrading of the system over a period of fifteen months was characterized and showed promising results, as the performance of the squeeze laser was only reduced due to dust inside the laboratory and not due to problems caused in the squeeze laser itself.

As mentioned in Section 3.3.2, the heterodyne readout has some advantages compared to the homodyne system: The detection of signals with optical path length changes with multiple wavelengths amplitude and the shift of the measurement frequency to reduce the effect of the dark noise of the detector. The application of the squeezed light enhanced heterodyne LDV is, however, limited to small amplitudes. The reason for this is that signals with amplitudes larger than one interferometer fringe cause the readout quadrature to swap, which is determined by the phase between the local oscillator and the squeezed light. This results in a shift from squeezed to anti-squeezed shot noise, which limits the sensitivity. Therefore, one major benefit of the heterodyne detection scheme is unusable. Now, the major advantage of the heterodyne readout is the shifted detection frequency, which can reduce the dark noise of the detector as well as that there is no feedback loop requires to lock the interferometer. One application for the squeezed heterodyne laser Doppler vibrometer, therefore, lies in the detection of small signals at low frequencies. Another utilization are experiments that prohibit the enhancement of the optical power. This is the case when working with biomedical probes or when the power threshold of the

photodiodes is approached. Another valuable benefit of the heterodyne detection is the post processing and the associated feedback loops. For homodyne schemes, the arm lengths of interferometer have to be stabilized, typically to the mid-fringe condition. With heterodyne readout, one feedback loop is saved as the information about phase and amplitude quadrature is obtained in the post processing of the data.

6 Detection of ultrasonic sound waves improved by squeezed light

Non-contact and non-destructive measurements provide a vast spectrum for detecting and analyzing vibrating structures or density fluctuations. A prominent system for these types of measurements is the laser Doppler vibrometer, which was introduced in Chapter 5. Here, laser light is sent onto the vibrating surface directly and the reflected light contains information about the oscillation of the sample. However, this topology is disadvantageous for rough and uneven surfaces, or for surfaces with low reflectivities or high absorption [60]. For rough surfaces, enhancing the laser power increases the signal-to-noise ratio, but is often not compatible with eye safety requirements in industrial applications. As for highly absorbing probes, e.g. with a black surface, high laser power can cause damage on the sample itself. In both cases, the injection of squeezed light would suffer from the introduced optical loss.

An alternative approach, that allows to evade this issue, is detecting air density fluctuations caused by the vibration of the sample. Here, the light beam travels parallel to the surface and acquires a phase shift due to the sound waves, which is then detected interferometrically. This method requires high sensitivity due to the low acoustic impedance of air. Here, the usage of a squeeze laser is very lucrative as the interaction between the sound wave and the laser light does not introduce any additional optical loss.

In this chapter, I show the detection of sound waves of a vibrating transducer at ultrasonic frequencies between 4.2 MHz and 7.2 MHz. The measurement is performed

in a homodyne Mach-Zehnder interferometer. Here, a highly squeezed state is injected in the interferometer to improve the signal-to-noise ratio. The measurement of high squeezing levels of more than $10\,\mathrm{dB}$ in a Mach-Zehnder interferometer was already proven in [61]. The high sensitivity of this setup allows the detection of pressure changes caused by the sound wave up to $0.12\,\frac{\mathrm{mPa}}{\sqrt{\mathrm{Hz}}}$. By analyzing the interaction between the optic and the acoustic field, information about the amplitude and the frequency of the sound waves can be derived. With this information, I provide a precise characterization of the absorption coefficient, which is a crucial parameter for describing the attenuation of the acoustic waves, for different frequencies and air temperatures.

6.1 The acousto-optic interaction

The interaction between acoustic and optical fields arises from the fact, that sound waves create refractive index changes when propagating through a medium due to the pressure changes of the waves themselves. When light moves through an acoustic field, this interaction creates effects such as diffraction, deflection and interference. Detecting these effects provides information about the initial fields.

Typically, one distinguishes between two types of acousto-optic interaction: Optical diffraction and optical deflection or refraction. Both of these phenomena depend on the relation of the wavelength of the sound wave Λ and size of the laser beam ω.

In **light diffraction** techniques the wavelength of the sound wave is smaller than the beam size ($\Lambda < \omega$). In this case the acoustic wave acts as a diffraction grating for the light field. Similar to solid gratings this leads to constructive and destructive interference while the light is propagating through the sound wave and results in a interference pattern, which depends on the properties of the sound wave. This effect was first shown in [62] and has ever since been the topic of multiple studies [63, 64]. One famous application of this technique is used in an acousto-optic modulator (AOM) to generate intensity modulations or to shift the frequency of the initial light. The AOM consists of a transducer that is directly connected to a transparent

crystal. The sound waves emitted by the transducer lead to a strain wave propagating through said crystal. This effect is called the photoelastic effect and it directly leads to a periodic change in the refractive index in the crystal, which produces a diffraction pattern when light is passing perpendicular thought the medium. By choosing the right angle, the so-called Bragg angle, between the light field and the crystal, most of the higher order modes of the diffraction pattern can be suppressed but the desired one. This produces a frequency shifted and spatially separated light field. In Chapter 5, an AOM was utilized to produce the measurement beam for the heterodyne readout. Recently in [65], the generation of an acoustic-optic modulator in air was demonstrated, where a frequency shifted beam at $f = 490\,\mathrm{kHz}$ with a pulsed laser beam passing a ultrasonic sound wave was created.

On the other hand **optical refraction** assumes the beam size of the light field to be smaller than the wavelength of the sound waves

$$\omega < \Lambda. \tag{6.1}$$

In this regime the light is ideally only passing through either a compression or a rarefaction of the sound wave. This means that there is no diffraction effect, but the light field experiences a phase modulation based on the frequency of the acoustic wave. This effect was studied in liquid and gases and finds applications especially in light refractive tomography. It was first introduced in 1993 in [66] with ultrasonic pulses in a heterodyne laser Doppler vibrometer in water and further investigated in different fluids [67, 68] and gases [69, 70]. Ever since most experiments for the analysis of sound pressure fields with optical refraction use commercially available laser Doppler vibrometer in both air and water with acoustic frequencies between $f = 40\,\mathrm{kHz}$ and $f = 1\,\mathrm{MHz}$ [71, 72, 73].

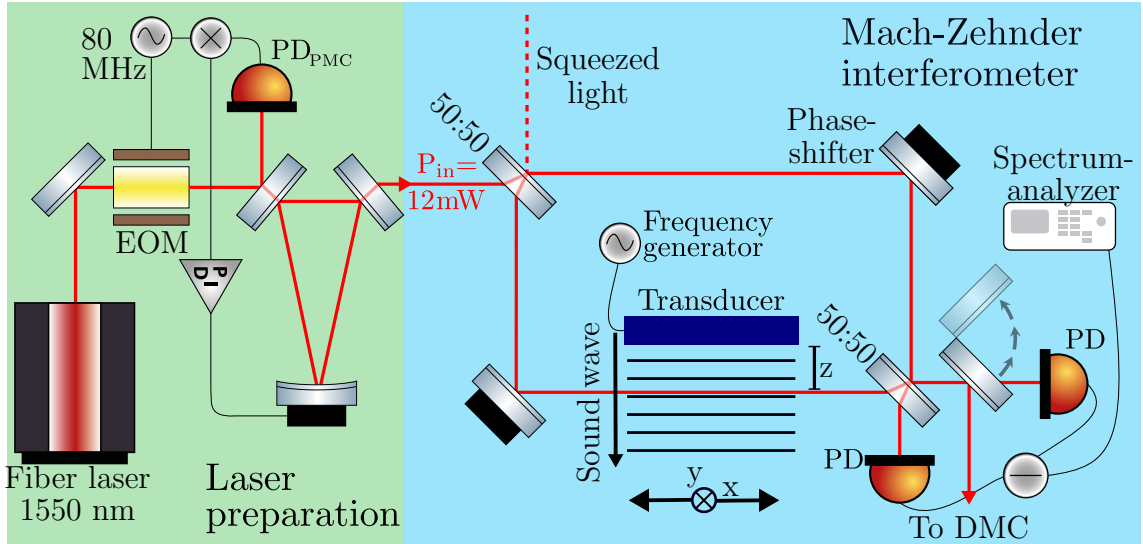In this thesis I analyze the effect of optical refraction.

Figure 6.1 – **Setup of the homodyne Mach-Zehnder interferometer for the detection of ultrasonic sound waves in air.** The setup is divided into different sections, highlighted by different colors. First, in green, the spatial mode is optimized in a pre-mode cleaner, which is stabilized with a Pound-Drever-Hall locking scheme. A 12 mW strong light beam is sent into the Mach-Zehnder interferometer in blue, where it is divided into two parts. In both arms the beam is focused by a lens with a focal length of f=+50 to ensure that the beam waist is smaller than the wavelength of the sound wave. This is followed by a second lens with the same proportions to prevent the beam from diverging. A transducer generates sound waves perpendicular to the beam propagation, which produce a phase modulation at the frequency of the acoustic wave. The light is recombined on a second 50:50-beam splitter and detected in a balanced homodyne scheme (brown), where the AC-output is used to detect the signal of the ultrasonic sound waves and the DC-output is fed back to a control loop to stabilize the interferometer on the mid-fringe condition. FR=faraday-rotator, EOM=electro optical modulator, PD=photodiode, DMC=diagnostic mode cleaner.

6.2 Setup

To analyze the ultrasonic sound waves I modified a Mach-Zehnder interferometer (MZI), which was set up and characterized by Jascha Zander in [74]. A simplified schematic of the experimental setup is shown in Figure 6.1. Quasi-monochromatic light is generated by a fiber laser provided by *NKT Photonics* at 1550 nm. It passes through an electro-optic modulator to produce sidebands at a frequency of 80 MHz. The spatial mode shape is optimized with a pre-mode cleaner (see Section 4.2.3) before being guided into the interferometer. In the MZI, the light is split into two equal parts at a 50:50-beam splitter. The two created light paths are individually reflected at a mirror and then recombined at a second 50:50-beam splitter. In a balanced homodyne detection scheme both output ports are analyzed simultaneously with two photodiodes. When the interferometer is operated at the mid-fringe condition the optical power on both photodiodes is equal. Their currents are subtracted and split in DC and AC components with a high-pass filter. The AC-output of the detector was connected to a spectrum analyzer from *Rhode und Schwarz*.

In one of the arms of the MZI, referred to as the reference arm, a phaseshifter is placed to periodically modulate the length. It consists of a highly reflective mirror, which is connected to a piezo-electric actuator. For the alignment of the interferometer, a sinusoidal voltage is applied to this phaseshifter, which results in a periodic change in the length of the reference arm. When recombined at the second beam splitter this length change leads to periodic constructive and destructive interference between the two beams. At the homodyne detector this is visible as a varying voltage oscillating with the frequency applied to the phaseshifter. The maximum and the minimum of this voltage is used to calculate the contrast or the visibility of the interferometer (see equation 4.1). In the measurement process the phaseshifter is used to stabilize the interferometer at the mid-fringe condition. Here, the derivation of the sine is maximal and the interferometer is most sensitive to phase-modulations. For the stabilization, the DC signal of the detector is used as the error signal for PID-control loop. All measurements in the homodyne Mach-Zehnder interferometer are performed at the mid-fringe condition.

In the other arm of the MZI, referred to as the signal arm, a piezo-electric transducer produces ultrasonic sound waves. The transducer used for all measurements is a dual element transducer from *Smart Sensor*. It has a diameter of 15 mm and its resonance frequency is 5.204 MHz. The signal used to produce the sound waves was generated by a self-built frequency generator and amplified before it was lead to the transducer. This amplification was necessary due to the low acoustic impedance of air.

In the experiment, the transducer is placed in a way such that the ultrasonic waves travel perpendicular to the propagation direction of the light field. If the beam waist ω_0 of the laser is smaller than the wavelength Λ of the sound waves, the light experiences a change in the refractive index proportional the frequency of the sound waves. This results in a phase modulation on the light, which can be detected as an interference pattern at the outputs of the MZI.

To ensure $\omega_0 < \Lambda$, two lenses with a concave surface and a focal length of $f = 50$ mm are placed in the signal arm. The first lens focuses the beam down to a size of 31 µm. To achieve high spatial overlap at the second beam splitter between the two beams and therefore a high visibility, the same lens setup was placed in the reference arm. As the wavelength of the sound waves decreases for higher frequencies (see equation 6.2) one challenge here is to find a balance between beam waist size and beam divergence. One generally wants to the beam to be as small as possible to fulfill the condition from equation 6.1. However, it is also necessary for the beam size to remain smaller than the wavelength across the entire interaction distance, which in turn requires a minimal divergence. In our case, the Rayleigh length for a beam waist of $\omega_0 = 31$ µm is $z_R = 1.95$ mm.

A diagnostic ring cavity (see Section 4.2.4) is used to optimize the spatial overlap of the signal and the reference beam. In Section 6.4, I use a squeeze laser to enhance the sensitivity of the system. Here, the cavity is additionally used to overlap the squeezed field with the light in the interferometer.

6.3 Ultrasonic sound waves in the Mach-Zehnder interferometer

Sound waves in air are longitudinal waves consisting of different sections called compression and rarefaction. They are characterized by their frequency f and the speed of sound c_s, resulting in the wavelength

$$\Lambda = \frac{c_s}{f} \, .$$ (6.2)

In this thesis the frequency f is determined by the vibration frequency of the surface of the transducer, which can be adjusted with a frequency generator. Due to the bandwidth of the transducer, the frequency of created sound waves were in the range of $4.2\,\text{MHz}$–$7.2\,\text{MHz}$. With $c_s = 343\,\text{m}\,\text{s}^{-1}$, the wavelength numbered between $47\,\text{µm}$ and $81\,\text{µm}$. Stated in Section 6.1, the light experiences changes in the refractive index of the medium when it is propagating through the sound wave. Following [73] this change can be converted into pressure with the piezo-optic effect:

$$n(x, y, z, t) = n_0 + \Delta n(x, y, z, t)$$ (6.3)

$$= n_0 + \left(\frac{\delta n}{\delta p}\right) \cdot p(x, y, z, t)$$ (6.4)

Here, n_0 is the refractive index of air without any ultrasonic sound wave and $\Delta n(x, y, z, t)$ describes the change of the refractive index caused by the propagating sound wave, where x describes is the propagation direction of the light, y is the vertical position and z the horizontal. With the piezo-electric coefficient of the medium $(\frac{\delta n}{\delta p})$, changes in the refractive index Δn can be connected to the actual pressure changes Δp of the sound wave. The piezo-electric coefficient is almost constant over small pressure changes, which is true for all our measurements, and depends on the temperature of the medium. It was calculated by using the ideal gas condition

with the Gladsone-Dale relation [75]. At room temperature and static pressure, the piezo-electric coefficient in air is $\left(\frac{\delta n}{\delta p}\right) = 2.072 \cdot 10^{-9} \, \frac{1}{\text{Pa}}$.

The interaction of a light beam in the interferometer traveling in x-direction can be described by the effective length change

$$\Delta L(y, z, t) = \int_{x_1}^{x_2} \Delta n(x, y, z, t)\mathrm{d}x \tag{6.5}$$

$$= \left(\frac{\delta n}{\delta p}\right) \int_{x_1}^{x_2} p(x, y, z, t)\mathrm{d}x \tag{6.6}$$

$$= \left(\frac{\delta n}{\delta p}\right) p(y, z, t) \int_{x_1}^{x_2} \exp\left(-2x^2/w_x^2\right)\mathrm{d}x \,. \tag{6.7}$$

The pressure field in x-direction can be described by a Gaussian fit, which is further elaborated in Section 6.5. w_x describes the width of this fit and x_1 and x_2 the distance in which the acoustic and the optical field can interact. This is estimated by the Rayleigh length, which numbered $x_R = 1.95\,\text{mm}$, where the radius of the beam is larger than the wavelength of the acoustic waves and therefore, condition 6.1 is not met anymore.

The optical path length difference can be obtained by the height of the peak in the spectrum. To convert the electrical power in dBm, which the spectrum analyzer is providing, to an amplitude spectral density in $\frac{\text{m}}{\sqrt{\text{Hz}}}$, I use the shot noise in our measurement as a calibration. This calibration method was utilized in [74] and [76]. Following [25] the square root of the spectral density of the theoretical, single-sided shot noise in the Mach-Zehnder interferometer normalized to a displacement x in one of the arms is given by

$$\sqrt{S_{\text{SN},x}^{\text{MZI}}} = \sqrt{\frac{hc\lambda}{2\pi^2 P_{\text{in}}}} \,. \tag{6.8}$$

Here $h = 6.626 \cdot 10^{-34}\,\text{J\,s}$ is the Planck constant, $c \approx 3 \cdot 10^8\,\frac{\text{m}}{\text{s}}$ the speed of light
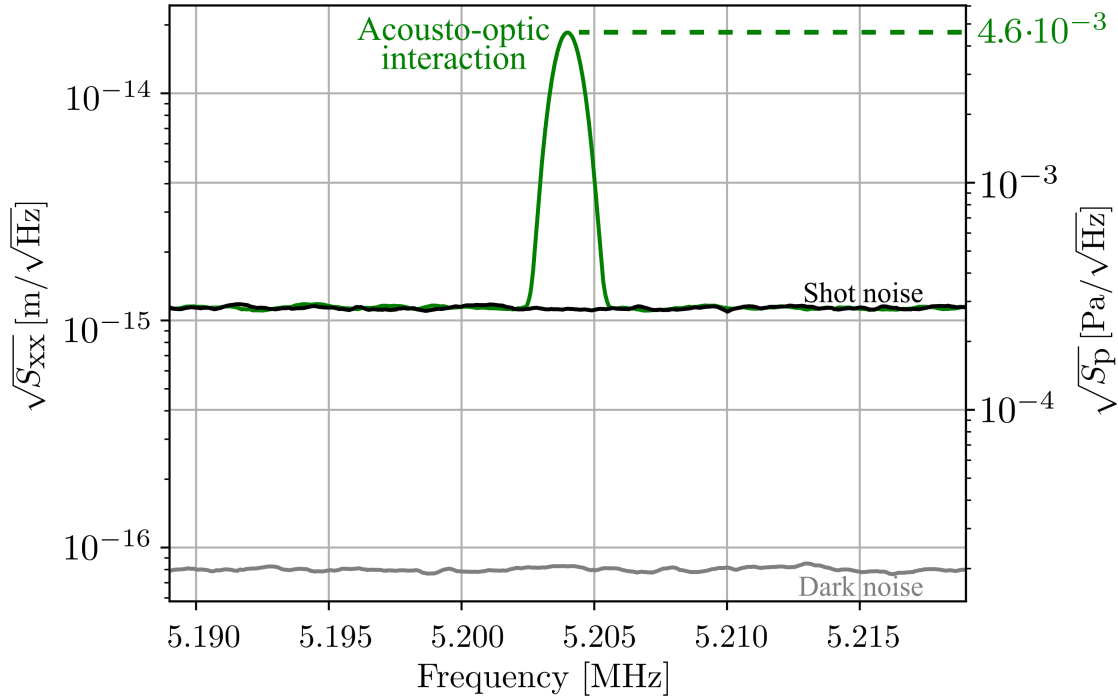
Figure 6.2 – **Spectral density and pressure of the acousto-optic interaction at 5.204 MHz.** The figure shows the acousto-optic interaction as a clear peak (green) in the spectrum at the resonance frequency of the transducer. The height of the peak was 25 dB above the shot noise and was converted into an amplitude spectral density in $\frac{m}{\sqrt{Hz}}$ and in $\frac{Pa}{\sqrt{Hz}}$. The shot noise (black) was measured while the path between the transducer and the laser beam was blocked, ensuring that the peak is not caused by other effects such as electromagnetic stray fields. The dark noise (gray) was 23 dB below the shot noise and was therefore neglectable. The spectra were measured with a resolution bandwidth (RBW) of 1 kHz and a video bandwidth of 10 Hz. The total power in the interferometer was $P_{in} = 12$ mW. The width of the ultrasonic interaction is limited by the RBW. The interaction strength of the two fields determines the height of this peak and for all future measurements, the maximum value of the peak was used to compare changes in the acousto-optic interaction.

and $\lambda = 1550$ nm the laser wavelength. With $P_{in} = 12$ mW as the light power in the interferometer measured before the first beam splitter, the shot noise numbers

$$\sqrt{S_{SN,x}^{MZI}} = 1.14 \cdot 10^{-15} \frac{m}{\sqrt{Hz}} \,. \tag{6.9}$$

With this calibration, the power of the ultrasonic peak is converted in units of dBm to $\frac{\text{m}}{\sqrt{\text{Hz}}}$ with the equation

$$\sqrt{S_{\text{US},x}} = \sqrt{10^{\frac{1}{10}(P_{\text{US,dBm}} - P_{\text{shot,dBm}})} S_{\text{SN},x}^{\text{MZI}}}, \tag{6.10}$$

where $P_{\text{US,dBm}}$ and $P_{\text{shot,dBm}}$ describe the noise power of the ultrasonic peak and the shot noise respectively, which are given by the spectrum analyzer. Finally, the amplitude spectral density of the pressure field p of the ultrasonic wave is calculated with

$$\sqrt{S_{\text{US},p}} = \frac{\sqrt{S_{\text{US,x}}}}{\Delta x} \left(\frac{\delta n}{\delta p}\right)^{-1}, \tag{6.11}$$

where $\Delta x = x_R = 1.95\,\text{mm}$. In Figure 6.2, the interaction of the ultrasonic sound waves and the laser light, described by the spectral density in $\frac{\text{m}}{\sqrt{\text{Hz}}}$ and the pressure in $\frac{\text{Pa}}{\sqrt{\text{Hz}}}$, is visible as a peak at 5.204 MHz in the spectrum from 5.189 MHz to 5.219 MHz. The height of this peak at $1.85 \cdot 10^{-14}\,\frac{\text{m}}{\sqrt{\text{Hz}}}$ or $4.58 \cdot 10^{-3}\,\frac{\text{Pa}}{\sqrt{\text{Hz}}}$ determines the interaction strength and was used to compare the response of the acousto-optic interaction to different frequencies or environmental changes in the following sections. In this configuration the shot noise in black limits the sensitivity at $0.28\,\frac{\text{mPa}}{\sqrt{\text{Hz}}}$, while the dark noise of the detector in gray is 23 dB below the shot noise and therefore negligible. The resolution bandwidth was 1 kHz and the video bandwidth 10 Hz. Here, the width of the peak is determined by the resolution bandwidth. The shot noise in black was measured by blocking the transducer, while the dark noise of the detector was detected when the laser light was blocked. It is shown to verify that the peak arises due to pressure changes in the air and not due to an electromagnetic stray field (see Section 6.7).

6.4 Squeezed light enhanced detection

As mentioned in the introduction of this chapter, conventional interferometric detection of vibrations involves sending light directly on the probe and analyzing the reflection, as shown in Chapter 5. For rough or uneven surfaces, however, speckle
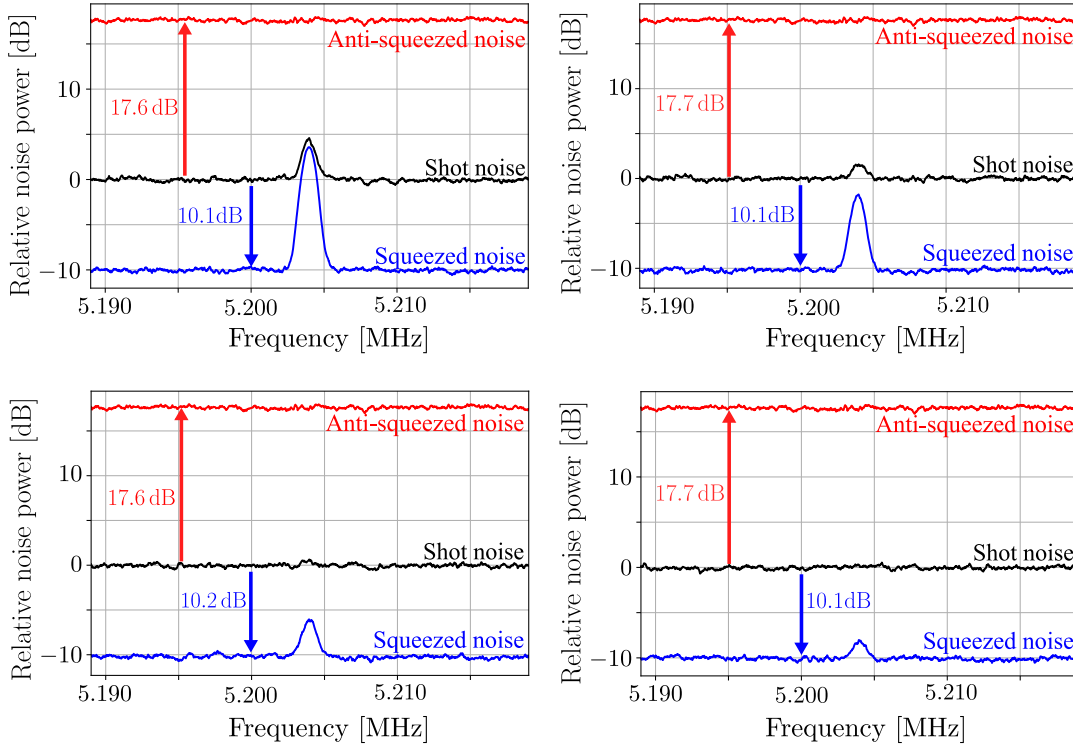
Figure 6.3 – **Detection of the acousto-optic interaction with squeezed light enhancement.** The figures shows how squeezed light enhances the detection of the ultrasonic peak for different signal strengths, which were varied by applying different voltages to the transducer. The squeezed (blue) traces show a reduced noise power of more than 10 dB in each figure, while the anti-squeezing trace (red) is about 17.7 dB above the shot noise. The readout quadratures were stabilized and averaged over 30 times. In the fourth picture (bottom right) the peak is only visible with the injection of squeezed light. The measurements were performed at room temperature. The local oscillator power was $P_{\mathrm{in}} = 12\,\mathrm{mW}$ and the RBW= $1\,\mathrm{kHz}$ and VBW= $10\,\mathrm{Hz}$. The dark noise was more than 20 dB below the shot noise and was not subtracted from the data.

noise, caused by scattering on the surface, can limit the sensitivity of the setup. Additionally, this type of measurement faces challenges when the absorption of the surface is high. Enhancing the optical light power increases the signal-to-noise ratio, but is only possible to a certain degree, especially for highly absorbing probes, where damages due to heating can be caused. In that case, applying squeezed light would not be feasible as the optical losses from the absorption directly reduce the purity

of the squeezed states.

For detecting sound waves, generated by the vibrating surface, squeezed light can greatly enhance the sensitivity: The measurement of the vibrations of the transducer is indirect as the sound waves only interact with the laser light by changing the refractive index of the air that the laser is propagating through. Therefore, no additional optical loss is introduced and the purity of the squeezed states is preserved. The utilization of high values of squeezing in a Mach-Zehnder interferometer was successfully demonstrated by Jascha Zander in [61]. He detected an artificial signal at 5 MHz, generated by an oscillating piezoelectric crystal glued to a mirror, with a shot noise reduction of more than 10 dB.

The squeeze laser for this experiment was built by Tobias Gehring and Vitus Händchen, and used by Jascha Zander in his PhD thesis [74]. In this topology, shown in Figure 6.1, two fields, the squeezed field and the local oscillator field, have to be aligned with respect to each other in both of the arms of the interferometer to reduce optical losses. To keep the losses as small as possible, both fields were separately sent onto the DMC while one of the arms was blocked. The order of aligning the different beam paths was done in the following order: First, the local oscillator through the signal path. Second, the local oscillator through the reference path, and third the control field, representing the squeezed light, through the signal path.

Figure 6.3 shows the spectra of the ultrasonic sound peak for different interaction strengths between the acoustic and the optical field, both with and without the injection of squeezed light, normalized to the shot noise. I simulated the decrease of the interaction strength by reducing the electrical power of the frequency generator. The optical power sent into the Mach-Zehnder interferometer remained at $P_{\text{in}} = (12.0 \pm 0.6)\,\text{mW}$. The measurement shows, that the resolution of the ultrasonic peak enhances when the squeezed light is injected into the interferometer. The squeezed light enhanced spectra were more than 10 dB below the shot noise for all signal strengths, which corresponds to a sensitivity enhancement that would require a power increase of a factor of 10. The mean squeezing value was $(10.14 \pm 0.08)\,\text{dB}$, while the mean anti-squeezing value numbered $(17.67 \pm 0.09)\,\text{dB}$ and result in $(7.8 \pm$

0.1) % of optical loss. The dark noise was more than 20 dB below the shot noise and was not subtracted from the data in the plots. Notably, in the fourth picture, the peak becomes visible only, when squeezed light is employed. Converting the signal to units of $\frac{\text{Pa}}{\sqrt{\text{Hz}}}$ resulted in the detection of a signal with the strength of $(0.12 \pm 0.02) \frac{\text{mPa}}{\sqrt{\text{Hz}}}$.

The results are cohesive with previous experiments: In 2016, a direct squeezing measurement on a balanced homodyne detector from Tobias Gehring and Vitus Händchen resulted 11.1 dB of squeezing, 16.6 dB of anti-squeezing and a corresponding optical loss of 5.4 % [77]. Five years later in [74], Jascha Zander detected 10.5 dB of squeezing and 21.1 dB of anti-squeezing in the homodyne Mach-Zehnder interferometer, leading to 7.8 % of optical loss. The comparison with these experiments shows, that no additional loss is present due to the sound waves. Additionally, there is no degrading of the system over a period of 8 years. In all measurements, the squeeze laser was operated in a clean room.

6.5 Dependence of the acousto-optic interaction on the spatial position of the transducer

In optical refraction, the laser lights beam waist ω_0 has to be smaller than the sound wave wavelength Λ. Due to the divergence of the optical beam, there is a distance between the in x- and y-direction at which this condition will not be fulfilled anymore, depending on the waist of the beam. This leads to the following challenge: Focusing the laser beam down strongly leads to a high divergence and a smaller Rayleigh length, which reduces the interaction area, where the $\omega < \Lambda$ is true. The Rayleigh length of a Gaussian beam characterizes the length z after which the beam radius increased by a factor of $\sqrt{2}$. In this setup, the laser beam is focused down to a size of $\omega_0 = 31\,\mu\text{m}$ and has a Rayleigh length of $z_\text{R} = 1.95\,\text{mm}$. Consequently a bigger waist, which still fulfills condition 6.1, leads to smaller interaction strength, but a higher Rayleigh length and therefore, a larger detection area.
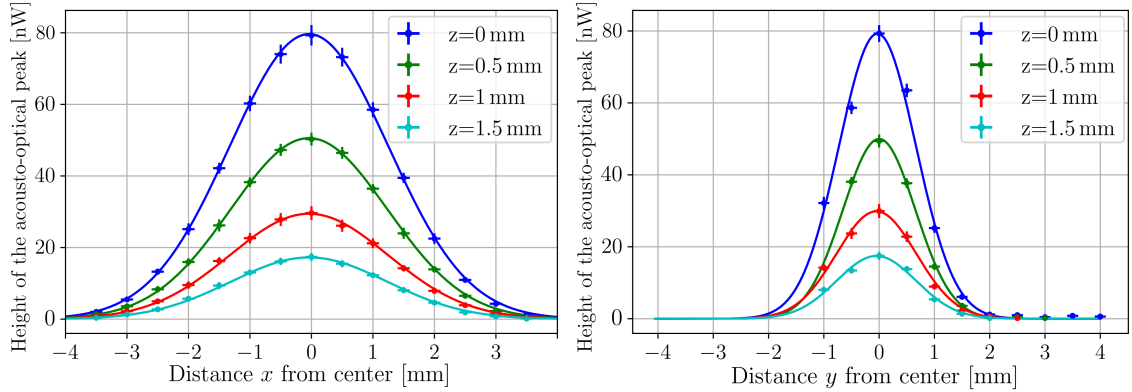
Figure 6.4 – **Dependence of the height of the ultrasonic peak on its relative position in x- and y-direction.** Each data point represents the height of the ultrasonic peak for different position. In the left picture, the y-distance was kept constant at its maximum. For each trace the x-distance was shifted for a fixed z-distance in 0.5 mm-steps. This procedure was repeated for different z-values between 0 mm–2 mm, where $z = 0$ describes the distance at which the transducer can not be moved closer to the optical beam. In the right picture the same measurement for variable y-distance and fixed x-distance was conducted. Here, the size of the translation stage prevented the acquisition of data points below -1 mm. The measurements follows a Gaussian structure, where the width of the Gaussian fit from equation 6.12 is larger for the x-distance than for the y-distance.

To find the position of the transducer at which the interaction between the acoustic field and the light field is strongest, I implemented a translation stage to allow adjustment of micrometer precision in x-, y- and z-direction. In Figure 6.4, I analyzed the x- and y-direction with a fixed distance in the z-axis. All measurements were performed at the same frequency $f = 5.204$ MHz and each data point describes the maximum of the ultrasonic peak for said parameters. The peak height was converted from units of dBm into linear units of W. Before each measurement, I scanned the x- and y-direction to find the global maximum of both directions. The point at which the ultrasonic peak was at its highest value, was designated as $P_{\max} \coloneqq P(x = 0, y = 0)$. For all measurements in the x-direction, the y axis was kept at its maximum value (at $y = 0$). After the x-axis was scanned, the x-position was fixed to its highest value and the y-axis was scanned.

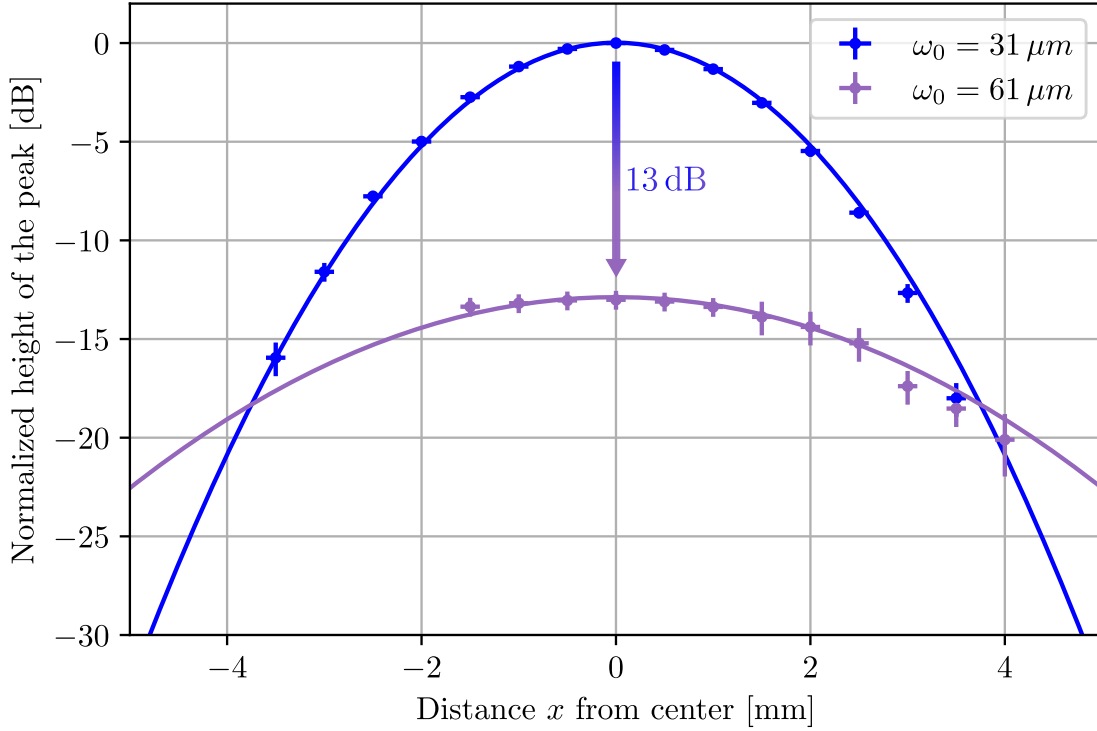Both measurements show a Gaussian distribution for each direction, which is shown

Figure 6.5 – **Comparison of different beam waist sizes ω_0 on the degrading of the peak height in x and y-direction.** Similar to the measurement presented in Figure 6.4, each data point represents the height of the acousto-optic interaction. The blue trace depicts the data presented in Figure 6.4 for $z = 0\,\mathrm{mm}$, where the beam was focused to a beam waist of $31\,\mathrm{\mu m}$. After widening the beam to a waist size with a focus of $61\,\mathrm{\mu m}$, the data shown in purple was taken. For both measurements the electrical signal strength on the transducer and the frequency was identical. The measurement shows that widening the beam waist leads to lower signal strengths (more that $13\,\mathrm{dB}$ as indicated by the arrow) but simultaneously, the drop of the interaction strength for increased x-distances is reduced.

as the solid lines in the figures. For the x-axis this fit was performed with

$$f(x) = A \exp\left(\frac{2(x - x_0)^2}{w_x^2}\right), \tag{6.12}$$

where A describes the maximum value of the fit, x_0 the offset of the maximum and w_x the width. For the y-axis the fit was identical, but with y_0 as the offset and w_y

as the width. The resulting widths of the fits were

$$w_x = (2.56 \pm 0.16)\,\text{mm},\ \ w_y = (1.39 \pm 0.05)\,\text{mm}\,. \tag{6.13}$$

This is expected, as the laser profile in x- and y-direction is different. In the x-direction, laser beam diverges slower than in y-direction. The lower bound of the data points for the y-direction is limited to $-1\,\text{mm}$ by the mechanical range of the transducer.

To find out whether the ultrasonic sound waves itself is diverging, the measurement was repeated for different z-distances, which is outlined by the different colors in Figure 6.4. $z = 0\,\text{mm}$ describes the z-distance at which the transducer can not be shifted closer to the beam without distorting its shape. Applying the Gaussian fit to measurements at different z-distance resulted in similar widths, which indicates that the sound waves are not strongly diverging in this measurement range. The results in 6.13 show the mean value of the four different waists w_x and w_y.

In Figure 6.5, the effect of the size of the beam waist on the acousto-optic interaction is analyzed by enhancing the beam waist from $31\,\mu\text{m}$ to $61\,\mu\text{m}$. This change was preformed by exchanging the lenses, which previously had a focal length of $f = 50\,\text{mm}$, to pair with $f = 100\,\text{mm}$. Typically, the measurement of the beam diameter can be performed with a slit beam profiler, which can analyze the shape and width of the beam by using the knife edge method. For small diameters however, this profiler becomes less precise. The beam waist ω_0 was determined by measuring the beam size at different x-distances, where the diameter is sufficiently large, and performed a Gaussian fit to the data. Besides changing the beam waist, both measurements were performed under identical circumstances. The z-direction was chosen to be $z = 0\,\text{mm}$, the frequency remained at $f = 5.204\,\text{MHz}$. Figure 6.5 shows the comparison of the interaction strength for these both waist sizes. Here, reducing the waist size leads to higher interaction strength in the center but simultaneously causes a faster drop when the x-distance is varied. Applying the same fit from equation 6.12 to the purple trace results in a width of $w_x = (4.74 \pm 0.63)\,\text{mm}$.

6.6 The absorption coefficient in air for high frequencies

For ultrasonic sound waves in air, the absorption coefficient α is an important parameter that describes the attenuation of these waves. Measuring the absorption coefficient for different environmental parameters has been a challenge at higher frequencies due to the low acoustic impedance of air and the high attenuation at MHz frequencies. The first measurements at frequencies above 1 MHz were conducted by Pielmeier et al. in [78], following theoretical predictions by Lebedew in [79]. Experimental work in the 1950s was performed in [80, 81, 82, 83, 84] for frequencies between 1 MHz and 11 MHz and for different gases, including dry air. More recently, in [85], Bond measured the absorption coefficient in air for higher frequencies between 10 MHz and 20 MHz using two transducers - one emitting the ultrasonic waves and the other receiving them. In this section, we characterize the absorption coefficient for frequencies between 4.2 MHz and 7.2 MHz and for different frequencies and temperatures.

6.6.1 Attenuation of ultrasonic sound waves in air

The attenuation of sound waves is described in [86]:

$$A = A_{\text{atm}} + A_{\text{div}} + A_{\text{gr}} + A_{\text{bar}} + A_{\text{misc}}, \qquad (6.14)$$

where A_{atm} describes the atmospheric attenuation due to classical absorption and relaxation losses, A_{div} the attenuation due to geometrical divergence, A_{gr} the attenuation due to ground effects, A_{bar} barrier effects and A_{misc} other miscellaneous effects. A full description and elaboration of the different attenuation contributions can be found in [86]. For high frequencies, the attenuation is dominated by the atmospheric attenuation, which in itself describes classical absorption, where the acoustic field transfers its energy by heating, and relaxation losses, where translational energy is

converted to internal energy of the air molecules. A_{atm} is given by

$$A_{\text{Atm}}(z) = \alpha(f, T, h, p)\frac{z}{1000}, \tag{6.15}$$

where α is the absorption coefficient in $\frac{\text{dB}}{\text{m}}$ and z is the distance between the source and the observer in m. The absorption coefficient depends on the frequency f of the sound wave and the temperature T, humidity h and pressure p of the air. According to [86] at room pressure $p = 101.325\,\text{kPa}$, α can be calculated by

$$
\begin{aligned}
\alpha = 8.689 f^2 \Bigg[& 1.84 \cdot 10^{-11} \left(\frac{T}{T_0}\right)^{1/2} \\
& + \left(\frac{T}{T_0}\right)^{-5/2} \left(\frac{0.01275 \exp(-2239.1/T)}{F_{\text{ro}} + f^2/F_{\text{ro}}} + \frac{0.1068 \exp(-3352/T)}{F_{\text{rn}} + f^2/F_{\text{rn}}}\right) \Bigg],
\end{aligned} \tag{6.16}
$$

where $T_0 = 293.15\,\text{K}$ and F_{ro} and F_{rn} are the relaxation frequencies for oxygen and nitrogen respectively. These relaxation frequencies are calculated with

$$F_{\text{ro}} = 24 + 4.04 \cdot 10^4 h \frac{0.02 + h}{0.391 + h} \tag{6.17}$$

and

$$F_{\text{rn}} = \left(\frac{T}{T_0}\right)^{-1/2} \left(9 + 280 h \exp\left\{-4.170\left[\left(\frac{T}{T_0}\right)^{-1/3} - 1\right]\right\}\right), \tag{6.18}$$

where h is the molar concentration of water vapour in %.

For high frequencies, equation 6.16 simplifies to

$$\alpha = 15.895 \cdot 10^{-11} \left(\frac{T}{T_0}\right) f^2, \tag{6.19}$$

which is the formula, that is used in the following sections to characterize the behavior of the absorption coefficient for different frequencies and temperatures.

6.6.2 Characterization of the absorption coefficient
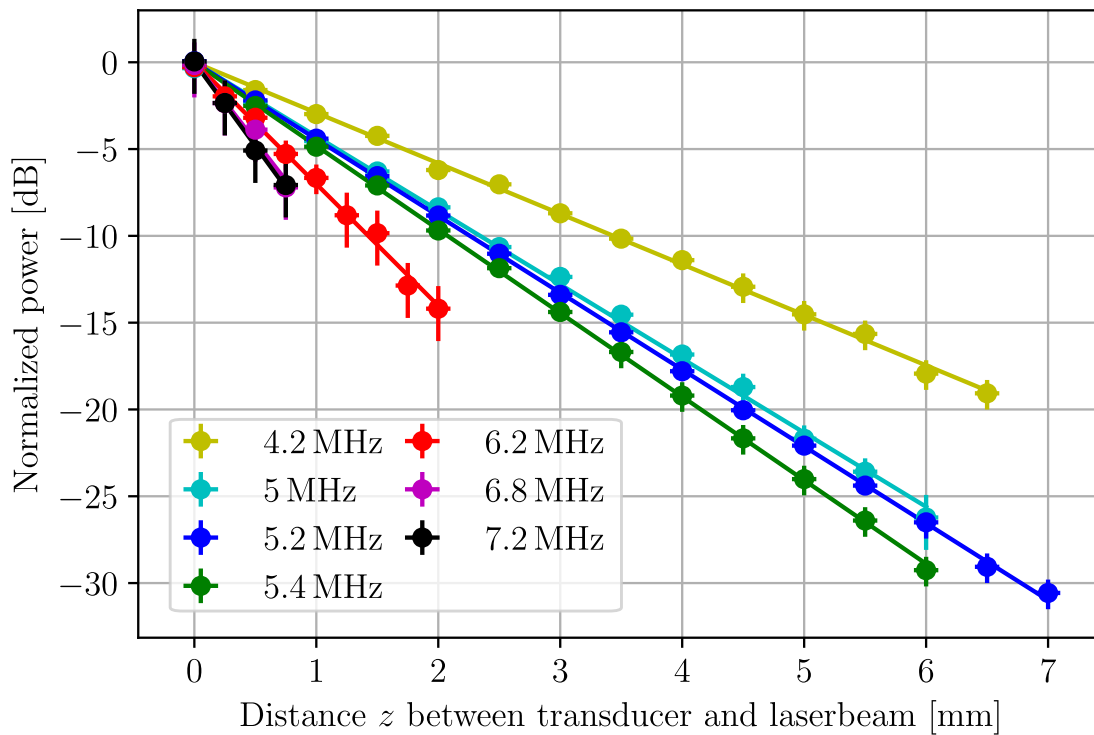
Frequency dependency

Figure 6.6 – **Attenuation of the ultrasonic peak for different frequencies.** Each point shows the height of the ultrasonic sound peak normalized to the maximum which describes the point where the transducer could not be moved closer to the beam before disrupting the beam shape. The power decreases when the transducer is moved away from the laser beam. The slope of each curve describes the absorption coefficient alpha. For high frequencies the transducer moves away from its resonance and the traces have fewer data points.

To measure the absorption coefficient and, therefore, the corresponding attenuation of the sound waves, the distance z between the transducer and the laser beam was changed manually in 0.5 mm-steps with a linear translation stage. The results are shown in Figure 6.6. For every data point, a measurement similar to the one in Figure 6.2 was performed. The height of these peaks was normalized to the respective data taken at $z = 0$. The measurement was repeated for different frequencies from

$f = 4.2\,\mathrm{MHz}$ to $f = 7.2\,\mathrm{MHz}$. This frequency range is limited by the bandwidth of the transducer.
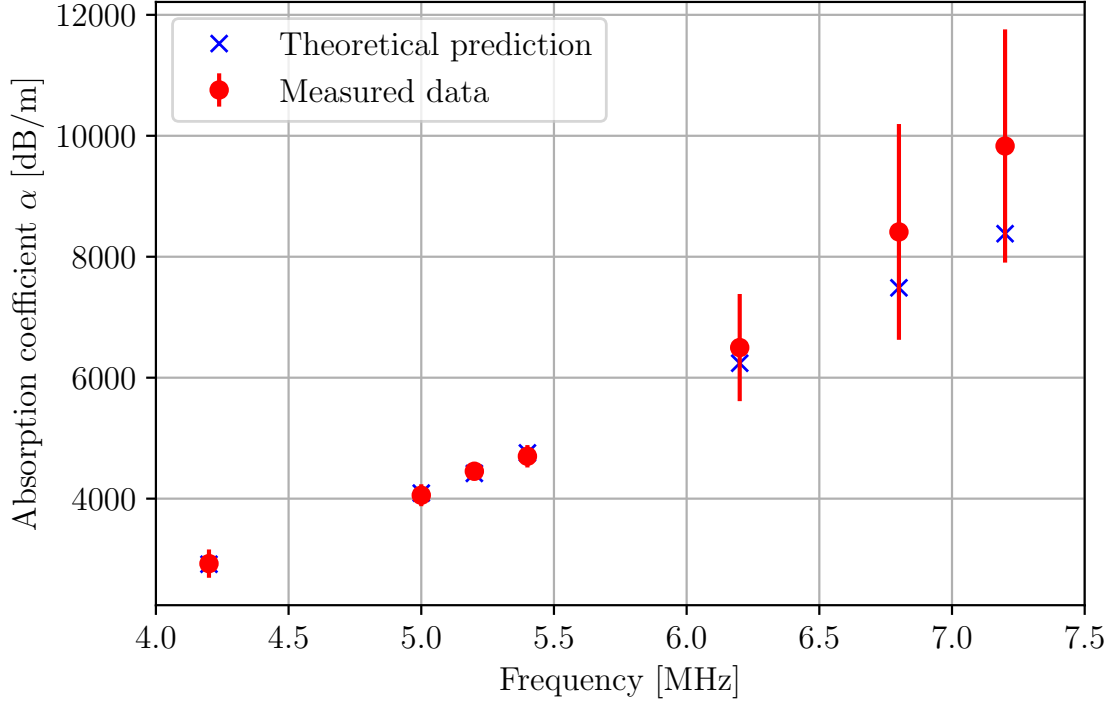

Figure 6.7 – **Absorption coefficient α for different frequencies.** The absorption coefficient was calculated from the traces presented in Figure 6.6 and compared with the theoretical values from equation 6.19. Especially for frequencies up to 5.4 MHz, the measured data is in good agreement with the theoretical prediction. For high frequencies the error bars enhance as the transducer moves off resonance.

On resonance of the transfer function of the transducer, which was found at 5.204 MHz, the peak was still visible when the distance between the transducer and the laser beam was enhanced to 7 mm. Moving the transducer further away leads to the peak vanishing in the shot noise. Off resonance, this distance is reduced, and for 7.2 MHz, the distance between the transducer and the laser beam is limited to 0.75 mm before the peak is undistinguishable from the noise.

Comparing the results of this measurement with equation 6.15, the slope of this trace immediately denotes the absorption coefficient of the sound wave:

$$P(z)[\text{dBm}] = C - \alpha z \,, \tag{6.20}$$

where C represents the height of the ultrasonic peak when the distance between the transducer and the laser beam is $z = 0$. Further deceasing the distance leads to the transducer shifting into the laser beam. Next, the noise power is converted from dBm to mW and an exponential fit is performed on the data. With $P[\text{dBm}] = 10 \log_{10}(\frac{P[W]}{P_0})$ and $P_0 = 1\,\text{mW}$ this leads to

$$P(z)[\text{dBm}] = 10 \log_{10}\left(\frac{P(z)[W]}{P_0}\right) = C - \alpha z \tag{6.21}$$

$$P(z)[W] = P_0 \cdot 10^{C/10} \cdot 10^{-\alpha z/10} \tag{6.22}$$

$$P(z)[W] = C' \cdot \exp\left(\ln\left(10^{-\alpha z/10}\right)\right) \tag{6.23}$$

$$P(z)[W] = C' \cdot \exp\left(-\alpha z \cdot \frac{\ln(10)}{10}\right), \tag{6.24}$$

where $C' = P_0 \cdot 10^{C/10}$. In the normalized measurements, depicted in Figure 6.6, we set $C' = 0$. Performing an exponential fit $y(x) = a \cdot \exp(bx)$ to the data, where in our case $y(x) = P(z)$, $a = C'$ and $b = -\alpha z \cdot \frac{\ln(10)}{10}$, and comparing it to equation 6.21 leads to

$$\alpha = -bz \cdot \frac{10}{\ln(10)} \,. \tag{6.25}$$

The absorption coefficient for each frequency was calculated with equation 6.25 from the data presented in Figure 6.6 and is shown in Figure 6.7. The measured data matches the theoretical prediction particularly well at lower frequencies up to 5.4 MHz. For frequencies above 6.2 MHz, the transducer shifts from its resonance, and therefore, the amplitude of the created sound waves is reduced, which directly results in fewer data points and higher error bars.
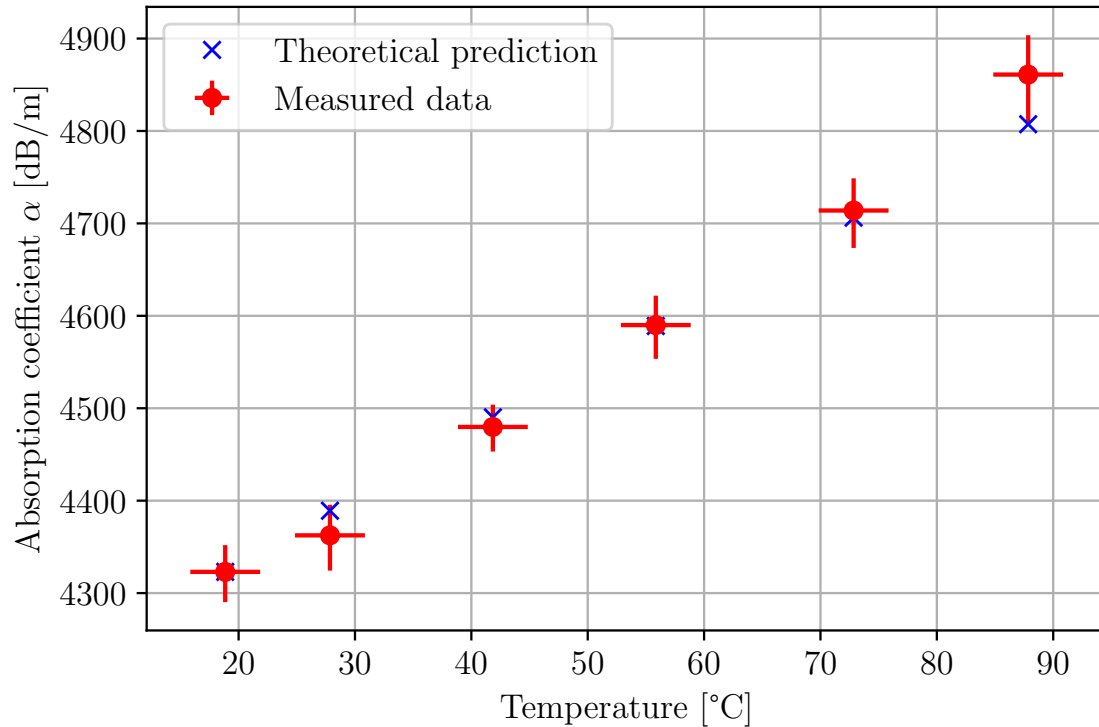
Temperature dependency

Figure 6.8 – **Absorption coefficient α for different temperatures** The absorption coefficient was measured for temperatures between $20\,°C$ and $70\,°C$ at a fixed frequency $f = 5.2\,\text{MHz}$ and a fixed distance $z = 0$. For each data point the peak height was measured and then converted into the absorption coefficient. Theoretical values were derivated from equation 6.19. Until $72\,°C$ the measurements are in good agreement with the theoretical data. For higher temperatures air fluctuations due to the excessive heating were causing heavy fluctuations.

According to equation 6.15, the absorption coefficient α depends on the properties of the ambient air. In our case, changing the pressure p would involve restructuring the experiment, which was difficult to perform without changing the frame of the experiment. The change in humidity, as suggested by the approximation in equation 6.19, is negligible, which means the only other parameter for us to investigate was the temperature T. For that, I designed and built an oven, which consists of a copper tube covered in aluminum foil. Heating wire was coiled around the oven to increase the air temperature in the tube up to $70\,°C$. Five holes in the oven allowed the laser

beam and the ultrasonic wave to each enter and exit the oven. For the ultrasonic wave, the exiting hole prevented a reflecting wave from interacting with the optical field. The fifth hole was used as an entrance for a thermometer, which measured the temperature inside the oven. Figure 6.8 shows the temperature dependence of the absorption coefficient. The measurement was performed at a fixed distance $z = 0$ and a fixed frequency $f = 5.2\,\mathrm{MHz}$, and the temperature was increased from $25\,°\mathrm{C}$ to $70\,°\mathrm{C}$. The data was compared to theoretical values taken from equation 6.19.

The measured data is in good agreement with the theoretical prediction. For high temperatures, strong fluctuations of the peak in the spectrum were observed, represented by the increasing height of the error bars. I assume, that they are caused by air turbulences due to the heating of the oven. For values above $70\,°\mathrm{C}$, these fluctuations become more severe, and ultimately limited the temperature range to $88\,°\mathrm{C}$. On the temperature axes, the error bars are given by the uncertainty of the thermometer, which were in this temperature range about $\pm 2.5\,°\mathrm{C}$.

In Section 6.7, the redesign of the setup to be operable at higher temperatures and higher frequencies is discussed.

6.7 Limitations

As mentioned in Section 6.2, the experimental realization of an interferometer that can detect continuous ultrasonic sound waves is difficult due to multiple reasons:

Electromagnetic stray fields: Due to the low acoustic impedance of air, the signal of the frequency generator to the transducer has to be amplified strongly to produce ultrasonic sound waves with sufficient amplitude. However, this amplification can result in the generation of unwanted electromagnetic stray fields. To decrease their influence, the input impedance of the transducer was adjusted to the output impedance of the frequency generator, which had a value of $R = 50\,\Omega$. Still, it was not possible to completely get rid of these stray fields. To differentiate these stray fields from the genuine acousto-optic interaction, the path between the trans-

ducer and the laser beam was blocked when the electronic dark noise was measured. While the sound waves vanish, the stray fields persist. Additionally, aluminum foil was used to shield the experiment.

Transducer position: The high attenuation and the condition from equation 6.1 result in a small space for placing the transducer relative to the laser beam. Figure 6.4 and 6.6 both show that even on resonance, the transducer can only be moved a couple of millimeter in any direction before the peak cannot be distinguished from the shot noise anymore.

Beam size and divergence: The requirement for a low beam size simultaneously leads to high divergence, which was discussed in Section 6.5. For the detection of ultrasonic sound waves at frequencies above 7.2 MHz, where the wavelength of the sound wave is reduced to $\Lambda = 34\,\mu\text{m}$, the beam size has to be decreased by a factor of 2. However, this enhances the Rayleigh length, limiting the interaction length between the acoustic and the optical field. Combining this effect with the fact, that the transducer is not resonant for higher frequencies means, that measurements for frequencies above 7.2 MHz would require a reconstruction of the experiment.

Temperature fluctuations: To go to higher temperatures, the used oven needs to be redesigned. In the ideal case, the transducer is placed inside a transparent but closed box with an adjustable temperature, which would reduce the fluctuations of the peak for higher temperatures discussed in Section 6.6.2. The laser beam would enter and exit the box through two anti-reflective coated windows to reduce optical losses.

6.8 Conclusion and outlook

Until now, non-contact measurements of vibrations of arbitrary objects are typically performed with a heterodyne laser Doppler vibrometer, which was discussed in Chapter 5. Here, laser light is sent onto the vibrating surface directly and the scattered light contains information about the oscillation. The sensitivity of such

a measurement decreases for rough or uneven surfaces caused by the increase of speckle noise, which is usually circumvented by enhancing the light power sent onto the probe. Increasing the optical power, however, directly leads to eye safety regulations, including laser protection glasses with higher attenuation or the hiring of a laser safety officer. Additionally, for probes with a high absorption, high optical powers can cause damage on the sample. In this experiment, only the interaction of the sound waves, emitted by the vibrating object, with the laser light is detected, which causes the measurement to be independent of the roughness of the surface. Due to this topology, the usage of squeezed light can efficiently be use to increase the signal-to-noise ratio.

Here, I show the characterization of the vibration of an oscillating surface by detecting the pressure changes caused by the ultrasonic sound waves, which were generated a transducer. In a Mach-Zehnder interferometer, the interaction between the acoustic and the optical field was visible as a peak at the oscillation frequency. The topology of the experiment allowed the utilization of high squeezing values over $10\,\mathrm{dB}$ as the optical loss in the system is minimized. In the squeezed homodyne Mach-Zehnder interferometer, pressure changes of sound waves as low as $(0.12 \pm 0.02)\,\frac{\mathrm{mPa}}{\sqrt{\mathrm{Hz}}}$ were detected. Additionally, by changing the relative position of the transducer to the laser beam, a reconstruction of the pressure field in x- and y-direction was generated. In a frequency range between $4.2\,\mathrm{MHz}$–$7.2\,\mathrm{MHz}$ and an ambient temperature of the system between $25\,°\mathrm{C}$–$70\,°\mathrm{C}$, a precise analysis of the absorption coefficient for ultrasonic waves was derived, which was challenging due to the high attenuation of air at these frequencies as well as the low acoustic impedance of air. The results were in good agreement with the theoretical prediction, which confirmed that the signal was generated by the acousto-optic interaction.

In principle, this measurement can be performed in every interferometric design. Here, the specific applications determine which type of interferometer and which readout is suited best. For high amplitudes or signals at very low frequencies, heterodyne schemes are advantageous, whereas for smaller signal strengths the more sensitive homodyne readout is more beneficial. Additionally, the heterodyne readout does not require the active length stabilization to the mid-fringe condition. In terms

of interferometric design choice, laser Doppler vibrometer are often used for the detection of sound waves. In this topology, the interaction between the acoustic and the optical field is generated between the PBS and the reflecting mirror. The laser light passes the sound waves twice, increasing the sensitivity by a factor of 2 compared to the Mach-Zehnder interferometer. On the other hand, the Mach-Zehnder interferometer requires less optical components. For the length stabilization, the MZI utilizes the DC-signal of the detector as an error signal, which simplifies the locking scheme as this signal is already accessible and necessary for the adjustment of the homodyne detector.

7 Summary and outlook

Outside of enhancing the optical laser power, squeezed light provides the only possibility to increase the sensitivity of shot noise limited interferometers. Most prominently in gravitational wave detectors, where enhancing the laser power is accustomed by problems such as thermal lensing or damage on the optics, squeezed light remains a powerful tool to enhance the detectable eventrate. Especially frequency-dependent squeezing, which enables the simultaneous decrease of both the quantum shot noise as well as the quantum radiation pressure noise, is more advantageous than the increase of the optical power.

In the last decades, vast improvements for the detection of high squeeze values were conducted. With highly stable feedback systems, low noise seed lasers and strong advancements in the quantum efficiency of the photodiodes and the loss of the coatings on the optics, squeeze values reached new heights. Utilizing these high squeezing values in quantum sensing, communication and eventually computing, however, is challenging. The development of future squeeze lasers shifts towards facilitating the transportation and integration of the setup, prioritizing compact size, ease of shipping, and rapid implementation with a highly stable output, comparable to the evolution of the classical laser system over the last seventy years. This development would be the first step for the commercial application of the squeeze laser. In contrast to conventional laser systems the setup of a squeeze laser is complex and requires the larger spaces. Until now, experiments, which take advantage of squeezed light, are often times built next to the squeeze laser or vice versa.

To open the path for a new generation of squeeze lasers, the primary goals of this thesis are the compactification of squeeze laser and to find new applications in

interferometric schemes, that specifically focus on investigating vibrating structures.

For this purpose, I firstly set up two different designs for squeeze lasers. For the first one, a monolithic cavity design was compared to a hemilithic one at 1550 nm on a 80 cm×80 cm breadboard. Here, the monolithic design produced 10.7 dB of squeezing at a sideband frequency of 5 MHz with 7 % of optical loss, while the hemilithic one generated 10.5 dB with 7.2 % of optical loss at the same frequency. As no significant difference in squeezing performance was observed, the more stable and easier-to-set-up hemilithic design was selected for future squeeze lasers. Subsequently, through optimization of the optical arrangement and reduction of non-essential components, the size of the breadboard was reduced to 60 cm×40 cm, which facilitated the transportation of the experiment. Despite the size reduction, the squeeze laser produced more than 10 dB of squeezing with 7.9 % of optical loss at 5 MHz detected on the on-board homodyne detector.

In a collaboration project, funded by the Deutsche Forschungsgemeinschaft (DFG), one of the squeeze laser built in Chapter 4 was implemented in a heterodyne laser Doppler vibrometer (LDV), which was separately built by Mengwei Yu in the group of Christian Rembe and stationed in the Clausthal University of Technology (TUC) in Clausthal-Zellerfeld. LDVs are the state-of-the-art detection method for measurements of vibrations by detecting the Doppler shift caused by the oscillating surface. For this purpose the squeeze laser and its supporting electronics were prepared for transportation. In the TUC a squeezed light enhancement of the heterodyne LDV of more than 2.7 dB was achieved. With this enhancement, the detection of the oscillation of a mirror at 1 MHz by using the light reflected of the sample was shown. Additionally, I characterized the degrading of the squeeze laser over a span of fifteen months. Typically, squeeze lasers are stored in particle filtered rooms to minimize dust entering the setup. In the TUC laboratory, where this was not the case, the housing we built provided sufficient cover, and no degradation inside the squeeze laser was observed. On the other hand, the external homodyne detector, which was stored outside of the housing, showed a decline in its performance, which was most certainly caused by dust particles deposed either on optical components or on the photodiodes of the detector.

Finally, I provide an alternative approach to detect surface vibrations. The LDV faces challenges for rough or uneven surfaces or when the absorption of the surface is high. In these cases, the signal-to-noise ratio is reduced and requires higher light powers. Additionally, due to an increase of optical loss, the impact of squeezed light decreases. Our experiment circumvents this issue by detecting the sound waves created by the surface vibration. To achieve this, a Mach-Zehnder interferometer was modified, demonstrating the detection of ultrasonic sound waves between 4.2 MHz–7.2 MHz with a sensitivity down to $0.12 \frac{\mathrm{mPa}}{\sqrt{\mathrm{Hz}}}$. In this configuration, the optical loss of the setup is minimized, while the main contributions are the interferometer contrast and the quantum efficiency of the photodiodes. With only 7.8 % of optical loss, this allows the detection of strongly squeezed states of light of 10.2 dB. Furthermore, an analysis of the absorption coefficient for ultrasonic sound waves was conducted, a challenging task due to the acoustic impedance of air and the high attenuation of sound waves at high frequencies. This characterization was performed for different frequencies and temperatures.

My thesis demonstrates the advantageous application prospects of the squeeze laser in two separate proof-of-principle experiments. Both focus on the detection of vibrations in different schemes. I show, that current squeeze laser technology allows for devices of merely 60 cm×40 cm as well as the transportation and the successful integration in a conventional heterodyne laser Doppler vibrometer. The results of this thesis combine the detection of vibrations, in both homodyne and heterodyne systems, and the sensitivity enhancing aspects of quantum squeezing. The presented work will therefore provide an outline for the construction of small, but robust and easy-to-use future squeeze laser. It makes a significant contribution to the development of squeeze laser in optical sensor technology and opens up the path for commercially available squeeze lasers and enabling completely new quantum-enhanced technologies for laser-based measurements.

Bibliography

[1] W. Heisenberg. "Über quantentheoretische Umdeutung kinematischer und mechanischer Beziehungen." In: *Zeitschrift für Physik* 33 (1 Dec. 1925), pp. 879–893. DOI: 10.1007/BF01328377.

[2] M. Born and P. Jordan. "Zur Quantenmechanik". In: *Zeitschrift für Physik* 34 (1 Dec. 1925), pp. 858–888. DOI: 10.1007/BF01328531.

[3] M. Born, W. Heisenberg, and P. Jordan. "Zur Quantenmechanik. II." In: *Zeitschrift für Physik* 35 (8 Aug. 1926), pp. 557–615. DOI: 10.1007/BF01379806.

[4] R. E. Slusher et al. "Observation of Squeezed States Generated by Four-Wave Mixing in an Optical Cavity". In: *Phys. Rev. Lett.* 55 (22 Nov. 1985), pp. 2409–2412. DOI: 10.1103/PhysRevLett.55.2409.

[5] R. M. Shelby et al. "Broad-Band Parametric Deamplification of Quantum Noise in an Optical Fiber". In: *Phys. Rev. Lett.* 57 (6 Aug. 1986), pp. 691–694. DOI: 10.1103/PhysRevLett.57.691.

[6] L. Wu et al. "Generation of Squeezed States by Parametric Down Conversion". In: *Phys. Rev. Lett.* 57 (20 Nov. 1986), pp. 2520–2523. DOI: 10.1103/PhysRevLett.57.2520.

[7] H. Vahlbruch et al. "Observation of Squeezed Light with 10-dB Quantum-Noise Reduction". In: *Phys. Rev. Lett.* 100 (3 Jan. 2008), p. 033602. DOI: 10.1103/PhysRevLett.100.033602.

[8]   H. Vahlbruch et al. "Detection of 15 dB Squeezed States of Light and their Application for the Absolute Calibration of Photoelectric Quantum Efficiency". In: *Phys. Rev. Lett.* 117 (11 Sept. 2016), p. 110801. DOI: 10.1103/PhysRevLett.117.110801.

[9]   M. Mehmet et al. "Squeezed light at 1550 nm with a quantum noise reduction of 12.3 dB". In: *Opt. Express* 19.25 (Dec. 2011), pp. 25763–25772. DOI: 10.1364/OE.19.025763.

[10]   A. Schönbeck, F. Thies, and R. Schnabel. "13 dB squeezed vacuum states at 1550 nm from 12 mW external pump power at 775 nm". In: *Opt. Lett.* 43.1 (Jan. 2018), pp. 110–113. DOI: 10.1364/OL.43.000110.

[11]   F. Meylahn, B. Willke, and H. Vahlbruch. "Squeezed States of Light for Future Gravitational Wave Detectors at a Wavelength of 1550 nm". In: *Phys. Rev. Lett.* 129 (12 Sept. 2022), p. 121103. DOI: 10.1103/PhysRevLett.129.121103.

[12]   C. D. Fromm et al. "Squeezed light at 2128 nm for future gravitational wave detectors". In: *Opt. Lett.* 46.23 (Dec. 2021), pp. 5850–5853. DOI: 10.1364/OL.433878.

[13]   H. Grote et al. "First Long-Term Application of Squeezed States of Light in a Gravitational-Wave Observatory". In: *Phys. Rev. Lett.* 110 (18 May 2013), p. 181101. DOI: 10.1103/PhysRevLett.110.181101.

[14]   M. Tse et al. "Quantum-Enhanced Advanced LIGO Detectors in the Era of Gravitational-Wave Astronomy". In: *Phys. Rev. Lett.* 123 (23 Dec. 2019), p. 231107. DOI: 10.1103/PhysRevLett.123.231107.

[15]   F. Acernese et al. "Increasing the Astrophysical Reach of the Advanced Virgo Detector via the Application of Squeezed Vacuum States of Light". In: *Phys. Rev. Lett.* 123 (23 Dec. 2019), p. 231108. DOI: 10.1103/PhysRevLett.123.231108.

[16]   D. Ganapathy et al. "Broadband Quantum Enhancement of the LIGO Detectors with Frequency-Dependent Squeezing". In: *Phys. Rev. X* 13 (4 Oct. 2023), p. 041021. DOI: 10.1103/PhysRevX.13.041021.

[17] C. H. Bennett and G. Brassard. "Quantum cryptography: Public key distribution and coin tossing". In: *Theoretical Computer Science* 560 (2014). Theoretical Aspects of Quantum Cryptography – celebrating 30 years of BB84, pp. 7–11. ISSN: 0304-3975. DOI: `https://doi.org/10.1016/j.tcs.2014.05.025`.

[18] S. Pirandola et al. "Advances in quantum cryptography". In: *Adv. Opt. Photon.* 12.4 (Dec. 2020), pp. 1012–1236. DOI: `10.1364/AOP.361502`.

[19] M. A. Taylor et al. "Biological measurement beyond the quantum limit". In: *Nature Photonics* 7 (3 Mar. 2013), pp. 229–233. DOI: `10.1038/nphoton.2012.346`.

[20] A. Khalaidovski. "Beyond the quantum limit : a squeezed-light laser in GEO 600". PhD thesis. Gottfried Wilhelm Leibniz Universität Hannover, 2011.

[21] A. Schönbeck. "Compact squeezed-light source at 1550 nm". PhD thesis. Universität Hamburg, 2018.

[22] C. M. Caves and B. L. Schumaker. "New formalism for two-photon quantum optics. I. Quadrature phases and squeezed states". In: *Phys. Rev. A* 31 (5 May 1985), pp. 3068–3092. DOI: `10.1103/PhysRevA.31.3068`.

[23] B. L. Schumaker and C. M. Caves. "New formalism for two-photon quantum optics. II. Mathematical foundation and compact notation". In: *Phys. Rev. A* 31 (5 May 1985), pp. 3093–3111. DOI: `10.1103/PhysRevA.31.3093`.

[24] C. Gerry and P. Knight. *Introductory Quantum Optics*. Cambridge University Press, 2004. DOI: `10.1017/CBO9780511791239`.

[25] R. Schnabel. "Squeezed states of light and their applications in laser interferometers". In: *Physics Reports* 684 (2017), pp. 1–51. ISSN: 0370-1573. DOI: `https://doi.org/10.1016/j.physrep.2017.04.001`.

[26] R. J. Glauber. "Coherent and Incoherent States of the Radiation Field". In: *Phys. Rev.* 131 (6 Sept. 1963), pp. 2766–2788. DOI: `10.1103/PhysRev.131.2766`.

[27] P. A. Franken and J. F. Ward. "Optical Harmonics and Nonlinear Phenomena". In: *Rev. Mod. Phys.* 35 (1 Jan. 1963), pp. 23–39. DOI: `10.1103/RevModPhys.35.23`.

[28]   R. E. Slusher et al. "Pulsed Squeezed Light". In: *Phys. Rev. Lett.* 59 (22 Nov. 1987), pp. 2566–2569. DOI: 10.1103/PhysRevLett.59.2566.

[29]   J. Bauchrowitz. "Messung und graphische Darstellung von Ein- und Zwei-Moden-gequetschten Zusänden des Lichts". PhD thesis. Gottfried Wilhelm Leibniz Universität Hannover, 2013.

[30]   M. M. Fejer et al. "Quasi-phase-matched second harmonic generation: tuning and tolerances". In: *IEEE Journal of Quantum Electronics* 28.11 (1992), pp. 2631–2654. DOI: 10.1109/3.161322.

[31]   D. S. Hum and M. M. Fejer. "Quasi-phasematching". In: *Comptes Rendus Physique* 8.2 (2007). Recent advances in crystal optics, pp. 180–198. ISSN: 1631-0705. DOI: https://doi.org/10.1016/j.crhy.2006.10.022.

[32]   M. O. Scully and M. S. Zubairy. *Quantum Optics.* Cambridge University Press, 1997. DOI: 10.1017/CBO9780511813993.

[33]   H. P. Yuen and V. W. S. Chan. "Noise in homodyne and heterodyne detection". In: *Opt. Lett.* 8.3 (Mar. 1983), pp. 177–179. DOI: 10.1364/OL.8.000177.

[34]   M. Collett, R. Loudon, and C. Gardiner. "Quantum Theory of Optical Homodyne and Heterodyne Detection". In: *Journal of Modern Optics* 34.6-7 (1987), pp. 881–902. DOI: 10.1080/09500348714550811.

[35]   M. S. Stefszky et al. "Balanced homodyne detection of optical quantum states at audio-band frequencies and below". In: *Classical and Quantum Gravity* 29.14 (June 2012), p. 145015. DOI: 10.1088/0264-9381/29/14/145015.

[36]   K. L. Dooley et al. "Phase control of squeezed vacuum states of light in gravitational wave detectors". In: *Opt. Express* 23.7 (Apr. 2015), pp. 8235–8245. DOI: 10.1364/OE.23.008235.

[37]   S. Dwyer et al. "Squeezed quadrature fluctuations in a gravitational wave detector using squeezed light". In: *Opt. Express* 21.16 (Aug. 2013), pp. 19047–19060. DOI: 10.1364/OE.21.019047.

[38]   E. Oelker et al. "Ultra-low phase noise squeezed vacuum source for gravitational wave detectors". In: *Optica* 3.7 (July 2016), pp. 682–685. DOI: 10.1364/OPTICA.3.000682.

[39] E. S. Polzik, J. Carri, and H. J. Kimble. "Atomic spectroscopy with squeezed light for sensitivity beyond the vacuum-state limit". In: *Applied Physics B* 55 (3 1992), pp. 279–290. ISSN: 0370-1573. DOI: `https://doi.org/10.1007/BF00325016`.

[40] R. Schnabel and A. Schönbeck. "The "Squeeze Laser"". In: *IEEE Transactions on Quantum Engineering* 3 (2022), pp. 1–9. DOI: `10.1109/TQE.2022.3224686`.

[41] J. Gniesmer. "Advanced Techniques for Squeezed-Light-Enhanced Gravitational Wave Detection". PhD thesis. Gottfried Wilhelm Leibniz Universität Hannover, 2019.

[42] H. Vahlbruch. "Squeezed Light for Gravitational Wave Astronomy". PhD thesis. Gottfried Wilhelm Leibniz Universität Hannover, 2008.

[43] S. Steinlechner. "Gequetschtes Licht bei 1550nm". Diploma. Gottfried Wilhelm Leibniz Universität Hannover, 2008.

[44] R. W. P. Drever et al. "Laser phase and frequency stabilization using an optical resonator". In: *Applied Physics B* 97 (June 1983). DOI: `10.1007/BF00702605`.

[45] O. Huhs. "Automated control of phase matching and double resonance in laser frequency conversion". Master thesis. Universität Hamburg, 2021.

[46] S. Chelkowski et al. "Coherent control of broadband vacuum squeezing". In: *Phys. Rev. A* 75 (4 Apr. 2007), p. 043814. DOI: `10.1103/PhysRevA.75.043814`.

[47] T. Kashiwazaki et al. "Over-8-dB squeezed light generation by a broadband waveguide optical parametric amplifier toward fault-tolerant ultra-fast quantum computers". In: *Applied Physics Letters* 122.23 (June 2023), p. 234003. ISSN: 0003-6951. DOI: `10.1063/5.0144385`.

[48] S. Rothberg et al. "An international review of laser Doppler vibrometry: Making light work of vibration measurement". In: *Optics and Lasers in Engineering* 99 (2017). Laser Doppler vibrometry, pp. 11–22. ISSN: 0143-8166. DOI: `https://doi.org/10.1016/j.optlaseng.2016.10.023`.

[49]   G. M. Revel, M. Martarelli, and P. Chiariotti. "A new laser vibrometry-based 2D selective intensity method for source identification in reverberant fields: part II. Application to an aircraft cabin". In: *Measurement Science and Technology* 21.7 (May 2010), p. 075108. DOI: 10.1088/0957-0233/21/7/075108.

[50]   M. Fischer et al. "Hot on the trail of squealing brakes - 3-D vibrometry makes noise sources visible". In: *Sound and Vibration* 39.7 (2005), pp. 7–8.

[51]   J. Zheng, J. Pan, and H. Huang. "An experimental study of winding vibration of a single-phase power transformer using a laser Doppler vibrometer". In: *Applied Acoustics* 87 (2015), pp. 30–37. ISSN: 0003-682X. DOI: https://doi.org/10.1016/j.apacoust.2014.06.012.

[52]   A. M. Huber et al. "Stapes prosthesis attachment: The effect of crimping on sound transfer in otosclerosis surgery". In: *Laryngoscope* 113.5 (2003), pp. 853–858. DOI: 10.1097/00005537-200305000-00015.

[53]   M. Yu et al. "Heterodyne laser Doppler vibrometer with squeezed light enhancement". In: *Opt. Lett.* 48.21 (Nov. 2023), pp. 5607–5610. DOI: 10.1364/OL.494064.

[54]   G. A. Massey. "Practical applications of the optical-heterodyne ultrasonic image-converter". In: *Ultrasonics* 8.1 (1970), pp. 16–18. ISSN: 0041-624X. DOI: https://doi.org/10.1016/0041-624X(70)90792-4.

[55]   Y. Yeh and H. Cummins. "Localized Fluid Flow Measurements with an He-Ne Laser Spectrometer". In: *Applied Physics Letters* 4 (June 1964), pp. 176–178. DOI: 10.1063/1.1753925.

[56]   W. Li, X. Yu, and J. Zhang. "Measurement of the squeezed vacuum state by a bichromatic local oscillator". In: *Opt. Lett.* 40.22 (Nov. 2015), pp. 5299–5302. DOI: 10.1364/OL.40.005299.

[57]   W. Li et al. "Enhanced detection of a low-frequency signal by using broad squeezed light and a bichromatic local oscillator". In: *Phys. Rev. A* 96 (2 Aug. 2017), p. 023808. DOI: 10.1103/PhysRevA.96.023808.

[58] B. Xie and S. Feng. "Squeezing-enhanced heterodyne detection of 10Hz atto-Watt optical signals". In: *Opt. Lett.* 43.24 (Dec. 2018), pp. 6073–6076. DOI: `10.1364/OL.43.006073`.

[59] K. Anai et al. "Quantum-enhanced optical beat-note detection beyond 3-dB noise penalty of image band". In: *ArXiv e-prints* (2023). DOI: `https://doi.org/10.48550/arXiv.2305.06579`.

[60] J. C. Dainty. *Laser speckle and related phenomena.* Vol. 9. Springer science & business Media, 2013.

[61] J. Zander, C. Rembe, and R. Schnabel. "10 dB interferometer enhancement by squeezing of photon shot noise with sub-femtometer resolution and eye-safe optical power". In: *Quantum Science and Technology* 8.1 (Oct. 2022), 01LT01. DOI: `10.1088/2058-9565/ac9ad5`.

[62] R. Reibold and P. Kwiek. "Optical Nearfield of Ultrasonic Light Diffraction". In: *Physical Acoustics: Fundamentals and Applications.* Ed. by O. Leroy and M. A. Breazeale. Boston, MA: Springer US, 1991, pp. 129–142. ISBN: 978-1-4615-9573-1. DOI: `10.1007/978-1-4615-9573-1_12`.

[63] K. V. D. Abeele and O. Leroy. "Probing of ultrasonic pulses by multidirectional light". In: *Ultrasonics* 29.6 (1991), pp. 464–470. ISSN: 0041-624X. DOI: `https://doi.org/10.1016/0041-624X(91)90077-L`.

[64] P. Kwiek, W. Molkenstruck, and R. Reibold. "Optical mapping of ultrasonic fields in the intermediate range between weak and strong acousto-optical interaction". In: *Ultrasonics* 35.7 (1997), pp. 499–507. ISSN: 0041-624X. DOI: `https://doi.org/10.1016/S0041-624X(97)00035-8`.

[65] Y. Schrödel et al. "Acousto-optic modulation of gigawatt-scale laser pulses in ambient air". In: *Nature Photonics* (Oct. 2023). ISSN: 1749-4893. DOI: `10.1038/s41566-023-01304-y`.

[66] X. Jia, G. Quentin, and M. Lassoued. "Optical heterodyne detection of pulsed ultrasonic pressures". In: *IEEE Transactions on Ultrasonics, Ferroelectrics, and Frequency Control* 40.1 (1993), pp. 67–69. DOI: `10.1109/58.185000`.

[67]   X. Jia, L. Adler, and G. Quentin. "Interferometric detection of finite-amplitude ultrasonic waves". In: *1994 Proceedings of IEEE Ultrasonics Symposium.* Vol. 2. 1994, pp. 833–836. DOI: 10.1109/ULTSYM.1994.401770.

[68]   A. R. Harland, J. N. Petzing, and J. R. Tyrer. "Nonperturbing measurements of spatially distributed underwater acoustic fields using a scanning laser Doppler vibrometer". In: *The Journal of the Acoustical Society of America* 115.1 (Dec. 2003), pp. 187–195. ISSN: 0001-4966. DOI: 10.1121/1.1635841.

[69]   O. B. Matar et al. "Mapping of airborne ultrasonic fields using optical heterodyne probing and tomography reconstruction". In: *2000 IEEE Ultrasonics Symposium. Proceedings. An International Symposium (Cat. No.00CH37121).* Vol. 2. 2000, 1117–1120 vol.2. DOI: 10.1109/ULTSYM.2000.921521.

[70]   L. Zipser, S. Lindner, and R. Behrendt. "Interferometrische Messung und Visualisierung von Schallwellen und Turbulenzen (Interferometric Measurement and Visualisation of Acoustic Waves and Vortexes)". In: *Technisches Messen* 69.6 (2002), pp. 275–281. DOI: doi:10.1524/teme.2002.69.6.275.

[71]   L. Chen, S. J. Rupitsch, and R. Lerch. "A reliability study of light refractive tomography utilized for noninvasive measurement of ultrasound pressure fields". In: *IEEE Transactions on Ultrasonics, Ferroelectrics, and Frequency Control* 59.5 (2012), pp. 915–927. DOI: 10.1109/TUFFC.2012.2276.

[72]   L. Chen, S. J. Rupitsch, and R. Lerch. "Quantitative reconstruction of a disturbed ultrasound pressure field in a conventional hydrophone measurement". In: *IEEE Transactions on Ultrasonics, Ferroelectrics, and Frequency Control* 60.6 (2013), pp. 1199–1206. DOI: 10.1109/TUFFC.2013.2682.

[73]   S. J. Rupitsch et al. "Quantitative Measurement of Airborne Ultrasound Utilizing Light Refractive Tomography". In: *Sensors and Measuring Systems 2014; 17. ITG/GMA Symposium.* 2014, pp. 1–5.

[74]   J. Zander. "Squeezed and Entangled Light: From Foundations of Quantum Mechanics to Quantum Sensing". PhD thesis. Universität Hamburg, 2021.

[75] L. Zipser and H. Franke. "Laser-scanning vibrometry for ultrasonic transducer development". In: *Sensors and Actuators A: Physical* 110.1 (2004). Selected Papers from Eurosensors XVI Prague, Czech Republic, pp. 264–268. ISSN: 0924-4247. DOI: https://doi.org/10.1016/j.sna.2003.10.051.

[76] L. Kleybolte. "Sensitivity Enhancement of Optomechanical Measurements using Squeezed Light". PhD thesis. Universität Hamburg, 2019.

[77] T. Eberle. "Realization of Finite-Size Quantum Key Distribution based on Einstein-Podolsky-Rosen Entangled Light". PhD thesis. Gottfried Wilhelm Leibniz Universität Hannoverr, 2016.

[78] W. H. Pielemeier. "Observed Classical Sound Absorption in Air". In: *The Journal of the Acoustical Society of America* 17.1 (June 2005), pp. 24–28. ISSN: 0001-4966. DOI: 10.1121/1.1916295.

[79] P. Lebedev. "Die Grenzwerte Der Kürzesten Akustischen Wellen." In: *Annalen der Physik* 340.6 (June 1911), pp. 171–174. DOI: doi:10.1002/andp.2093400610.

[80] M. Greenspan. "Propagation of Sound in Rarefied Helium". In: *The Journal of the Acoustical Society of America* 22.5 (June 1950), pp. 568–571. DOI: 10.1121/1.1906652.

[81] M. Greenspan. "Propagation of Sound in Five Monatomic Gases". In: *The Journal of the Acoustical Society of America* 28.4 (June 1956), pp. 644–648. DOI: 10.1121/1.1908432.

[82] W. Tempest and H. D. Parbrook. "The absorption of sound in argon,nitrogen and oxygen". In: *Acustica*. Vol. 7. 1957, pp. 354–362.

[83] M. Greenspan. "Rotational Relaxation in Nitrogen, Oxygen, and Air". In: *The Journal of the Acoustical Society of America* 31.2 (July 1959), pp. 155–160. ISSN: 0001-4966. DOI: 10.1121/1.1907686.

[84] H. E. Bass and R. G. Keeton. "Ultrasonic absorption in air at elevated temperatures". In: *The Journal of the Acoustical Society of America* 58.1 (July 1975), pp. 110–112. ISSN: 0001-4966. DOI: 10.1121/1.380638.

[85] L. J. Bond, C. Chiang, and C. M. Fortunko. "Absorption of ultrasonic waves
      in air at high frequencies (10–20 MHz)". In: *The Journal of the Acoustical
      Society of America* 92.4 (Oct. 1992), pp. 2006–2015. ISSN: 0001-4966. DOI:
      `10.1121/1.405251`.

[86] *Acoustics - Attenuation of sound during propagation outdoors - Part 1: Cal-
      culation of the absorption of sound by the atmosphere.* Standard. Geneva, CH:
      International Organization for Standardization, June 1993.

Publications

L. Kleybolte, P. Gewecke, A. Sawadsky, M. Korobko, and R. Schnabel "Squeezed-Light Interferometry on a Cryogenically Cooled Micromechanical Membrane" In: Phys. Rev. Lett. 125, (Nov. 2020), pp. 213601.

[53] M. Yu, P. Gewecke, J. Südbeck, A. Schönbeck, R. Schnabel and C. Rembe "Heterodyne laser Doppler vibrometer with squeezed light enhancement". In: Opt. Lett. 48.21 (Nov. 2023), pp. 5607-5610.

Danksagung

Zum Ende der Arbeit möchte ich mich bei mehreren Personen bedanken. Allen voran bei meinem Doktorvater, Roman, für die Unterstützung, die Hilfe bei allen möglichen Problemen, dem offenen Ohr, wenn ich mal nicht weiter kam und der Möglichkeit, meine Arbeit in der Arbeitsgruppe zu absolvieren. Die legendären Doppelkopfrunden muss ich natürlich auch einmal erwähnen. Ohne dich hätte ich das alles nicht geschafft, vielen Dank!

Zudem möchte ich mich bei meiner tollen Arbeitsgruppe bedanken: Bei Jan und Jascha für die schöne Zeit in den letzten fünf Jahren. Bei Axel und Mikhail für die viele Hilfe während der Arbeit. Bei Lisa für die schöne Zeit in meiner Masterarbeit. Bei meinem "Jahrgang", vor allem bei Julian, Bene, Alex, Maik, Daniel, Sophie und Justin für die schönen Stunden während der Arbeit, aber auch außerhalb. Bei Dieter und Kirstin und bei der "nächsten" Generation um Jonas, Nils, Leif und Rene.

Großer Dank geht an meine Familie und an meine Freunde für die viele Unterstüzung während des gesamten Studiums, ohne euch hätte ich das nicht geschafft!

Und da dies vermutlich das Ende meiner Studienzeit darstellt, will ich auch all meinen ehemaligen Kommilitonen danken, die ich während meiner Zeit kennen lernen durfte. Ich habe die Zeit extrem genossen!

Und wie in jedem guten Buch gilt der letzte Dank ... Dir, als Leser, der du gerade diese Arbeit (bestimmt komplett) durchgearbeitet hast. Ich hoffe, sie hat dir gefallen!

Eidesstattliche Versicherung / Declaration on oath

Hiermit versichere ich an Eides statt, die vorliegende Dissertationsschrift selbst verfasst und keine anderen als die angegebenen Hilfsmittel und Quellen benutzt zu haben.

Die eingereichte schriftliche Fassung entspricht der auf dem elektronischen Speichermedium.

Ich bin damit einverstanden, dass die Doktorarbeit veröffentlicht wird.

Hamburg, den 26.01.2024

Pascal Gewecke